




Newberry Geothermal Energy

A Research Observatory for a Sustainable Future

Newberry Geothermal Energy

Establishment of the Frontier Observatory for Research in Geothermal Energy (FORGE) at Newberry Volcano, Oregon

Appendix A

Conceptual Geologic Model

April 27, 2016

Contents

A.1 Summary A.1
A.2 Geological and Geophysical Context of the Western Flank of Newberry Volcano A.2
A.2.1 Data Sources A.2
A.2.2 Geography A.3
A.2.3 Regional Setting A.4
A.2.4 Regional Stress Orientation A.10
A.2.5 Faulting Expressions A.11
A.2.6 Geomorphology A.12
A.2.7 Regional Hydrology A.20
A.2.8 Natural Seismicity A.24
A.2.9 Geophysical Studies A.25
A.2.10 Geothermal Exploration A.43
A.2.11 Conditions at the Proposed NEWGEN FORGE Site Area A.49
A.3 Newberry Volcano EGS Demonstration A.63
A.3.1 Summary of Results A.64
A.3.2 Implications of NEGSD Stimulation of Stress Magnitude Model A.65
A.4 NEWGEN Conceptual Geologic Models: Methodologies, Results and Interpretation A.67
A.4.1 Coupled Thermal-Hydrological-Mechanical-Chemical Model A.68
A.4.2 Thermal Model A.70
A.4.3 Representation in EarthVision A.72
A.5 NEWGEN Parameter Summary and Uncertainty A.80
A.5.1 Parameters Summary A.82
A.5.2 Preliminary Analyses for Quantifying Uncertainties in the Characterization Data A.86
A.5.3 Future Approach for Uncertainty Quantification, Propagation, and Reduction A.88
A.6 References A.91

Figures

A.1 Tectonic boundaries and geological provinces of the Pacific Northwest A.4
A.2 Block motions for Cascadia forearc proposed by Wells et al. A.6
A.3 Regional fault map showing the location of the NEWGEN FORGE site and the intersection of principal structural trends in Central Oregon A.7
A.4 LiDAR-based digital elevation mapping indicates the regional fault fabric and volcanic landforms at Newberry Volcano A.9
A.5 Topographic profiles A-A', B-B', and C-C' A.13
A.6 Lava flows and young volcanic vents at Newberry Volcano.. A.14
A.7 Location of cross sections and geothermal exploration wells surrounding the NEWGEN FORGE site. A.18
A.8 West-east cross-section A-A' showing formation correlations and speculative isotherms. A.19
A.9 North-south cross-section B-B' showing formation correlations and speculative isotherms. A.19
A.10 Deschutes Basin in central Oregon and the NEWGEN project area A.20
A.11 Background seismicity within 10 km of NEWGEN FORGE site A.25
A.12 Seismic tomography experiment.. A.27
A.13Underlying one-dimensional P-wave velocity model used in tomogram A.28
A.14 3D seismic travel-time tomographic model of P-wave velocity beneath Newberry Volcano A.29
A.15 Tomographic and seismic waveform modeling interpretation of geologic structure beneath Newberry Volcano on a SW-to-NW profile A.29
A.16 Slices through the shear velocity model at 0.5 and 2.0 km depth, including the independently located seismicity A.31
A.17 Location of MT stations cited by Waibel et al. (2015) A.32
A.18 West-to-east cross section from 2D MT model of Waibel et al. (2015) A.33
A.19 Locations of Davenport MT stations from 2006.. A.33
A.20 OSU 3D resistivity model beneath Newberry Volcano A.35
A.21 Map views of OSU 3D MT resistivity model from combined MT data set.............................. A.36
A.22 Free-air anomaly map A.40
A.23 A cross section through well Pad 29 (upper plot) and 3D perspective view (lower plot) of the higher density bodies responsible of the main observed gravity anomalies modeled for the NEWGEN FORGE site.. A.42
A.24 NWG 55-29 density log along with an averaged log density (red) over specific depths intervals and a comparison to the density values obtained from the gravity inversion A.42
A.25 Equilibrated temperatures of core holes and exploration wells at Newberry Volcano from Frone A.46
A.26 Thermal conductivity versus depth for measured values on cores and cuttings A.47
A.27. Proposed NEWGEN FORGE site... A.50
A.28 Newberry NWG 55-29 wellbore and casing profile. A.52
A.29 Statistics of breakout occurrence in NWG 55-29 .... A.53
A.30 Core samples from Well GEO N-2 from 4219.5 to 4221 ft MDand from 4219.5 to 4221 ft MD showing the location of 1 in. in diameter by 2 in. long sample plugs. A.58
A.31 Well NWG 46-16 completion, geology, and temperature. A.59
A.32 CO_2 gas concentrations measured during drilling on Well NWG 46-16. .... A.61

A.33 Seismic density plot for NWG 55-29 .... A.65
A.34 Summary of measured downhole fluid pressures and hypothesized stress profiles A.66
A.35 Location of the THMC domain superimposed on east-west cross section from Sammel et al. (1988) A.69
A.36 2D cross sections with thermal conductivities and densities used in the thermal model. A.70
A.37 Steady-state thermal model of the western half of the volcano along an east-west cross section of the volcano seen from the north A.71
A.38 Representative geophysical data layers displayed in EarthVision viewed from northwest looking toward southeast A.74
A.39 Two main geophysical units defined by density from 3D gravity inversion A.75
A.40 Geological data layer showing intrusive bodies mapped at the surface or identified through well cores and mud logs, with areas at depth between wells interpolated by assigning bulk petrologic classifications to geophysically defined intrusive bodies A.76
A.41 Well traces colored by gamma ray log values for NWG 55-29 and GEO N-2; NC-01 does not have an available gamma ray log A.78
A.42 West-to-east cross section through geologic data volume as displayed in EarthVision A.79
A.43 Geostatistical analysis of well log porosity, dry density, and thermal conductivity at Wells GEO-N1, GEO-N2, GEO-N4, and GEO-N5 .... A.87
A.44 Cross-dependence structure of collocated porosity, dry density, and thermal conductivity at Wells GEO-N1, GEO-N2, GEO-N4, and GEO-N5. The data are from the depths of 1400 ft to 4150 ft. A.87
A.45 Fitted probability density functions of well log porosity, dry density, and thermal conductivity at GEO Wells N1, N2, N4, and N5. .... A.88
A.46 Fitted probability density functions of thermal conductivity at Well NWG 55-29 (left) and across 15 Newberry wells A.88
A.47 Fitted probability density functions of thermal gradient and permeability across Newberry wells A.88

Tables

A.1 Compilation of stress state data for the study area and neighboring regions. A.10
A.2 Elevation at base of formations in various wells and core holes A.17
A.3 Fluid compositions at locations up-, down- and cross-gradient from the NEWGEN FORGE site, and EPA maximum drinking water standards. A.22
A.4 Physical properties and geometries of the three preferred magma body models. A.30
A.5 Gravity modeling parameters for each of the subsurface structures. A.41
A.6 Thermal gradient and thermal conductivity A.48
A.7 Well data and injectivity test results from nearby Newberry wells and temperature core holes A.49
A.8 Stress model around the NWG 55-29 wellbore. A.54
A.9 Post-emplacement mineral alteration identified in wellbore NWG 55-29. .... A.55
A.10 Summary of elastic, strength, and Mohr-Coulomb properties of GEO N-2 core A.58
A.11 Gas analysis from Well NWG 46-16 .... A.62
A.12 Summary of critical NEWGEN parameters for target reservoir depth. A.80

Acronyms and Abbreviations

1D	one-dimensional
2D	two-dimensional
3D	three-dimensional
4D	four-dimensional
ASL	above sea level
B&R	Basin and Range
BFZ	Brothers fault zone
BHTV	Borehole Televiewer
BP	Before Present
cal/g	calorie(s) per gram
CE	CalEnergy
cfs	cubic feet per second
cm	centimeter(s)
cm^3	cubic centimeter(s)
CO_2	carbon dioxide
COR	Corvallis (seismograph station)
DNH	Davenport Newberry Holdings, LLC
DOE	U.S. Department of Energy
EGS	enhanced geothermal system(s)
EJ	exajoule (s) = 10^{18} joules
EPA	U.S. Environmental Protection Agency
FORGE	Frontier Observatory for Research in Geothermal Energy
ft	foot (feet)
ft^3	cubic feet
g	gravity or gram(s)
GEO	Geothermal Resources International
gpm	gallons per minute
GPS	Global Positioning System
GTO	Geothermal Technologies Office
hr	hour(s)
ka	thousand years ago
K-Ar	potassium-argon
KFO	Klamath Falls (seismograph station)
kg	kilogram(s)
kJ	kilojoule(s)
kJ/(kg.K)	kilojoule(s) per kilogram per kelvin

km	kilometer(s)
kph	kilometer(s) per hour
L	liter(s)
lb	pound(s)
LiDAR	light detection and ranging
M	(earthquake) moment magnitude
m	meter(s)
m^3	cubic meter(s)
Ma	million years ago
mD	miliDarcy(ies)
mGal	milligal(s)
mi	mile(s)
M_L	Richter-magnitude-scale
MMI	Modified Mercalli Intensity
MPa	megaPascal
MSA	microseismic array
MT	magnetotelluric(s)
nD	nanoDarcy(ies)
NEGSD	Newberry Enhanced Geothermal Systems Demonstration
NETL	National Energy Technology Laboratory
NEWGEN	Newberry Geothermal Energy
ODWR	Oregon Department of Water Resources
OSU	Oregon State University
PNSN	Pacific Northwest Seismic Network
ppm	parts per million
psi	pounds per square inch
psig	pounds per square inch gauge
PT	pressure-temperature
RTK	Real-Time Kinematic
s	second(s)
Sandia	Sandia National Laboratory
S_{hmin}	minimum horizontal stress
S_V	stress near vertical
TCH	temperature core hole
TD	total depth
THMC	Thermal-Hydrological-Mechanical-Chemical (model)
TMD	total measured depth
TVD	true vertical depth

uGal	microgal(s)
USGS	United States Geologic Survey
W/(m.K)	watt(s) per meter per kelvin
WHP	wellhead pressure
yr	year(s)

Appendix A

Conceptual Geologic Model

A.1 Summary

Newberry Geothermal Energy (NEWGEN) presents a robust Conceptual Geologic Model to support the establishment and management of the proposed Frontier Observatory for Research in Geothermal Energy (FORGE) on the western flank of the Newberry Volcano. Through this Conceptual Geologic Model, NEWGEN demonstrates that the site

- has ideal temperature profiles at suitable depth, validated by measurements in multiple deep wells (~3 km),
- meets the requirements for low permeability and absence of hydrothermal activity within the site,
- has an enormous reservoir of heat with 2.4 GW potential (representing 40 percent of Oregon's total electricity consumption for 30 years),
- builds on 40+ years of intensive characterization of Newberry Volcano, and
- has reduced geological uncertainties based on existing wells and a known seismic response to injection based on more than 4 years of microseismicity data.

The Conceptual Geologic Model for the NEWGEN FORGE site provides a unified framework where NEWGEN FORGE *identifies the target reservoir units*, constrains their *spatial extent*, and characterizes properties of relevance to enhanced geothermal systems (EGSs). In the conceptual model, the *temperature profile* within the target reservoir units is constrained by borehole equilibrium temperature measurements from deep wells, backed by thermal conductivity measurements of rock cores and cuttings, diffusive heat flow models, and coupled Thermal-Hydrological-Mechanical-Chemical (THMC) Models that make use of *constraints on porosity and permeability* obtained from measured well data, bulk permeability data, and injectivity test data. Additional constraints on porosity and permeability were inferred from seismic and magnetotelluric models. *Fluid content* at the NEWGEN FORGE site is limited to a shallow aquifer or aquifers that extends to depths of 150 to 300 m below ground surface, beneath which increasing alteration of the volcanic minerals to clays, zeolites, and other moderate temperature minerals decreases permeability substantially to form a thick low-permeability zone, as observed in cores, well logs, mud logs, and low electrical resistivity values. *Structural characteristics* have been defined by decades of geologic studies as well as by recent high-resolution LiDAR (light detection and ranging) mapping, by seismic tomographic and waveform modeling, and by magnetotelluric and gravity inversions. The site lithology and petrology have been defined by cores, well and mud logs, and surface sampling, and geophysical models provide a basis for interpolating between well-ties. The *stress regime* has been evaluated by regional seismic focal mechanism studies, by interpretation of faults and volcanic features aligned along structural controls, borehole breakouts, and the Newberry Enhanced Geothermal Systems Demonstration (NEGSD) stimulations. The Conceptual Geologic Model is intended to be a dynamic rather than static view of conditions in and surrounding the NEWGEN FORGE site. As a FORGE Phase 1 deliverable, it is intended to demonstrate the suitability of the site based on the characterization undertaken to date, but it also highlights areas of greater and lesser uncertainty, providing guidance for additional characterization work during Phase 2 of the FORGE project.

During FORGE Phase 1, NEWGEN has developed a coherent and self-consistent understanding of the target reservoir depth, temperature profile, thermal conductivity, fluid chemistry, permeability and porosity, structure and lithology of the target formation, regional and in situ stress directions, extent of microseismicity, transmissivity, and impedance/injectivity. This process has guided the thinking about where there may be shortcomings in the existing data sets and models, and how they could be addressed during the next phase of the FORGE program. The assimilation and coregistration of such a diverse data set was done using the EarthVision™ software environment for three-dimensional (3D) model building, analysis, and interpretation. The ultimate goal is to merge the geophysical and geological data volumes into an EGS parameter visualization volume that would delineate the parameters most directly governing EGS potential (e.g., permeability, stress field, injectivity, etc.). A summary of these parameters and their uncertainties are quantified in the conceptual model.

Important constraints on the suitability of the NEWGEN site to implement FORGE were derived from the NEGSD project, which created a fracture network during a successful EGS stimulation. Critical measurements of injectivity, extensive microseismic monitoring and measurements of induced seismicity, complementary surface geophysical data sets obtained during monitoring efforts, and comparisons between predicted stress and the mechanical response of the stimulation efforts have provided confirmation that conditions near NWG 55-29 meet FORGE requirements.

At NWG 55-29, the full span of FORGE target temperatures of 175ºC to 225ºC are reached at depths from 1472 m to 1892 m. This depth range is contained in a basaltic andesite-basalt unit bounded on the bottom by a welded lithic tuff, both within the John Day Formation. At the adjacent NWG 46-16 (the northeast NEWGEN FORGE pad), the full FORGE target temperature range is projected to be reached at depths from 1752 m to 2182 m. This depth range is contained within tuff + debris flow + andesite, rhyolitic tuff, and tuff + andesite units of the Mascall Formation. Thermal modeling predicts that at Pad 17 the temperature depth range is projected to be contained within the John Day Formation, but no well has been drilled at that pad to confirm the lithology or temperature. On thermal grounds, the target formation volume is therefore contained within depths of ~1472 m (shallowest at NWG 55-29) to ~2682 (deepest at well Pad 17), providing the full FORGE temperature range of 175 to 225°C. Here we assume that the thermally defined target formation volume spans (but is not limited to) a 1000 m radius around each of the potential NEWGEN FORGE drilling sites; therefore, 3.14 km^2 (780 acres) per pad and 9.4 km^2 (2340 acres) total. The thickness of the target formation volume is ~420 m to 450 m throughout that area. Taking an average value of 435 m of formation volume thickness, and the NEWGEN FORGE surface area of 9.4 km^2, the total target formation volume is 4.1 km^3, representing a very large heat reservoir.

The NEWGEN FORGE site also has very low permeability and porosity, making it ideal for testing EGS technologies. The results of injection tests at wells in the vicinity of the NEWGEN FORGE site reveal injectivity several orders of magnitude lower than the lowest permeability geothermal wells found in other hydrothermal fields. Unlike hydrothermal projects, the very low permeability found at depth on the flanks of Newberry Volcano is a desirable feature for EGS advancement, allowing development of a closed hydraulic circuit. All of the wells demonstrated injectivities several orders of magnitude lower than the lowest permeability of typical geothermal producers such as Coso and the Salton Sea range.

A.2 Geological and Geophysical Context of the Western Flank of Newberry Volcano

A.2.1 Data Sources

Geologic exploration and discovery data collected over the past 40 years from Newberry Volcano and the surrounding region were integrated into a model of the geologic conditions underlying the proposed NEWGEN FORGE site. The specific types and sources data used are detailed in Appendix D, the Site Characterization Data Inventory. Quantified geologic information and measured data trends such as temperature and permeability as a function of depth and areal extent provided guides for estimating the resource parameters over the extent of the NEWGEN FORGE site. The parameter values for the Conceptual Geologic Model and the uncertainties on those parameters are summarized in Section A.4 and A.5 of this Appendix.

Three large projects funded by the U.S. Department of Energy (DOE) have been performed on the proposed NEWGEN FORGE site in the past 6 years by NEWGEN Consortium members. AltaRock Energy, Inc. (Altarock) led the NEGSD,[1] Davenport Newberry Holdings (now part of AltaRock), led an Innovative Exploration Technology project,[2] and Oregon State University (OSU) with the National Energy Technology Laboratory (NETL) and Zonge International carried out a four-dimensional (4D) EGS monitoring project[3] to complement the NEGSD. These projects resulted in the collection of a wealth of new data that are directly relevant to the NEWGEN FORGE site.

The NEGSD project was performed in three phases separated by Go/No Go decisions. Each phase included a major report that is now publicly available; Phase 1 report (AltaRock 2011), Phase 2.1 report (AltaRock 2014), and Phase 2.2 report (AltaRock 2015). Two master's degree theses at The School for Renewable Energy Science at the University of Iceland and the University of Akureyri were directly related to the geothermal well used for NEGSD—Letvin (2011) and Fetterman (2011). At least one conference paper was presented each year during the project to inform the scientific community of NEGSD progress; at the Stanford Geothermal Workshop (Cladouhos et al. 2011a, 2012, 2013a, 2015a; Petty et al. 2013), the annual meetings of the Geothermal Resources Council (Osborn et al. 2011; Cladouhos et al. 2011b, 2015b), and American Rock Mechanics Association (Cladouhos et al. 2013b). Abstracts and posters were presented at the American Geophysical Union annual meeting (Grasso et al. 2013, 2014). NEGSDS papers published in peer-reviewed journals include those by Templeton et al. (2016), Fang et al. (2015), and Cladouhos et al. (2015c).

The final report of the Davenport Innovative Exploration Technology project, by Waibel et al. (2015), can be found in the Geothermal Data Repository. In addition, the Davenport project produced a PhD thesis at Southern Methodist University (Frone 2015).

The 4D EGS monitoring project is still active, publications are in preparation, and it is supporting the PhD thesis research of OSU student Esteban Bowles-Martinez. Conference presentations include those by Schultz et al. (2012, 2013, 2014) and Schultz (2013a), and a Stanford Geothermal Workshop paper was presented by Mark-Moser et al. (2016). Project content from the 4D EGS monitoring project was an important component of a briefing to the JASON Scientific Advisory Group on behalf of DOE's Geothermal Technologies Office (GTO) (Schultz 2013b). Project presentations also included GTO Peer Reviews in 2013 and 2015.

A.2.2 Geography

The Newberry Volcano is located in Deschutes County, Oregon, approximately 50 km (31 mi) east of the crest of the Cascade Range. The volcano is situated within the Eastern Cascades Slopes and Foothills ecoregion, as designated by the U.S. Environmental Protection Agency (EPA), though the mountain itself is characterized as Cascade Crest Montane Forest. The nearest major city is Bend, Oregon (population of ca 81,000), located about 35 km (22 mi) north of the volcanic center. Tourism is a major source of revenue for the city, as Bend provides close access to many recreational activities including skiing,

[1] EE0002777 Newberry EGS Demonstration Project

[2] EE0002833 Validation of Innovative Exploration Technologies at Newberry Volcano

[3] FY11 AOP 1.1.1.13 Novel use of 4D Monitoring Techniques to Improve Reservoir Longevity and Productivity in Enhanced Geothermal Systems

hiking, biking, and rock climbing. Other populations near Newberry include Three Rivers (population ca 2400) and La Pine (population ca 1700), and the resort community of Sunriver (population ca 1300).

A.2.3 Regional Setting

Newberry Volcano is situated near the juncture of three geologic provinces in central Oregon: the Cascade Range and volcanic arc to the west, the Columbia Plateau to the northeast, and the Basin and Range to the southeast (Figure A.1). The Cascade Arc is a long-lived feature with a magmatic history including several prominent eruptive periods, Western Cascades from 35 to 17 Ma, the early High Cascades from 7.4 to 4.0 Ma, and the late High Cascades from 3.9 Ma to present (Priest 1990). Formation of the Cascades results from the subduction of the Juan de Fuca plate beneath the North American plate, occurring at a rate of 3.0 to 4.5 cm/yr (Wilson 1993). Modern volcanic features include large stratovolcanoes such as Mount Jefferson at 3199 m (10,495 ft), Mount Bachelor at 2764 m (9068 ft), and the Three Sisters at 3062 to 3159 m (10,046 to 10,364 ft), as well as many smaller domes and mafic vents. The Columbia Plateau is one of the largest flood basalt plateaus on Earth, extending between the Cascade Range and the Rocky Mountains and covering about 160,000 km^2 (61,776 mi^2) of the Pacific Northwest. The Basin and Range province is a broad physiographic and geologic region characterized by alternating narrow faulted mountain ranges (horsts) and flat arid valleys or basins (grabens) that developed as a result of crustal extensional that began in Early Miocene time.

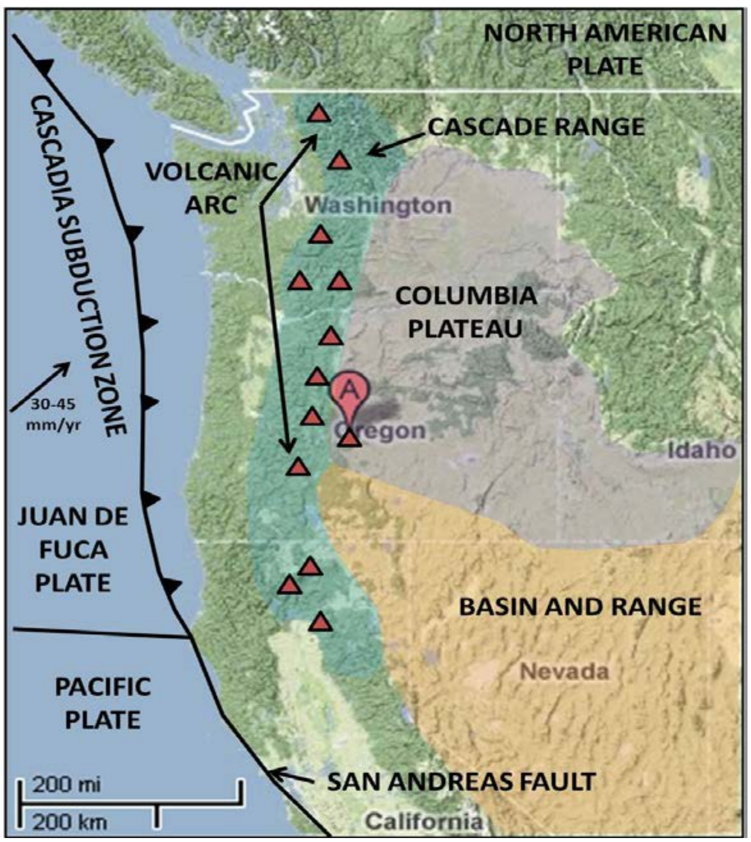

Figure A.1. Tectonic boundaries and geological provinces of the Pacific Northwest. Red triangles represent major volcanic centers of the Cascade Arc ("A" is Newberry Volcano). Blue, purple, and orange regions represent the Cascade Range, Columbia Plateau, and Basin and Range provinces, respectively. The bold black lines represent tectonic plate boundaries: the Cascadia Subduction Zone to the north and the San Andreas Fault to the south, and the east-west Mendocino Transform Fault (unlabeled) separating the Pacific and Juan de Fuca plates.

Oblique subduction of the Juan de Fuca plate beneath North America has produced a complex tectonic setting for the Pacific Northwest (Figure A.2). Neogene deformation, paleomagnetic rotations, and geodetic data suggest the Cascadia forearc (defined as the area between the plate boundary and volcanic arc) is migrating northward along the coast and breaking up into large rotating blocks (Wells et al. 1998). Deformation occurs mostly around the margins of a large, relatively aseismic Oregon coastal block composed of thick, accreted seamount crust (Wells et al. 2014). This 400 km (249 mi) long block rotates clockwise with respect to North America around a pole of rotation (i.e., a Euler pole) in eastern Washington. Extensional deformation in the Basin and Range and contractional deformation in the Yakima fold belt accompanies the clockwise rotation of this forearc block in the south and north, respectively (Figure A.2) (Wells et al. 1998). Newberry Volcano and the volcanoes of the High Cascades in central and southern Oregon and northern California formed along the trailing, eastern edge of the Oregon coastal block (Schmidt et al. 2008; Wells et al. 1998; Wells and McCaffrey 2013).

Newberry Volcano formed in the northwest corner of the Oregon Basin and Range extensional province (Jensen et al. 2009; MacCleod et al. 1995; Williams 1935). Cenozoic extension created the vast Basin and Range province, a region of distributed normal faulting in the North American plate (Wernicke 1992). The extensional province impinges on the Cascade Arc at the extreme northwestern corner of the Basin and Range (B&R) region (Figure A.3). Newberry Volcano occupies a structural position to the east of Cascade Arc faults and to the west of the B&R faults, including the Brothers fault zone (BFZ) (Jordan et al. 2004; Lawrence 1976; Meigs et al. 2009; Wells and McCaffrey 2013). Whereas east-west extension on north-trending normal faults characterizes deformation in the volcanic arc (Priest 1990; Sherrod and Scott 1995; Sherrod and Smith 2000; Sherrod et al. 2004; Taylor 1990), northwest-trending down-to-the-northeast normal faulting occurs in the BFZ (Lawrence 1976; Meigs et al. 2009; Trench et al. 2012). North- to north-northeast-trending faults dominate the B&R structural fabric (Crider 2001; Donath 1962; Pezzopane and Weldon 1993; Scarberry et al. 2010). This structural setting, near the transition from the B&R to the Cascades, has influenced the origin and history of Newberry Volcano.

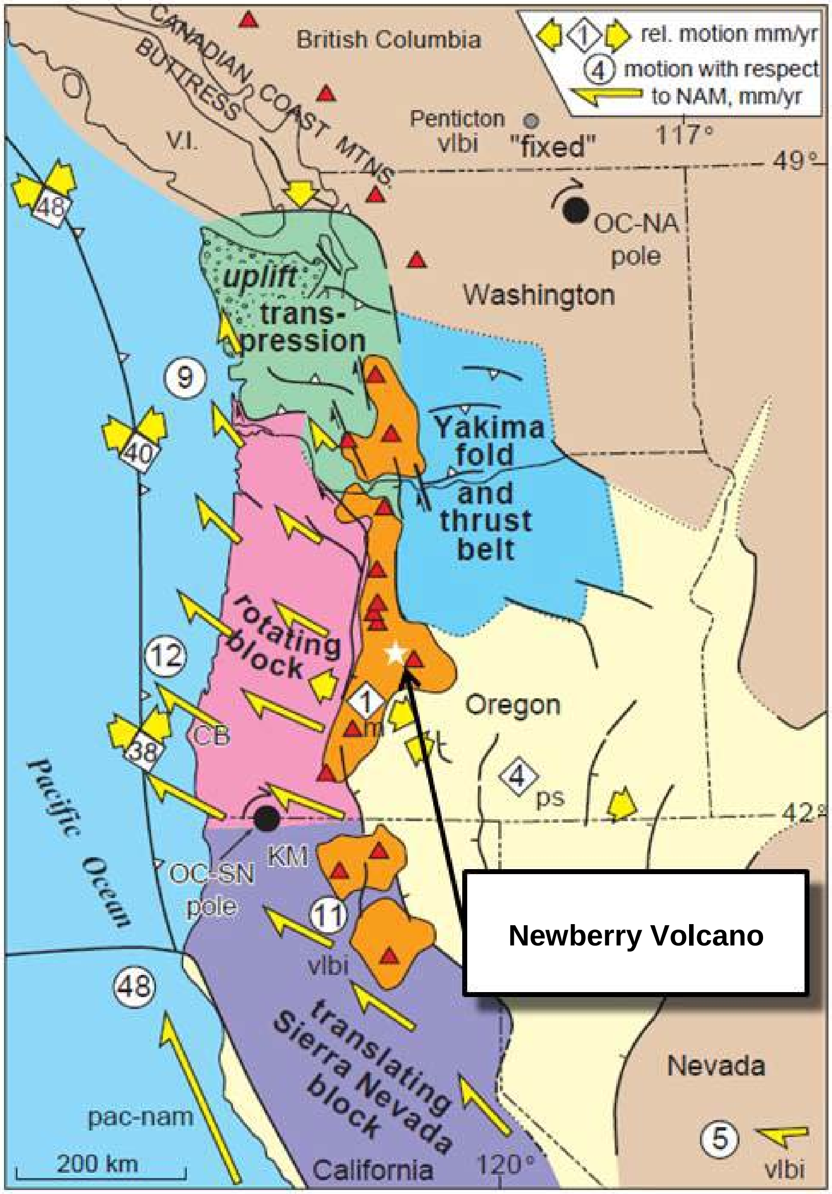

Figure A.2. Block motions for Cascadia forearc proposed by Wells et al. (1998). The Oregon coastal block (pink) rotates clockwise due to northwest translation of the Sierra Nevada block (purple). Extension in the Cascade Volcanic Arc (orange) and Basin and Range (yellow) occurs along the trailing (east) edge of the Oregon coastal block. Contraction, crustal shortening, and thrust faulting occur in the Washington forearc (green) and the Yakima fold belt (blue) as the north end of Oregon block impinges on southern British Columbia.

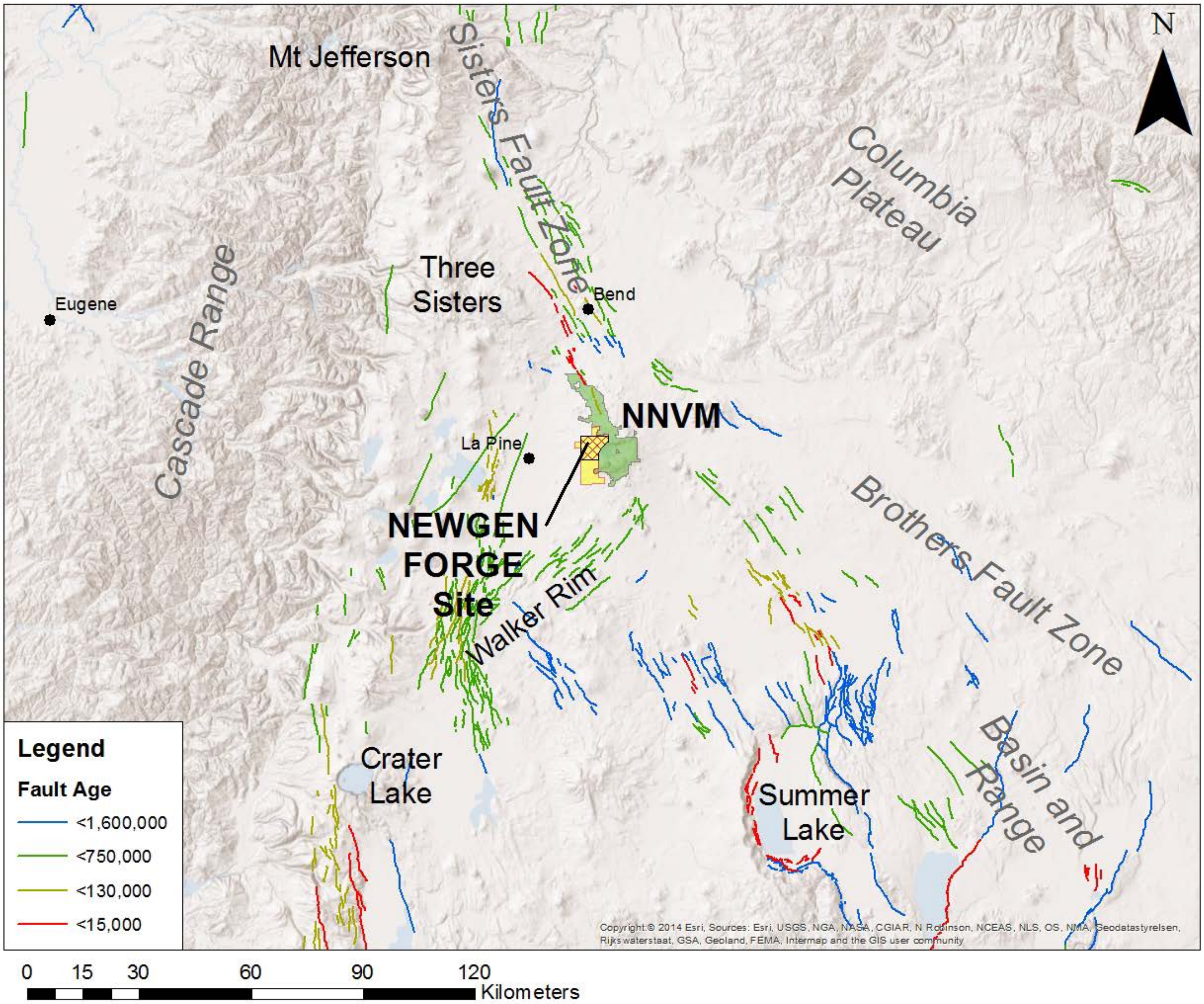

Figure A.3. Regional fault map showing the location of the NEWGEN FORGE site and the intersection of principal structural trends in Central Oregon. North-trending faults bound the west side of the Cascade Arc in the south. North- and northeast-trending faults at Walker Rim extend northeastward into the southern flank of Newberry. North-northwest-trending faults of the Sisters fault zone extend from the Mt. Jefferson area near the top of the figure to the southeast through Bend into the north flank of Newberry Volcano, where it is expressed at the surface as the Northwest Rift zone (MacLeod and Sherrod 1988; McKay et al. 2009; Sherrod et al. 2004). Color coding characterizes fault activity (U.S. Geological Survey [USGS] Quaternary fold and fault database).

Faults with two orientations cut the Newberry Volcano and owe their existence to two discrete processes (Figure A.4). Northeast-, north-, northwest-trending faults, and faults related to caldera formation have been recognized since the earliest investigations of the volcano (Jensen et al. 2009; MacCleod and Sherrod 1988; MacCleod et al. 1995; McKay et al. 2009; Williams 1935). One set of structures formed in response to volcanic and caldera-related processes of the volcano itself. Arcuate vents and ring fractures parallel the north rim of the central caldera (MacCleod and Sherrod 1988; MacCleod et al. 1995; Williams 1935). First recognized by Williams (1935), four caldera ring fractures occur on the northwest flank of Newberry Volcano (Figure A.4, red and orange) (MacCleod et al. 1995).

Tectonically related northwest- and northeast-trending faults compose the second group of structures (Figure A.4, blue and yellow). On the southern flank of the volcano, the northeast-trending Walker Rim fault projects beneath the volcanic edifice (Figure A.3) (MacCleod et al. 1995). In the north, the Sisters fault zone, including the Tumalo fault, projects from the Mt. Jefferson region of the Cascade Arc southeasterly into the northern flank of Newberry Volcano (MacCleod and Sherrod 1988; MacCleod et al. 1995; McKay et al. 2009; Sherrod et al. 2004). A diffuse zone of fissures, cinder cones, fractures, known as the "Northwest Rift zone" (McKay et al. 2009), crops out on the north flank of Newberry Volcano. A fissure eruption along the Northwest Rift zone at ~7 ka produced a number of mafic flows and cinder cones, including the Lava Butte flow and cone (McKay et al. 2009). Tectonic faults that cut the Newberry massif occur as part of the structural transition between the Cascade Arc and the B&R extensional province. Flows from the fissure eruption ponded against fault scarps near Lava Butte (MacLeod and Sherrod 1995; McKay et al. 2009), which indicates that they existed prior to eruption. Whereas the northwest-trending BFZ crops out ~10 km to the north of Newberry Volcano, the Brothers faults likely do not deform the volcano given that a ~400 ka lava flow sourced from Newberry Volcano buries the northwestern end of the fault zone (MacCleod et al. 1995).

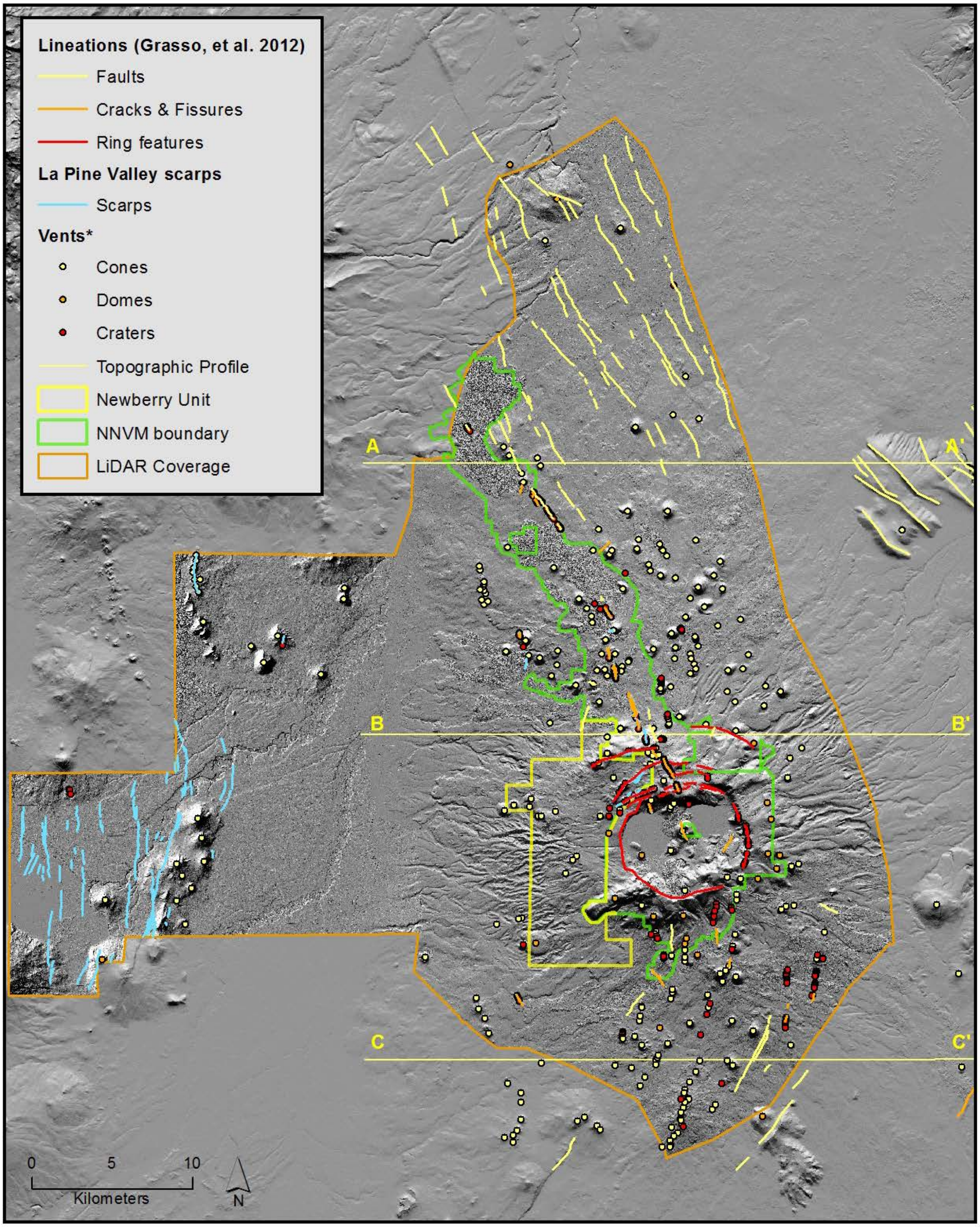

Figure A.4. LiDAR-based digital elevation mapping indicates the regional fault fabric and volcanic landforms at Newberry Volcano (Grasso et al. 2012). Topographic profile lines A-A’, B-B’, and C-C’ of Figure A.5 are shown.

A.2.4 Regional Stress Orientation

Crider (2001) inverted seismic event data south of Newberry Volcano for stress directions using focal mechanisms from earthquakes with moment magnitudes (M) greater than 4.0. The solution yields a stress tensor with: 1) the least compressive stress sub-horizontal ($S_{hmin} = \sigma_3$) and oriented east-west or slightly east-northeast to west-southwest (264° ±29°); 2) the greatest compressive stress near vertical ($S_V = \sigma_1$); and 3) the intermediate stress approximately north to south ($S_{Hmax} = \sigma_2$). Other geologic stress indicators including dikes, cinder cones, and normal faults yield stress directions within the study area that are consistent with the results of this focal mechanism stress inversion. A compilation of additional stress state data in central Oregon is provide in Table A.1.

Table A.1. Compilation of stress state data for the study area and neighboring regions.

AUTHOR	LOCATION	DATA SOURCE	NOTES[a]
Braunmiller et al. 1995	Klamath Falls, Southern OR	Focal Mechanism Solutions	Both E-W Normal Faulting (90°) and NE-SW Strike-Slip Faulting (60°)
Crider 2001	Summer Lake, S. Central OR	Focal Mechanism Solutions	σ_1 = 241/62, σ_2 = 349/10, σ_3 = 084/26 Oblique Normal Fault Regime, M > 4
		Cinder Cone Alignments	Paleo Stress (Late Mio.-Recent), NW-NNW Extension ~244°
		Earthquake T-Axes	1999 Christmas Valley Earthquake, E-W Extension ~263°
		Dike Alignments	Paleo stress (Late Mio.-Plio.), ENE-WSW Extension ~256°
Humphrey and Coblenz 2007	West Coast United States	World Stress Map	Northern Oregon: Thrust (003°) Southern Oregon: Strip-Slip (σ_1= 028, σ_3 = 118)
McCaffrey et al. 2013	South Central Washington	Focal Mechanism Inversion and GPS	σ_1 = 004-012/03-13, σ_2 = 095-106/06-03, σ_3 = 248-260/57-80. thrust fault regime
Pezzopane and Weldon 1993	Northern and Southern OR	Focal Mechanism Inversion	Northern Oregon: σ_1 = 281/71, σ_2= 044/10, σ_3 = 137/15; Southern Oregon: σ_1 = 012/20, σ_2 = 206/70, σ_3 = 104/05
Werner et al. 1991	Central WA & Central OR	Borehole Breakouts, Vent Alignments, Focal Mechanisms	Columbia Basin: Focal Mechanisms (NNE Compression), Central Cascades: Vents (NNW or N-S Compression)

σ_1 = maximum principal stress, σ_2 = intermediate principal stress, σ_3 = minimum principal stress.
Principal stress values are shown as azimuthal trend (degrees from north) and plunge (degrees from trend).

A.2.5 Faulting Expressions

The high-resolution topographic LiDAR data (Figure A.4) allow for better characterization of the La Pine graben faults shown in the USGS fault and fold database at the western edge of the La Pine Valley (Personius 2002a), the volcano's ring fractures (Personius 2002b), and determination of whether active faults or fractures occur near the NEWGEN FORGE site. Analysis of the 880 km^2 (229 mi^2) of LiDAR data is shown in Figure A.4 and discussed in detail by Cladouhos et al. (2011b). The ring fractures mapped in the USGS database (red in Figure A.4) are expressed as curved lineaments defined by fissures and an alignment of vents. Dip-slip fault offset along the ring fractures is not observed in the LiDAR surfaces. Formation of the ring fault system at ~80 ka seems probable given that the caldera-forming eruption is thought to have occurred at ~80 ka (Jensen et al. 2009). The ring faults are not expressed in a post-eruptive andesitic tuff (MacLeod and Sherrod 1995) that mantles the western flank of the volcano. Thus, the lack of surface scarps in the LiDAR data, the absence of faults in the andesitic tuff, and the association of the ring fracture system with the caldera-forming eruption implies that the ring faults are not part of an active fault system.

Potentially active faults bound the west side of the La Pine graben. LiDAR reveals a series of short (<6 km [<3.7 mi]), discontinuous scarps interpreted to be normal faults bounding nested grabens with associated lava flows and cinder cones (light blue in Figure A.4). The USGS fault and fold database includes many of these faults, but in less detail. The USGS database also includes two long (30 and 35 km [18 and 22 mi]), NNE-trending faults in the La Pine graben west of La Pine (green lines in Figure A.3). However, no evidence of these longer faults can be seen in the LiDAR data (Figure A.4). This is not surprising, as the notes in the USGS database for these faults indicate that "… the graben margin faults inferred from the gravity data by Ake et al. (2001) have no topographic expression or demonstrated offset in Quaternary deposits" (Personius 2002a). Examination of the maps and figures in Ake et al. (2001) confirms that these faults are drawn on the basis of inflections in gravity profiles.

A.2.5.1 Stress on Newberry

Closer to Newberry Volcano, the strike of normal faults and extensional vents or fissures mapped with LiDAR provides a first approximation of the local S_{hmin} direction that will influence EGS creation at the NEWGEN FORGE site. The fault scarps on the west side of the La Pine Valley cut modern alluvial sediments and are considered to be younger than 130 ka (Personius 2002a). The youngest vents and fissures are part of the Northwest Rift and must be younger than 7 ka because they were conduits for basalt flows that overlie the Mazama ash erupted between 6600 and 6700 ^{14}C years Before Present (BP) (MacLeod et al. 1981).

The average fault orientation on the west side of the La Pine graben (light blue in Figure A.4) and the average fissure orientation in the rift zone differ by only about 10° (Cladouhos et al. 2011a). This suggests a normal fault regime with roughly east-west extension. This inferred regional stress orientation is simpler than might be expected for Newberry Volcano based on the diversity of fault orientations regionally (Figure A.3). An east-west extensional stress regime is consistent with stress analyses based on faults, fissures, earthquake focal mechanisms, and data in the World Stress database (Braunmiller et al. 1995; Crider et al. 2001; Donath 1962; Humphreys and Coblentz 2007; Pezzopane and Weldon 1993). This conclusion is further supported by the analysis of borehole televiewer (BHTV) data (Section A.2.11.1 Conditions at Pad 29 from the Well NWG 55-29 Wellbore) acquired in NWG 55-29 that shows similar stress directions and fracture populations.

Grasso et al. (2012) characterized the interrelationship between structure and volcanic landforms using LiDAR mapping of fault scarps and volcanic vent alignments across the Newberry Volcano edifice (Figure A.4). Fault orientation south of the caldera reflects the north-northeast to south-southwest structural grain of the Walker Rim fault zone. Strike changes to north-northwest to south-southeast trending faults and fissures north of the caldera. Extension in the east-west direction is evidenced by topographic down-step from east to west across the edifice of several hundred meters (Figure A.5). Volcanic vents, cinder cones, and fissures are common in the area and appear to be aligned with fault orientations in many areas. The frequency and volume of eruptive material including significant volcanic ash production may obscure the surface expression of some features.

A.2.6 Geomorphology

Newberry Volcano is a broad shield volcano (Williams 1935) that has been active for approximately the last 600,000 years (MacLeod et al. 1982; Jensen 2006). The volcano constructed an elliptically shaped massif approximately 50 km by 30 km (31 mi by 19 mi), and some lava flows reach more than 64 km (40 mi) to the north of the caldera (Figure A.6) (Jensen et al. 2009). Infrequent, widely distributed boulders with exotic lithologies interpreted to be glacial erratics (Donnelly-Nolan and Jensen 2009) may indicate the presence of a glacier at the summit prior to the cataclysmic eruption at ~80 ka. The more gently sloped lower flanks are composed of ash and lahar deposits, basaltic lava, cinder cones, and minor silicic domes. Several basalt flows sourced from the Northwest Rift are younger than 7000 years, the age of the regionally extensive Mazama ash from Crater Lake (McKay et al. 2009). The more steeply sloped upper flanks of the volcano are composed predominantly of overlapping silicic domes and subordinate basaltic rock. The central caldera, which is about 8 km by 5 km (5 mi by 3 mi), is a nested composite of craters and vents and contains two lakes: Paulina Lake on the west at an elevation of 1930 m (6332 ft) and East Lake on the east at an elevation of 1941 m (6365 ft). Paulina Lake is drained by the west-flowing Paulina Creek, the only perennial surface water found on the flanks of the edifice. Within the caldera are resurgent obsidian flows, cinder cones, and maars. The Big Obsidian Flow and other features represent the most recent eruptions, which occurred between 1.6 ka and 1.3 ka. The elevation of the rim of the caldera ranges from 2133 to 2408 m (6998 to 7900 ft), except along the breached western side, where the elevation is 1929 m (6329 ft).

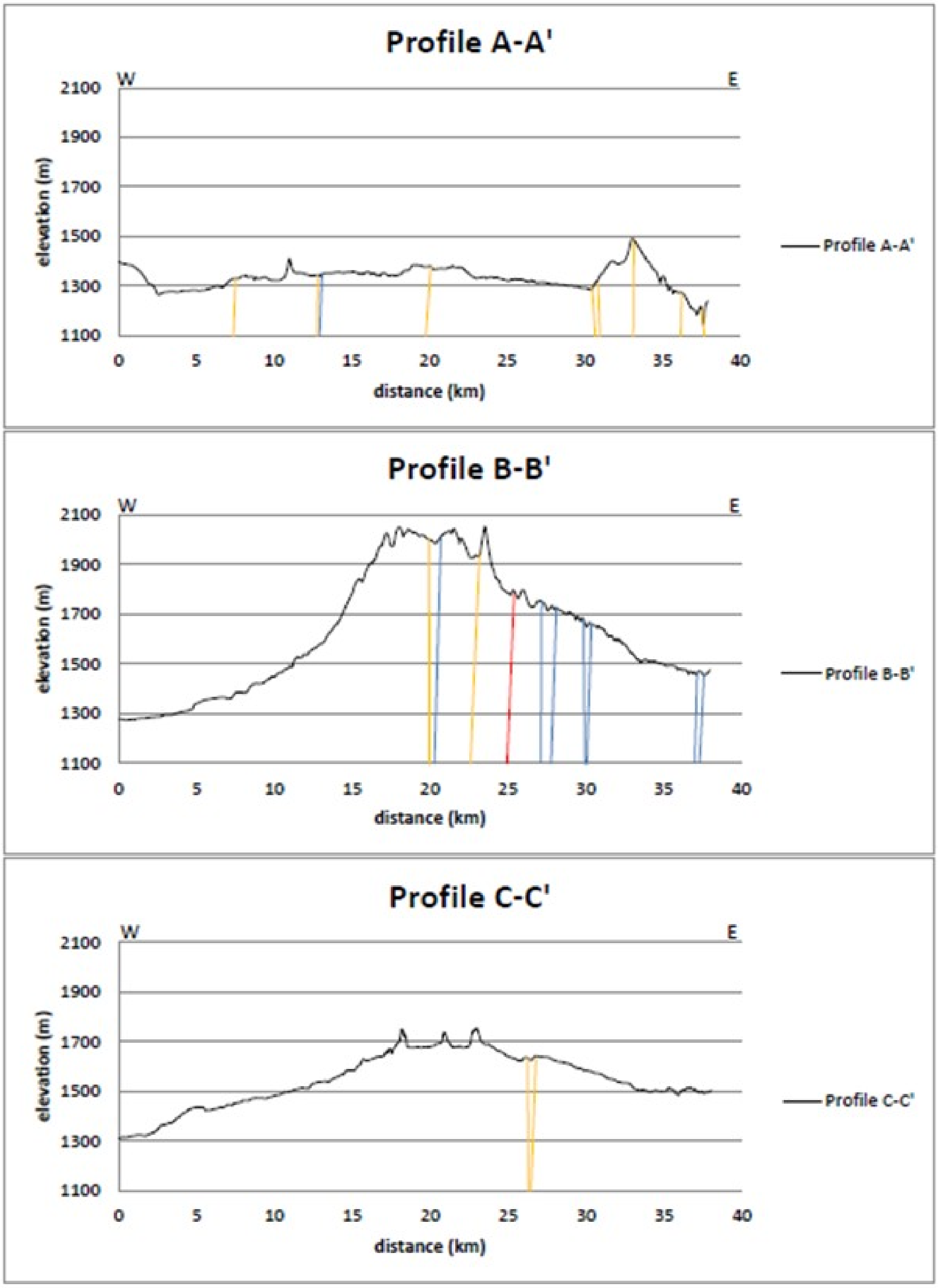

Figure A.5. Topographic profiles A-A', B-B', and C-C' (profiles are marked in Figure A.4) showing projected structural features below the Newberry Volcano edifice, from Grasso et al. (2012). Vertical exaggeration ~16x.

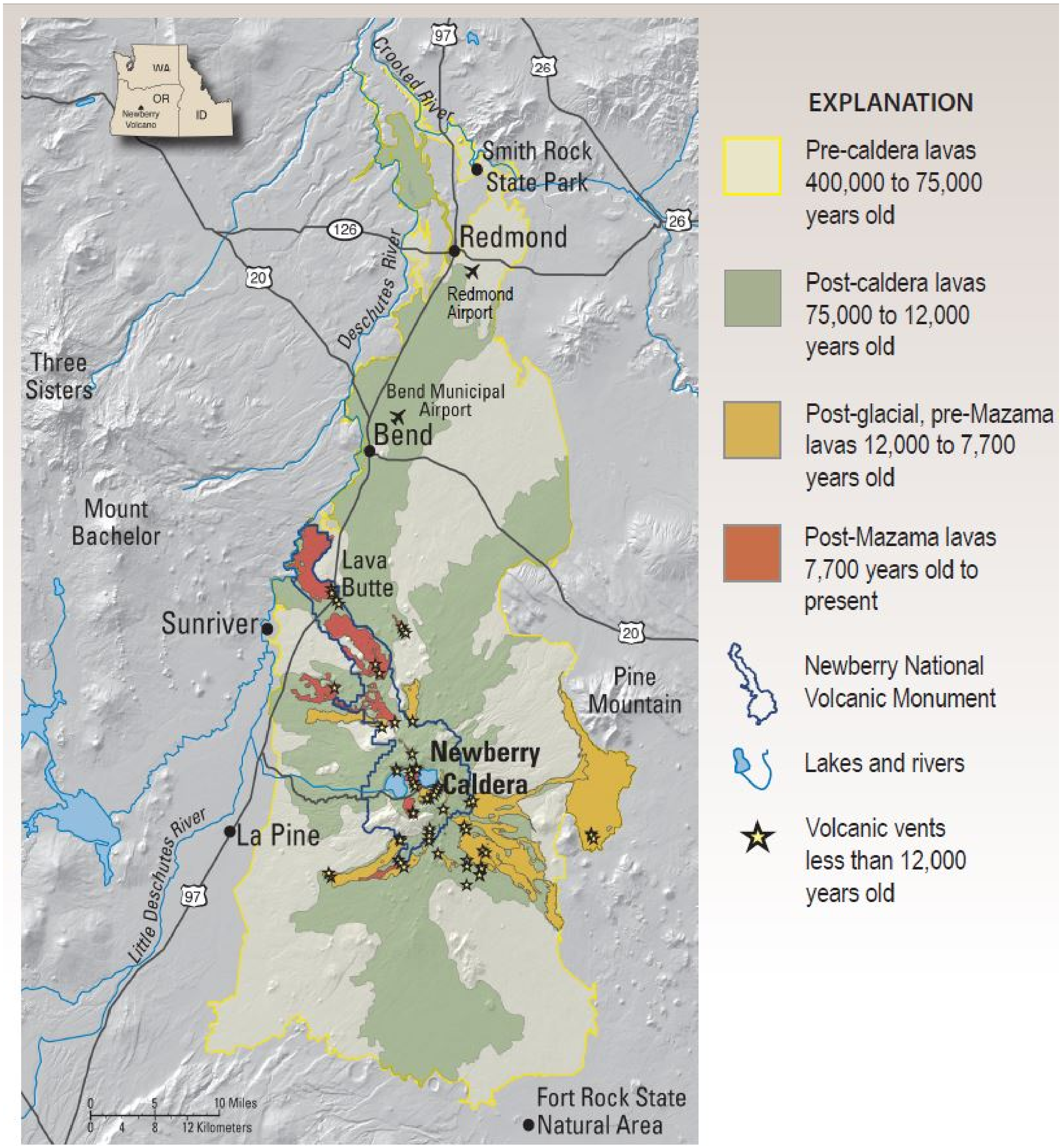

Figure A.6. Lava flows and young volcanic vents at Newberry Volcano. The USGS continues to study and monitor the area (from Donnelly-Nolan et al. 2011).

Due to the porous nature of the surface material on the flanks of Newberry Volcano, little modern fluvial erosion or deposition occurs except at Paulina Creek, or after heavy rainfall or melt events (Donnelly-Nolan and Jensen 2009). Soil development is fairly limited in the 1 to 3 m (3.3 to 9.8 ft) of ~7 ka Mazama ash that blankets the edifice, and does not play a fundamental role in understanding the geothermal aspect of the project area.

The USGS is actively seeking to understand the evolution and growth of Newberry Volcano because it has erupted within the past 1500 years. Recent work and ongoing monitoring work is summarized on a USGS Fact sheet available for download (Donnelly-Nolan et al. 2011). Figure A.6 summarizes Newberry volcanic flows relative to local communities and roads. A complete detailed Geologic Map of Newberry will be published by the USGS after final field checking, map compilation, and production (J. Donnelly-Nolan pers. comm. 2016). Other ongoing work by the USGS includes the following (J. Donnelly-Nolan, pers. comm. 2016):

- Argon dating is ongoing and additional samples will be collected during summer 2016.
- Additional paleomagnetic sampling for correlation purposes is planned for summer 2016.
- Tephra studies that are mostly focused on the approximately 75-ka caldera-forming eruption will continue at least through 2016.
- A revised and updated field guide to Newberry Volcano is in progress and publication is planned to coincide with the International Association of Volcanology and Chemistry of the Earth's Interior meeting to be held in Portland, Oregon, in August 2017.
- Dating of granitic intrusions and drill hole samples from NWG 55-29 using zircons is an ongoing master's thesis project.

A.2.6.1 Volcanic Stratigraphy

Analyses of surface rock samples show a wide range of igneous rock compositions, dominated by a bimodal concentration of basaltic andesite and rhyodacite. Hundreds of volcanic vents and fissures are located on and adjacent to the volcano, some of which pre-date Newberry Volcano. Data from MacLeod et al. (1982), and from deeper temperature core holes (TCHs), suggest that the early eruptive history of the edifice was dominated by mafic lava. Over time, the magmatic character changed to the current bimodal basaltic andesite and rhyodacite. The Newberry flows are deposited on older volcanic and clastic sequences, most of which do not outcrop locally.

The descriptions of the geologic units, presented below in order from youngest (shallowest) to oldest (deepest), were used to generate the cross sections (Figure A.7, Figure A.8, Figure A.9). Subsurface conditions are derived from the numerous TCHs and geothermal exploration wells that have been drilled at Newberry Volcano since the 1970s by both the private and public sectors. Early work was conducted by Occidental Petroleum (Santa Fe Geothermal), Phillips Petroleum, Sunedco, USGS, Sandia National Laboratory (Sandia), Geothermal Resources International (GEO), Union Oil, and CalEnergy (CE) Exploration.

Formation dates described below are derived from various reports from around the region. No existing downhole geochronology is currently available for the Newberry edifice. Katie Sullivan, of the USGS in Menlo Park and San Francisco State University, is using zircon from granodiorite in Well NWG 55-29 cuttings to date suspected Newberry-aged intrusion as part of her master's thesis. Whole rock geochemistry from borehole cuttings on the western flank of the edifice was acquired as part of Davenport's DOE-funded innovation exploration project by Waibel et al. (2015) and Frone (2015).

- *Recent Pleistocene-Holocene Newberry Volcanics* (~700 ka to 1.3 ka) – The volcano is a bimodal construct of intermediate to mafic lava flows, cinder cones, silicic lava flows, and domes, tuffs, lahars, and debris flows. Xenoliths and cuttings from wells drilled by CalEnergy and Davenport provide evidence of intrusive rocks related to the Newberry volcanics. The potassium feldspars in the silicic igneous rocks of Newberry Volcano are dominated by albite, with an absence of sanidine. This potentially could be used to distinguish the felsic intrusives of the Newberry Volcano from older felsic units observed in the Deschutes, Mascall, and John Day Formations. The subvolcanic rocks include granodiorite, felsic dikes, and olivine basalt, which, based on drill cuttings, intrude the John Day Formation. Radiometric age dates from across the edifice reveal multiple episodes of volcanic activity. The youngest flows are found in the central caldera, including the Big Obsidian Flow. Carbon-14 ages obtained from an ash-flow tuff beneath the obsidian flow are 1310 ^{14}C yr BP (Jensen 2006). K-Ar dates from rhyolite domes around the edifice range from 400 ka to 700 ka (MacLeod et al. 1981). Rhyolite of Paulina Peak dates to 83.5 ± 5 ka (Jensen et al. 2009). Basalt flows associated with the Northwest Rift zone are ~7 ka based on radiocarbon ages that range from 6610 to 7240 years BP (MacLeod et al. 1995; McKay et al. 2009) and the fact that they overlie the Mazama ash erupted from Mount Mazama (Crater Lake) between 6600 and 6700 ^{14}C years BP (MacLeod et al. 1981).

- *Pliocene-Pleistocene Lavas and Sediments* (~5.3 Ma to 126 ka) – Broad olivine basalt shield volcanoes and volcanic sediments are mapped off of the flanks of Newberry Volcano. Much of the detailed mapping of these rocks has been done to the north and west of the volcano. Pre-Newberry silicic volcanic centers of East Butte, China Hat, and Quartz Mountain are on the periphery of Newberry Volcano.
- *Pliocene Deschutes Formation* (>7 to 4 Ma) – The upper portion is composed of olivine basalt flows, andesite flows, basaltic ash, debris flows, eroded, re-worked basaltic and andesitic volcanic sediments, and debris flows dating from about 6 Ma to 4 Ma (Smith 1986). These are underlain by ash-flow tuffs, ignimbrites, rhyolites and rhyodacites, and black-pumice dacite pyroclastics, dating to about 7.4 Ma (Smith 1986). Pyroclastic and debris units are observed to contain a mix of andesite, scoria, dacite, and pumice fragments, all within a single flow (Smith 1986; Sherrod et al. 2004). Ferns and McClaughry and Ferns (2006) identify Deschutes Formation members that are older than 7 Ma as indicated by their position beneath the 7.05 Ma Rattlesnake ash-flow tuff observed to the northeast of Newberry Volcano.
- *Miocene Mascall (Simtustus) Formation* (16.0 to 14.7 Ma) – The Mascall Formation is composed of white- to light-gray sanidine crystal lithic tuff, tuffaceous sandstone and siltstone, lacustrine sediments, and conglomerates (Ferns and McClaughry 2006; Sherrod et al. 2004). Draus (2002) reports magnetic chronology ages of 14.7 to 16.0 Ma, consistent with reported K-Ar ages of 16.6 ±1.4 Ma for the basal tuff, 16.0 Ma for an interbedded Columbia Basalt flow, and an Ar/Ar age of 15.8 Ma for included tuff beds.
- *Un-Named Basalt Flows* (19 to 16 Ma) – Unnamed basalts account for an indeterminate part the 2-million-year unconformity between the Mascall and John Day Formations. These basalts are likely temporal correlatives of the widespread Steens and Columbia River Basalt Group.
- *Oligocene John Day Formation* (37 to 19 Ma) – The John Day Formation is composed of silicic, intermediate and basaltic volcanic lava flows, rhyolite ash-flow tuff, and dacite to rhyodacite tuffs and alluvial deposits, dated at 19 Ma to 37 Ma (Robinson et al. 1984). The western exposures show welded and cemented tuff, volcaniclastic deposits, rhyolite domes and flows, and basalt to andesitic basalt flows. The rhyolite flows and tuffs are sanidine-normative.
- *Intruded John Day* – Based on deep geothermal exploration wells (Table A.2) subvolcanic intrusions underlie and penetrate the John Day Formation. These are generally poorly characterized due to a lack of exposure but comprise dacite to granodiorite. This zone is often referred to as “highly intruded John Day,” or simply as subvolcanic. All formations contain layers of mafic to silicic lava flows and tuffs along with their feeder pipes and dikes, which have been documented by surface mapping or in drill cuttings (Fitterman et al. 1988).

Table A.2. Elevation at base of formations in various wells and core holes (meters and feet above sea level).

TEMPERATURE CORE HOLE OR WELL	NEWBERRY	DESCHUTES	MASCALL	JOHN DAY	INTRUSIVES
NWG 55-29[a]	650 m (2327 ft)	325 m (1066 ft)	Not present?	-746 m (-2447 ft)	<-1294 m (-4244 ft)
NWG 46-16[1]	650 m (2327 ft)	325 m (1066 ft)	-300 m (-1000 ft)		
GEO N-2	775 m (1453 ft)				
GEO N-5	<744 m (2440 ft)				
Santa Fe NC-01	<603 m (1978 ft)				
CE 76-15 TCH	1015 m (3329 ft)	878 (2880 ft)	<437 (1433 ft)		
CE NB4	<693 m (2273 ft)				
CE 23-22	564 m (1890 ft)	427 m (1400 ft)			-703 to -983 m TD (≤-2305 to 3225 ft TD)
CE 88-21					-753 to -900 m TD (≤-2472 to -2952 ft TD)

(a) Geothermal exploration wells. Bottom of Newberry Formation boundaries from Frone (2015).

TD = total depth

Two cross sections depict structural and stratigraphic relationships across the project (section location in Figure A.7). The two sections, a west-east line (Figure A.8) and a north-south line (Figure A.9) use the grouped units (Table A.2). Individual formation identification is of only marginal interest for our purposes; the composition of the rocks is more important with respect to the tendency to fracture. Debris flows, cemented tuffs, and volcaniclastic sediments typically have a clay matrix, are poorly consolidated as deposited, and undergo plastic deformation when stressed. By altering primary minerals to clay, low-grade metamorphism will also make rocks less brittle. Lava flows, welded tuffs, and intrusive rock tend to be brittle, and will mechanically fail (fracture) when stressed. Rock intruded by magma has the potential to be recrystallized by high heat and become more brittle, and be fractured by the pressure and mechanical movement of the intruding magma. Post-intrusive cooling fractures can occur in both the crystallizing magma and adjacent rock. These characteristics and processes are not formation-specific. Even in the absence of detailed geologic correlations, the combination of brittle rock, regional tectonic strain and faulting, intrusive-related fractures, and high temperatures present an attractive combination for EGS development.

The isotherms shown in the cross sections of Figure A.8 and Figure A.9 were drawn by interpolating the temperatures measured in wells, assuming conductive gradients. Away from the control points at the wells, the isotherms can be considered speculative. Frone (2015) provides a more robust temperature model, which is incorporated in the EarthVision model described in Section A.4.3, and will be incorporated in future cross sections.

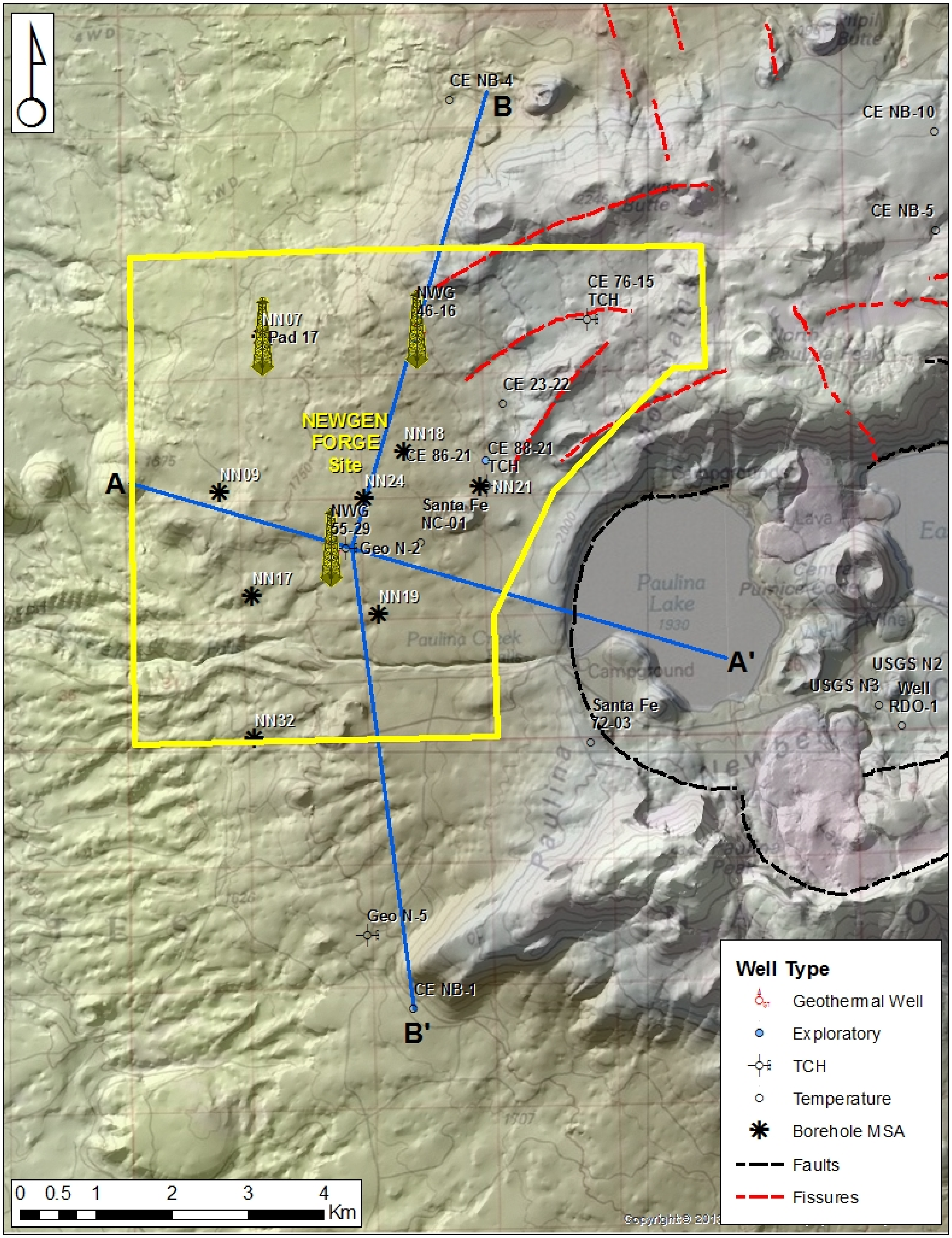

Figure A.7. Location of cross sections and geothermal exploration wells surrounding the NEWGEN FORGE site.

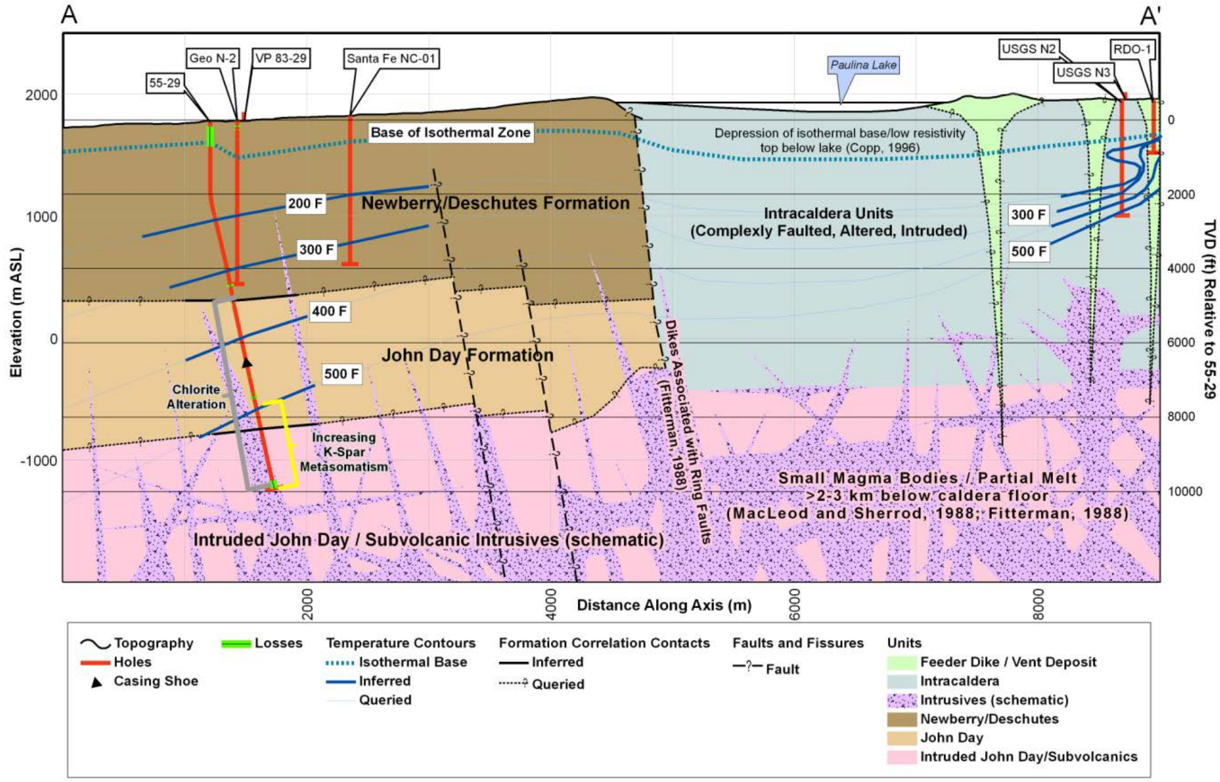

Figure A.8. West-east cross-section A-A' showing formation correlations and speculative isotherms.

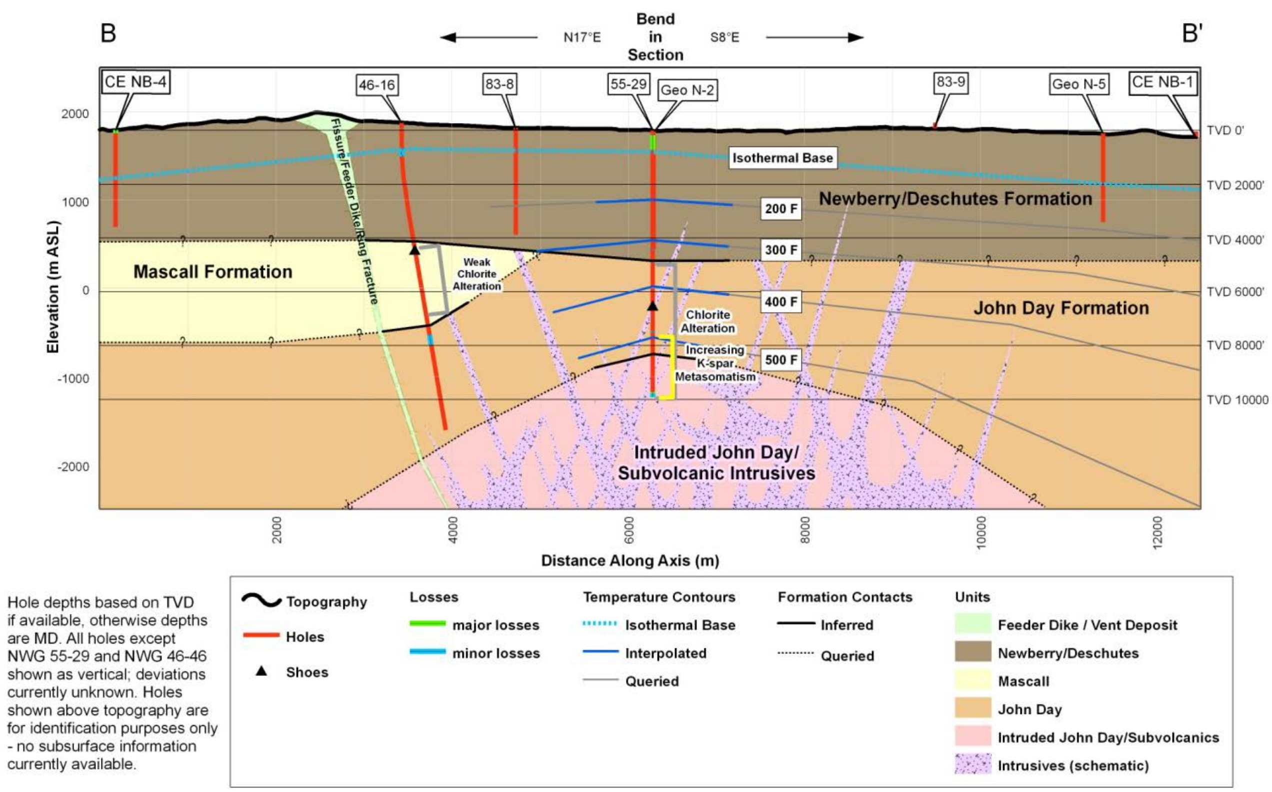

Figure A.9. North-south cross-section B-B' showing formation correlations and speculative isotherms.

A.2.7 Regional Hydrology

The NEWGEN FORGE site is located in the southern edge of the upper Deschutes Basin (Figure A.10). The groundwater hydrology of the upper Deschutes Basin was the subject of a USGS water resources investigation report (Gannett et al. 2001) and an Oregon Department of Geology and Mineral Industries Special Report (Sherrod et al. 2002). The principal source of groundwater recharge for the basin is the crest of the Cascades, including a broad upland area east of the Three Sisters known as the Bend Highland. The average annual rate of recharge from precipitation in the upper Deschutes Basin is roughly 108 m^3/s (3800 cfs) (Gannett et al. 2001). The upper Deschutes Basin extends eastward from the Cascades, and northward from a drainage divide near Chemult that separates it from the Klamath Basin to the south. The eastern margin of the basin lies along the south part of the Ochoco Mountains and through the crest of Newberry Volcano. The northern boundary is near Warm Springs, northwest of Madras, Oregon, (Sherrod et al. 2002).

The upper Deschutes Basin covers an area of approximately 11,655 km^2 (4500 mi^2), and is dominated by a long history of bimodal arc and back-arc volcanism.

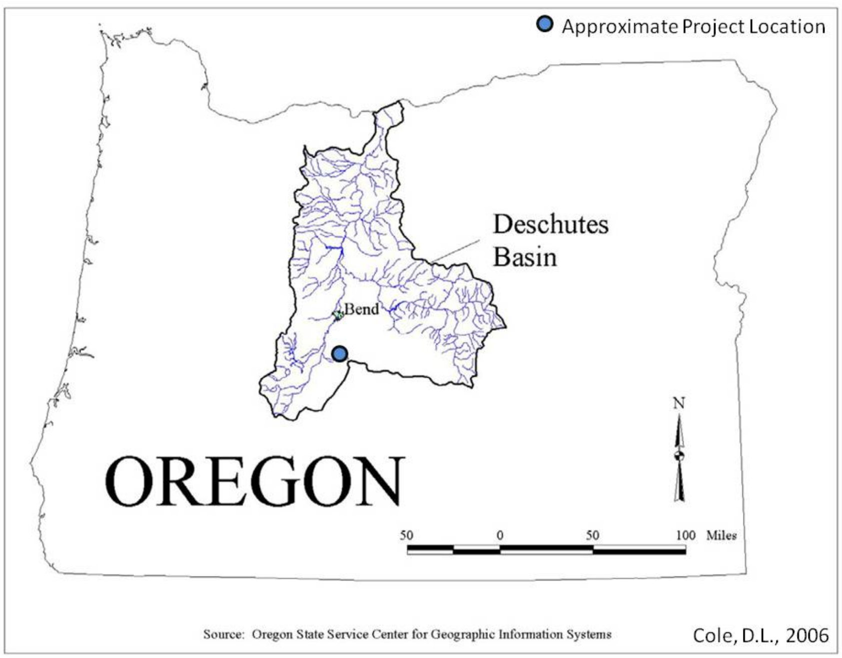

Figure A.10. Deschutes Basin in central Oregon and the NEWGEN project area (from Cole 2006).

Climatic conditions in the area consist of warm, dry summers and cold, wet winters. The Cascades Range, and to a lesser degree Newberry Volcano, contribute to orographic processes in the area. Most precipitation falls in the western side of the basin where annual totals can locally exceed 508 cm (200 in.) per year; this quickly diminishes to the east, with only 25 cm (10 in.) per year falling in the central Deschutes Basin (Gannett et al. 2001). A number of rivers and streams drain the upper Deschutes Basin, with the Deschutes River being the largest. At Newberry Volcano, Paulina Creek is the only drainage feature with year-round flow.

The most prominent surface hydrologic features in the project area (Figure A.7) are East Lake (69,600 acre-feet or 8.5×10^7 m^3), Paulina Lake (249,800 acre-feet or 3.1×10^8 m^3) and Paulina Creek, a net losing stream with a net loss of 0.17 m^3/s (6.1 cfs) for the 13 km (8 mi) stretch of creek from Paulina Lake to U.S. Forest Service Road 21 (Sammel and Craig 1983; Morgan et al. 1997). Both Paulina and

East Lakes are found within the central caldera at Newberry Volcano. East Lake, at an elevation of 1941 m (6368 ft), drains through the subsurface of the central vent complex to the lower Paulina Lake, elevation 1930 m (6332 ft). Paulina Lake is drained by Paulina Creek, which is partially controlled at the outflow of the lake by a small diversion structure to moderate flows for downstream irrigation.

A.2.7.1 Groundwater Hydrology

Sammel and Craig (1983) conducted an assessment of the hydrologic system within Newberry caldera. They estimated groundwater recharge within the caldera to be 3.1 to $8.0 \times 10^6\,m^3$ (2500 to 6500 acre-feet/year), or approximately 19 to 50% of the 79 cm (31 in.) or $1.6 \times 10^7\,m^3$ (13,000 acre-feet) of precipitation that falls within the caldera annually. Bauer and Vaccaro (1987) estimated recharge rates in the project area, based on their deep percolation model, to be 18 to 64 cm/yr (7 to 25 in./yr) (23 to 81% of precipitation). Regardless of the discrepancies between recharge estimates, and potentially between recharge in various years, all researchers would likely agree that infiltration of precipitation is the dominate source of groundwater recharge in the basin.

Regionally, groundwater is hosted in Quaternary alluvial valley fill, and late Cenozoic volcanic and volcaniclastic units with significant primary permeability (e.g., scoria, cinder, etc.) and secondary permeability (e.g., faults and joints). Unconfined to partially confined aquifers are encountered in youngest Newberry Formation deposits on the flanks of Newberry Volcano. Regionally volcanic and sedimentary units of the extensive Deschutes Formation host many prolific aquifers across the entire basin; however below Newberry, the older Newberry and the Deschutes Formation is altered and impermeable below a depth of ~300 m (~1000 ft) as evident from temperature profiles which become conductive below this depth (A.2.10.2 Thermal Measurements and Exploration Wells). The devitrified tuffs and altered sedimentary and volcanic deposits of the older (Oligocene) John Day, Mescall, and Clarno Formations found below the Deschutes Formation form a regional aquiclude (Gannett et al. 2001).

One of the most heavily used aquifers near the NEWGEN project area is the La Pine aquifer. This is a shallow, unconfined aquifer hosted in Quaternary alluvium and interspersed lava flows in the La Pine sub-basin of the Deschutes Valley. The aquifer is underlain by low-permeability clay-rich marsh and lacustrine, low-energy fluvial deposits created when lava flows from Newberry Volcano dammed the ancestral Deschutes River (Sherrod et al. 2002; Morgan et al. 2007). Water table depth in the aquifer varies geographically and temporally, but is often less than 6 m (20 ft), and permeable units extend to only about 100 m (328 ft) (Gannett et al. 2001).

Groundwater on the flanks of Newberry Volcano around the project area is hosted in young volcanic flows and interspersed sedimentary deposits that feature occasional and discontinuous impermeable lithologies. Figure A**.7** shows a plan view of the project area and cross-section lines A-A' and B-B'. Figure A.8 and Figure A.9 show the base of the isothermal zone identified as the bottom of the shallow unconfined aquifer on the flanks of Newberry Volcano. Based on loss zones encountered while drilling, isothermal temperature profiles, and alteration described in mud logs, the shallow, mostly unconfined aquifer intersected by the water wells on Pads 16 and 29 (well numbers DESC 58649 and DESC 58395, respectively) only extends to depths of about 300 m (984 ft) across the project area, with some spatial variability (Dames and Moore 1994). Below this depth is a basal aquiclude formed by increased clay content due to alteration. The top of the aquifer likely fluctuates several meters or more depending on seasonal precipitation, and represents the base of the vadose zone in this area.

Table A.3. Fluid compositions at locations up-, down- and cross-gradient from the NEWGEN FORGE site, and EPA maximum drinking water standards.

Location	Temp (°F)	pH	Cond. (µS/cm)	Alkalinity	As*	B	Ca	Cl	Fe	Li	Mg	Hg* (ng/L)	K	SiO2	Na	Sr	SO4	TDS
East Lake Hot Springs No. 5B (29CDD06)†	146	6.3	814	450	<0.001	1.2	72	1	0.004	0.033	34	<10	8.3	220	54	360	10	654
Paulina Hot Springs No. 2B (26AAB03)†	133	6.4	1145	632	0.012	0.95	55	5	0.01	0.21	45	<10	16	210	130	200	3.6	822
East Lake†	51.4	7.2	330	101	0.002	0.96	25	0.4	0.003	0.011	12	<10	3.8	9.9	24	98	65	212
Paulina Lake†	50.4	8.3	590	342	0.015	0.89	28	2.3	0.01	0.071	38	<10	5.6	43	48	84	3.1	358
Paulina Creek†	54.3	8.8	566	38	0.014	0.002	27	2.4	0.006	0.07	38	<10	5.4	40	46	83	3.2	350
Pad 29 Water Well (3/08)‡	53	7.5	420	255	0.027	n/a	19	3	0.06	n/a	n/a	bdl	n/a	n/a	38	n/a	2.8	256
Pad 29 Water Well (9/10)‡	53	7.8	n/a	230	0.026	0.55	19	3	<0.1	<0.1	24	n/a	5	60	42	0.08	2.5	270
La Pine High School (15AAA)†	48	8.2	106	56	<0.001	0.003	5.2	2	0.057	<0.004	5.2	< 10	1.8	30	9.5	22	1.2	80
Newberry EGS Demonstration average pre-stimulation																		
East Lake Hot Springs	46.8	6.3	0.91	160	0.006	1	35	1.4	0.17	<0.1	17	<0.0001	4.8	37	32	0.11	54	270
Paulina Lake Hot Springs	46.8	6.3	0.917	660	0.014	0.9	56	7.5	<0.05	0.2	48	<0.0001	16.0	220	140	0.2	3.5	820
NN-18	**10.2**	**7.2**	**0.3**	**181**	**0.028**	**0.91**	**10.7**	**6.6**	**0.09**	**<0.1**	**10**	**<0.0002**	**6.95**	**56**	**47**	**<0.05**	**8.95**	**215**
Pad-29 water well	**16.3**	**7.6**	**0.4**	**242**	**0.0314**	**0.568**	**19.2**	**3.56**	**0.085**	<0.1	**25**	<0.0001	**4.78**	**60**	**44.2**	**0.08**	**2.46**	**278**
NN-17	**10.6**	**7.4**	**0.4**	**241**	**0.0105**	**0.555**	**18**	**3.1**	**<0.05**	**<0.1**	**24**	**<0.0002**	**4.1**	**52**	**39.5**	**0.07**	**2**	**265**
Prairie Campground water well	**11.5**	**7.4**	**0.1**	**48.0**	**<0.002**	**<0.05**	**4.3**	**1.7**	**<0.05**	**<0.1**	**3.5**	**<0.0002**	**1.4**	**35.0**	**7.9**	**<0.05**	**1.5**	**70.0**
Newberry EGS Demonstration average post-stimulation																		
East Lake Hot Springs	**31.8**	**7.0**	**43.7**	**238**	<0.002	**0.96**	**42.8**	**1.7**	**0.1**	<0.1	**21**	<0.0001	**5.6**	**67.3**	**37.3**	**0.1**	**45**	**348**
Paulina Lake Hot Springs	**42.8**	**6.6**	**70.6**	**524**	**0.0**	**0.8**	**47.2**	**6.6**	<0.1	**0.19**	**43**	<0.0001	**11.9**	**157.6**	**101.6**	**0.17**	**8.9**	**642**
NN-18	**7.2**	**8.9**	**10.1**	**181**	**0.0**	**0.9**	**9.8**	**6.0**	**0.2**	<0.1	**13**	<0.0001	**6.2**	**69**	**45.7**	<0.05	**4.7**	**243**
Pad-29 water well	**13.7**	**7.3**	**-41.3**	**250**	**0.0**	**0.6**	**19.0**	**3.6**	<0.05	<0.1	**25**	<0.0001	**5.0**	**58**	**44.3**	**0.07**	**2.5**	**280**
NN-17	**7.1**	**8.3**	**-6.9**	**233**	**0.0**	**0.5**	**17.7**	**3.3**	**0.2**	<0.1	**24**	<0.0001	**4.2**	**53**	**38.6**	**0.1**	**1.9**	**251**
Prairie Campground water well	**10.8**	**7.7**	**108**	**44**	**<0.002**	**<0.05**	**4.2**	**1.25**	**0.075**	**<0.1**	**3.55**	**<0.0001**	**1.65**	**36.5**	**8.1**	**<0.05**	**0.5**	**73**
EPA Drinking Water Standards*		6.5-8.5			0.01			250	0.3			2000					250	250

*As and Hg = primary MCLs, all others = secondary MCLs. Oregon regulations are the same as the EPA for As and Hg.

† Morgan, et al., 1997

‡ Data collected by Davenport Power, LLC.

Four boreholes were drilled and one existing well was deepened for seismic monitoring at the NEGSD site in 2012 (Figure A**.7**). The standing water levels recorded after the wells were completed ranged from 171 m (562 ft) below the ground surface at NN18 (surface elevation 6033 ft) to 106 m (350 ft) below the ground surface at NN17 (surface elevation 5580 ft), indicating the top of the aquifer at five locations within the NEWGEN project area. Water-level data are recorded at NN18 and the Pad 16 water well and reported annually to the Oregon Department of Water Resources (ODWR). In addition, ODWR maintains a transducer in NN18 and periodically visits the site to download water-level data.

The NEGSD water monitoring program collected groundwater at seven sampling locations up, down, and cross-gradient from NWG 55-29 prior to, during, and after stimulation activities. Samples were analyzed for a suite of constituents, and these data have been compiled with historical data, which will inform future groundwater monitoring efforts at the NEWGEN project site. A summary of geochemical data from surface and groundwater monitoring sites is provided in Table A.3. Complete reports on the groundwater monitoring efforts of the NEGSD are included in the Phase 2.1 and 2.2 reports (AltaRock 2014, 2015).

Productivity of the aquifer at the NEWGEN FORGE site has been demonstrated on several occasions. During drilling, Wells NN17, NN18, NN19, NN21, and NN24 all produced water at varying rates; Well NN17 was the most productive and reached up to 31 L/s (500 gpm). A drawdown test of the Pad 29 water well carried out in 2011 indicated a specific capacity of 3.3 L/s per meter (16 gpm per foot) of drawdown. Transmissivity and conductivity were estimated, respectively, at 602 m^2/day (6485 ft^2/day) and 49 m/day (162 ft/day) for a 12.2 m (40 ft) thick aquifer. Transmissivity estimates from the drawdown test are 5 to 10 times higher than results from Gannett et al. (2001). However, this is not unexpected given the heterogeneous nature of aquifer lithologies across the basin.

A.2.7.2 Thermal Springs

Thermal features within Newberry caldera, including Paulina Hot Springs (52°C [126°F]) and East Lake Hot Springs (62°C [144°F]), are believed to result from the circulation and steam heating of meteoric water, with no significant contribution of geothermal liquid (Sammel and Craig 1983). Both East and Paulina Lake hot springs were sampled as part of the NEGSD water monitoring plan (Table A.3). Gas seeps are also found in the central part of the caldera, near the younger rhyolite domes. Field observations during winter months indicate gas seeps in a number of places at both East and Paulina Lakes where lake ice is often melted in various areas.

A.2.7.3 Geothermal System in a Low-Permeability Environment

Below ~300 m (~1000 ft) beneath NWG 55-29 and other NEWGEN well pads, increased smectite and green clay alteration forms an impermeable base in the host rock, and at greater depths (approximately 1500 m [4921 ft]) the altered tuffs of the John Day Formation result in extremely low permeability. The results of injection tests for Wells CE 23-22, CE 86-21, and CE 76-15 TCH, and NWG 55-29 all located on the western flank of Newberry Volcano in the vicinity of the NEWGEN FORGE site, reveal injectivity several orders of magnitude lower than the lowest permeability geothermal wells found in other hydrothermal fields (Section 2.3.4 above). Unlike hydrothermal projects, the very low permeability found at depth on the flanks of Newberry Volcano is a desirable feature for EGS advancement, allowing development of a closed hydraulic circuit.

A.2.8 Natural Seismicity

The historical earthquake record can be divided into three periods: pre-instrumental, instrumental prior to 2011, and instrumental after 2011. Prior to ca. 1961, earthquake locations and estimates of magnitude were based on felt reports. Earthquake data were gathered from newspaper accounts, which began with the establishment of settlements in the region. The pre-instrumental record for this region is estimated to be complete above an earthquake M 5 since about 1850 (Wong and Bott 1995). The historical catalog used in this analysis is from Wong et al. (2000), updated with data principally from the Advanced National Seismic Network and the USGS.

A.2.8.1 Pre-Instrumental Seismicity

No earthquakes greater than M 5.0 occurred within 100 km of Newberry Volcano between 1891 and 1961. The closest large event was the M 6.0 Klamath Falls, Oregon, earthquake that occurred on 21 October, 1993, 165 km southwest of Newberry Volcano. However, several moderate-size events have occurred since 1891. They include three Richter-magnitude-scale (M_L) 4.3 events or Modified Mercalli Intensity (MMI) V events in 1906, 1920, and 1921, none of which were felt at Newberry Volcano.

The largest and most significant earthquake in eastern Oregon, known as the Milton-Freewater or Stateline earthquake, occurred at 11:08 p.m. on the night of July 15, 1936 (Neumann 1938). The maximum intensity was MMI VII+, and it was felt over an area of 275,000 km^2. The event was estimated to be a M_L 6.4 (Bott and Wong 1993). The mainshock was preceded by two felt foreshocks at 10:30 p.m. and 11:20 p.m. local time and was followed by numerous aftershocks (Neumann 1938).

A.2.8.2 Instrumental Seismicity in Oregon (pre-2012)

Although the earliest seismograph station in the Pacific Northwest was established in 1906 in Seattle, coverage using modern instrumentation did not begin until 1980 when the University of Washington extended its seismographic coverage into Oregon. Before this time, stations such as Corvallis (COR) installed in 1944 and Klamath Falls (KFO) in 1962 were few in number. Due to the lack of extensive seismographic coverage, the historical record is probably only complete in the study region for events of $M_L \geq 3.0$ since 1980.

There have only been six M_L 3.0 or greater earthquakes within 100 km of the Newberry Volcano since 1980. Of these events, four in 1999 consisted of a minor swarm of earthquakes during April and May. The largest event in the swarm was a M_L 4.3 earthquake on April 28, 1999, which was felt at Christmas Valley and Paisley, Oregon. It was located about 98 km southeast of the Newberry Volcano (Figure A.4). Two other events were felt in Christmas Valley, a M_L 3.1 on 27 April and a M_L 3.3 earthquake the following day. The closest M_L 3.0 and larger earthquake to the site was an event estimated at M_L 3.0 in 1943 about 35 km north of the site. Based on the instrumental record, no earthquakes with M_L >3.0 have been located within 10 km of Well NWG 55-29 or Newberry Volcano.

A.2.8.3 Natural Seismicity (after 2012)

The regional seismic network at Newberry Volcano was greatly improved in 2011 and 2012. In 2009, the only station at Newberry Volcano was NCO, a single-component, short-period seismometer on the east flank and only four microearthquakes (M 1.3–2.2) were detected at Newberry Volcano in the prior 25 years (PNSN 2015). In 2011, the USGS installed six three-component broadband seismometers and one three-component short-period sensor (PNSN 2015). In 2012, four of the borehole stations in the NEGSD microseismic array (MSA) were added to the Pacific Northwest Seismic Network (PNSN) network (see Preliminary Induced Seismicity Mitigation Plan for more information about the NEGSD

MSA). The seismic coverage of Newberry Volcano is now comprehensive, and events as small as M 0.0 can be detected. Since 2012, 74 natural microearthquakes with M 2.3 to 0.0 have been located within 10 km of the NEWGEN FORGE site (Figure A.11).

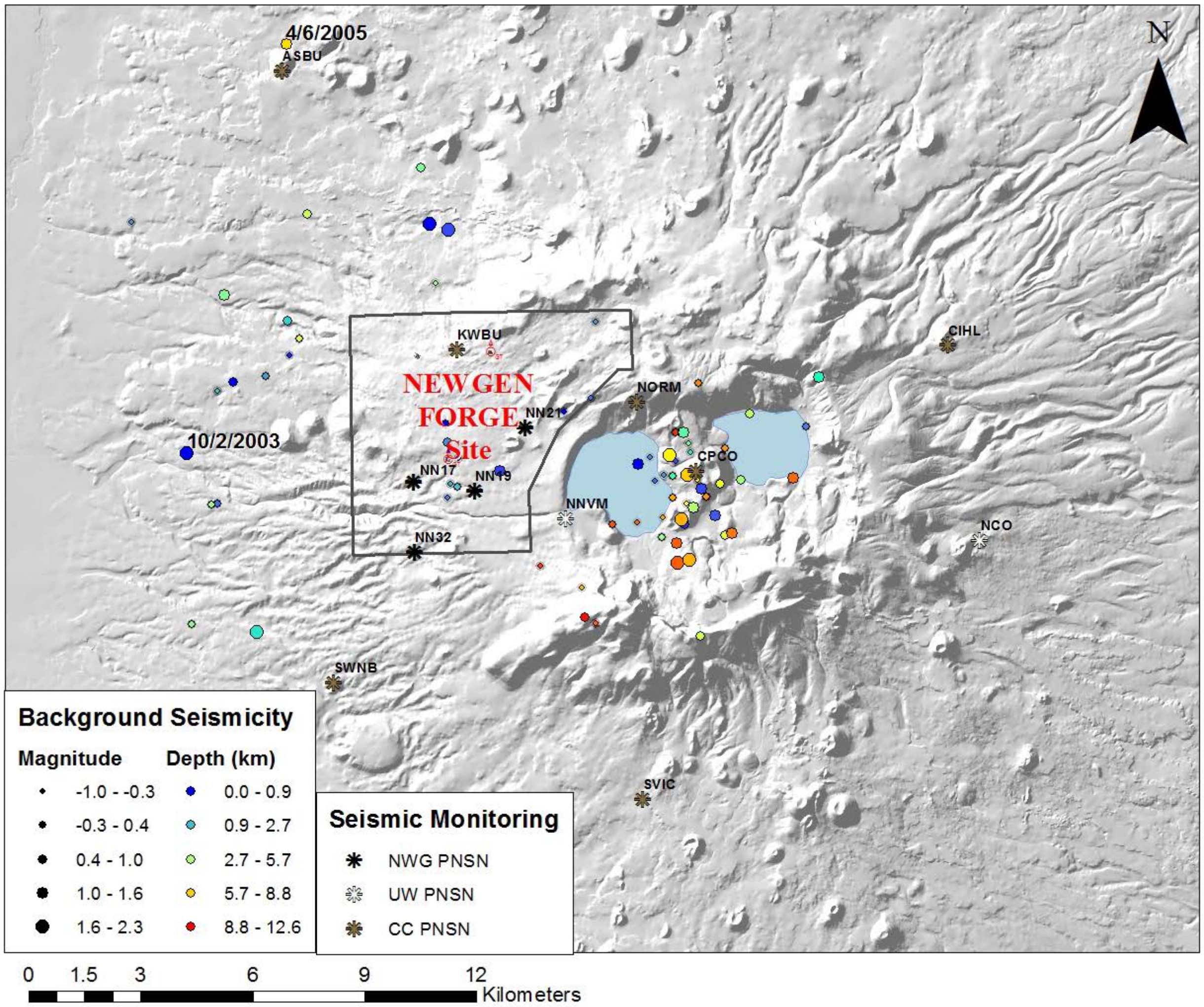

Figure A.11. Background seismicity within 10 km of NEWGEN FORGE site. Only two events were located (labeled with dates) before the network was improved.

A.2.9 Geophysical Studies

A.2.9.1 Geophysical Data Sources

Our understanding of conditions within the proposed NEWGEN FORGE area is aided by more than three decades of focused geophysical observations at Newberry Volcano. Well-ties from core logs and mud logs as well as downhole equilibrium temperature measurements establish known values at depth for several key geophysical parameters and associate these with known lithologies. The geophysical problem is to interpolate between known values separated by relatively short distances within the NEWGEN FORGE site (Figure A.7). This has advantages over situations where there is limited information about known properties at depth, and significantly reduces the uncertainties in the interpretation. The many hundreds of geophysical observations in and immediately surrounding the NEWGEN FORGE site allows for stronger constraints on model parameters and improves the quality of the geophysical interpolation.

The problem of generating estimates of geophysical parameter values such as seismic velocities, electrical resistivities, densities, etc. within the subsurface is intrinsically non-unique. This uncertainty propagates into EGS parameters derived wholly or in part from each of the geophysical results, such as the extent of the target reservoir rock units, the temperature profile, fluid content, permeability and porosity, structure and lithology, petrology, and stress regime.

The power of geophysical methods for geothermal characterization lies not in the use of any one method in isolation, but in the combination and coregistration of multiple methods, each sensitive to its own range of material properties and physical conditions. By overlaying these combined observations, ambiguities in the derived EGS parameters of interest can be greatly reduced. Referencing against, or directly constraining the model inversions to fit observed lithologies and downhole conditions provides the strongest constraint of all. The issue of qualitative, quantitative and/or probabilistic uncertainty analysis that this raises is discussed further in Section A.5.

The primary geophysical data sets and their role in the initial characterization of the NEWGEN FORGE site are discussed below.

A.2.9.2 Seismic Tomography

Beachly et al. (2012) represents the most comprehensive seismic *P-wave* velocity model of Newberry Volcano published to date. This study made use of data from a series of high-resolution explosive source seismic profiles obtained at Newberry Volcano in 1983 and 1984 by the USGS, and by a team from the University of Oregon in 2008. The seismic station locations and explosive source locations are shown in Figure A.12.

The 3D seismic tomographic velocity model (Figure A.13, Figure A.14) shows at shallow depths that a ring-shaped high-velocity anomaly underlies the caldera ring faults that were previously identified by MacLeod et al. (1995). This 7 km by 5 km wide, 1 to 2 km laterally thick ring structure surrounds a central low-velocity zone that extends from 0.5 km to 2 km beneath the caldera. Beneath this, *P-wave* velocities in the ring structure increase, and the structure widens, particularly to the west and east of the caldera. At 3 km depth, the eastern high-velocity anomaly is 1 km/s faster than average, and the western is 0.6 km/s faster. Beneath 3 km, the high velocity widens further, although the extent is poorly resolved.

The tomographic model reveals a heterogeneous seismic velocity structure beneath the volcano. The heterogeneities may not map simply to changes in lithology, but may also reflect variations in porosity and temperature, and also the presence of partial melt at depth beneath the caldera. The low-velocity zone within the caldera is inferred to be porous, caldera-fill deposits in the upper 500 m, and from 500 m to 2 km beneath the caldera low velocities are associated with porous, fractured lava flows that correlate with those identified in drill cores (Beachly et al. 2012).

The high-velocity ring surrounding the caldera is interpreted as an intrusive complex of more competent rock; either ring-dikes or cone-sheets that underlie the surface ring faults. At depths >2 km, high velocities are associated with an intrusive complex built up through successive events. Velocities here are higher than in the ring complex, and this zone is elongated in the east-to-west direction. This may be associated with the east-to-west extensional setting at Newberry Volcano. Mafic magmas may find a path for surface eruption along the Northwest Rift zone that extends from the caldera to the north and northwest, and along an extension of the north-northeast–trending Walker Rim fault system that intersects the caldera from the south (Figure A.3). A line of volcanic vents is distributed along the trace of this fault to the south of the caldera (Figure A.4). These features may facilitate surface eruptions (McKay et al. 2009), whereas intrusions along the east and west flanks of the volcano may not erupt as easily, thus building up a greater volume of intrusive materials at depth.

By using finite-difference waveform modeling, Beachly et al. (2012) show that the tomographic model in Figure A.13 and Figure A.14 matches the observed seismic first-arrival travel times, but it does not produce the secondary seismic phases nor the observed changes in first-arrival amplitudes seen in the seismic data. Low-velocity bodies such as the putative magma chamber beneath the caldera may be difficult to resolve from *P-wave* arrival times because of waveform healing, particularly if they are smaller or deeper than the dominant seismic wavelength. Previous seismic studies (Achauer et al. 1988; Gettings and Griscom 1988), as well as Fitterman's (1988) electromagnetic investigation of the caldera either failed to detect such a body, or produced ambiguous results. While the travel-time tomogram may be insensitive to such a body, secondary seismic phases may be significantly influenced by such zones.

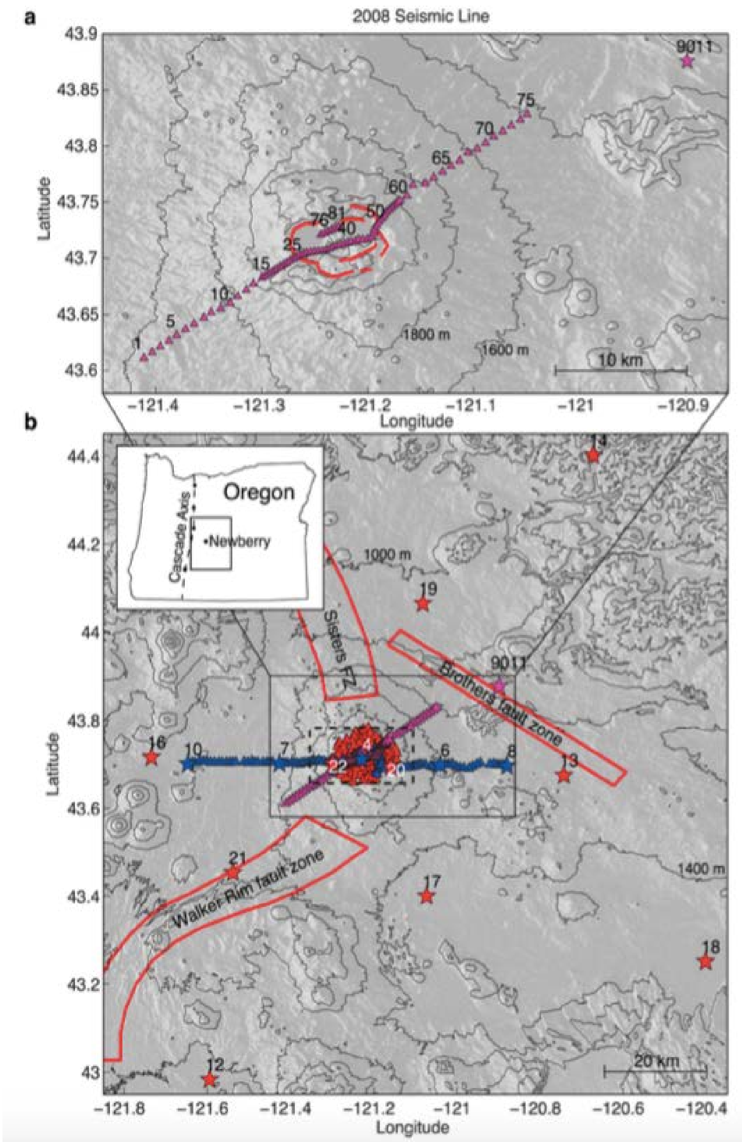

Figure A.12. Seismic tomography experiment.

(a) Map of 2008 seismic experiment showing 40 km long seismic line centered on Newberry caldera. Stations (pink triangles) were spaced every 300 m near the volcano's center and every 800 on the flanks. Shot 9011 (star) of the National Science Foundation EarthScope High Lava Plains Experiment was 30 km NE of the caldera. Caldera ring fractures are marked in red (from MacLeod et al. 1995).

(b) Map of the three seismic data sets used in the tomography inversion for crustal P-wave velocity structure. The USGS data collected in 1983 and 1984 are shown with blue and red symbols, respectively. The explosive sources are shown as numbered stars and the seismic stations as triangles.

(Figure from Beachly et al. 2012)

Beachly et al. (2012) tested the hypothesis that a discrete magma chamber superimposed on the underlying 3D seismic structure would explain the discrepancy between the 3D model and the observed secondary seismic phases and observed amplitude changes. Finite-difference forward modeling of the impact of each proposed body on secondary phases in the seismic wavefield was used to minimize the misfit between the predicted and observed seismic waveforms. Such a body was superimposed on the background tomographic model to examine three possible scenarios: a graded-mush zone, a crystal suspension, and a melt sill above a thin mush zone. 140 different melt zone models were tested covering a range of geometries for each of these scenarios. Their results show that finite-difference waveform modeling constrains the geometry, velocity and partial melt fraction of the low-velocity region.

The seismically derived interpretation of Newberry's structure, aggregating both tomographic and waveform modeling results, is shown in Figure A.15. The waveform data fits all of three preferred models shown in Table A.4.

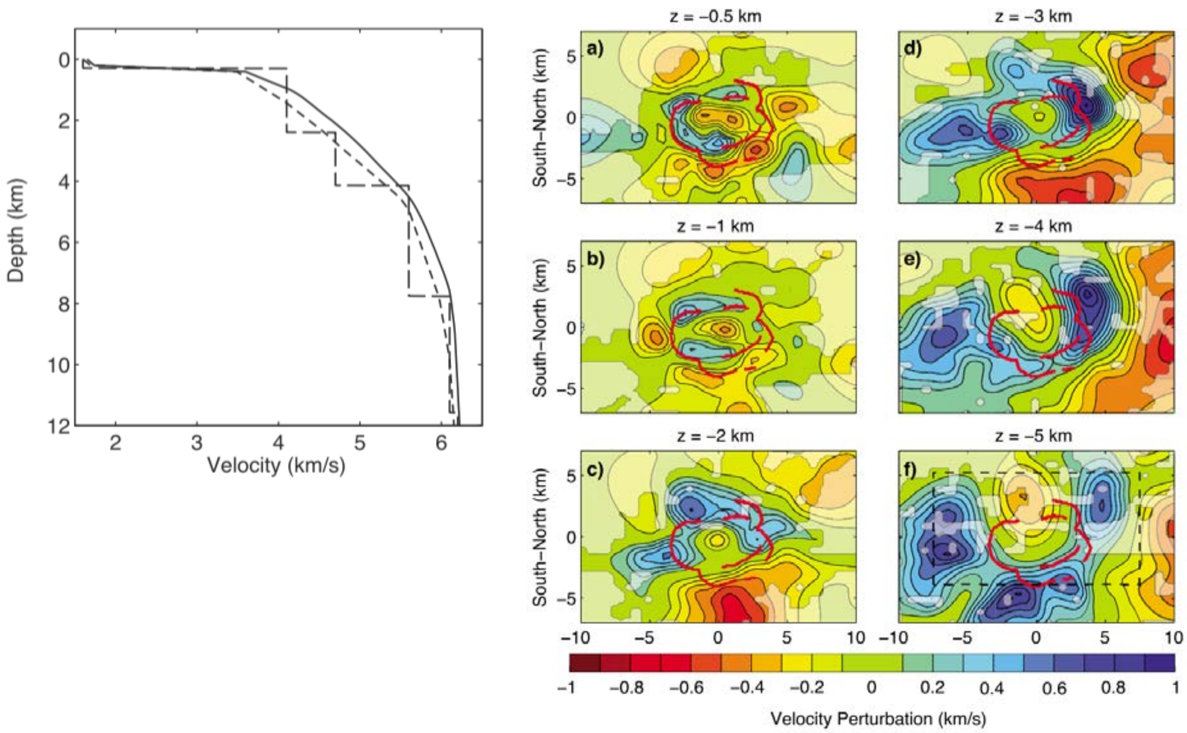

Figure A.13. (Left) Underlying one-dimensional (1D) P-wave velocity model used in tomogram (continuous black line). (Right) 3D P-wave velocity as a perturbation on the 1D model shown with 0.1 km/s contours. Red areas represent those with slower P-wave velocities than the 1D model at that depth, and blue are areas of faster velocities. Lighter shaded areas of the model are poorly resolved. Red lines show caldera ring faults mapped at the surface (MacLeod et al. 1995). (a)-(d) represent map views at depths of 0.5 km, 1 km, 2 km, 3 km, 4 km, and 5 km, respectively. (Figure from Beachly et al. 2012.)

While the zone of partial melt is separated from the NEWGEN area by a thick section of impermeable rock, efforts to characterize the seismic structure at higher resolution within the FORGE site during the proposed Phase 2 of this project will need to take the existence of this body into account for seismic ray paths that impinge on this zone. Additionally, the presence of partial melt beneath Newberry Volcano provides an enormous store of heat; the three preferred models predict a range of melt volumes between 1.6 and 8.0 km^3 (Beachly et al. 2012). Frone et al. (2014) estimate that there is 6.1 EJ (exajoules) [10^{18} joules]) of heat contained within the upper 3.5 km beneath the caldera, and 174.4 EJ beneath the entire volcanic edifice, to that same depth. This contrasts with the ~100 EJ total U.S. energy use budget in 2012.

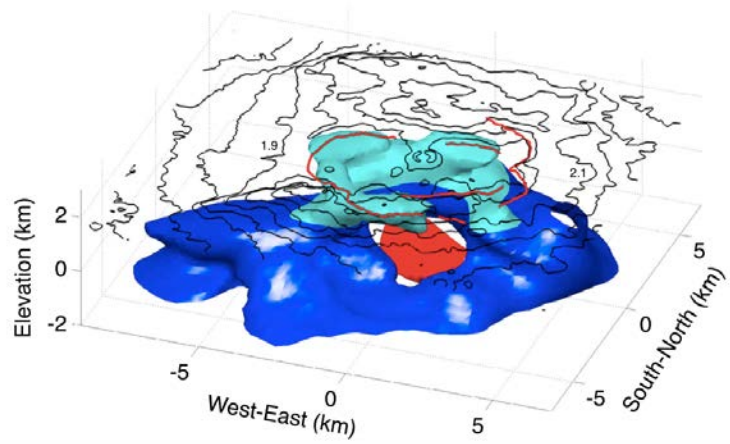

Figure A.14. 3D seismic travel-time tomographic model of P-wave velocity beneath Newberry Volcano. High-velocity structure is light blue above 1.5 km depth and dark blue beneath that. The high-velocity isosurfaces represent intervals of +0.2 km/s velocity above a background 1D structure. The difference in shade of blue illustrates a possible structural difference between a shallow high-velocity ring structure associated with the caldera rim, and a broader, deeper high-velocity region. A central low-velocity region appears in red, shown as a -0.1 km/s velocity perturbation isosurface from the 3 to 5 km depth. A shallow low-velocity anomaly within the caldera is not shown. Red lines at the surface are inferred ring fractures; black lines show 0.1 km topographic contours. (From Beachly et al. 2012.)

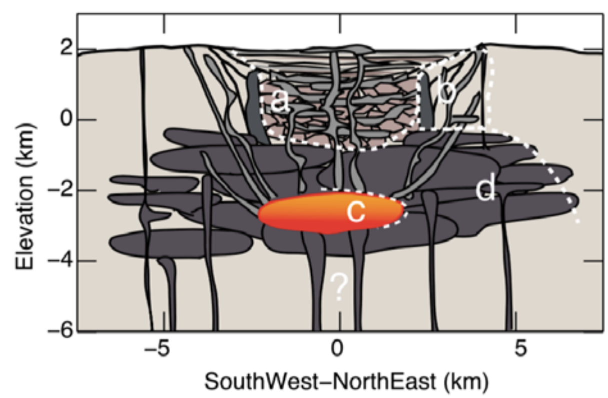

Figure A.15. Tomographic and seismic waveform modeling interpretation of geologic structure beneath Newberry Volcano on a SW-to-NW profile. Region (a) is caldera fill consisting of layers of tephra, porous lavas, and rhyolite domes in upper 1 km, and collapsed pre-caldera rocks in the lower 1 to 3 km. Silicic dikes and sills likely intrude this region. Region (b) is an intrusive-ring complex surrounding the caldera fill. This may consist of ring-dikes formed during caldera collapse, dikes intruded into ring faults during uplift and/or later dikes that feed eruptions on the caldera rim. Region (c) is the magma body, here shown as a molten sill with a thin mush region on the bottom. Region (d) is a deeper intrusive complex composed of stalled dikes, sills, and remnant magma chamber plutons. (Source: Beachly et al. 2012.)

Table A.4. Physical properties and geometries of the three preferred magma body models.

MODEL	PARTIAL MELT	V_p	V_s	ρ	Q_p	Q_s
Mush zone						
(top) elev. = -1 km	26 ± 6%	-40%, 3.2 km/s	-75%, 0.9 km/s	2.4 g/cm^3	8	3
(bottom) elev. = -4 km	11 ± 4%	-15%, 4.9 km/s	-20%, 2.6 km/s	2.6 g/cm^3	8	0.9
Crystal suspension						
(top) elev. = -2 km	33 ± 8%	-55%, 2.4 km/s	0 km/s	2.4 g/cm^3	8	10,000
(bottom) elev. = -4 km	33 ± 8%	-55%, 2.7 km/s	0 km/s	2.5 g/cm^3	8	10,000
Melt sill						
(melt) elev. = -2.3–2.9 km	100%	2.3 km/s	0 km/s	2.0 g/cm^3	20	10,000
(mush) elev. = -2.9–3 km	26 ± 6%	-40%, 3.4 km/s	-75%	2.5 g/cm^3	8	10,000

Another tomography study (Matzell et al. 2014) used ambient seismic noise and microseismicity from the 2012 stimulation recorded on the NEGSD MSA and a network of broadband sensors that ran from November 2011 to October 2012. Ambient noise correlation and seismic interferometry provided hundreds of unique paths sampling the region around NWG 55-29. High-quality Green's functions were resolved with only a few weeks of data. The best 1D velocity models along each path were inverted to create a 3D shear wave velocity model (Figure A.16). Synthetic seismograms calculated through the 3D model captured the complexity of the direct and scattered waves that were observed in 2012 microseismic data. These techniques allowed resolution of sharp variations in both P and S velocity to be resolved throughout the zone of microseismicity (Figure A.16). A precise 3D velocity model will allow better precision for microseismic event locations to better monitor the growth of the EGS fracture network.

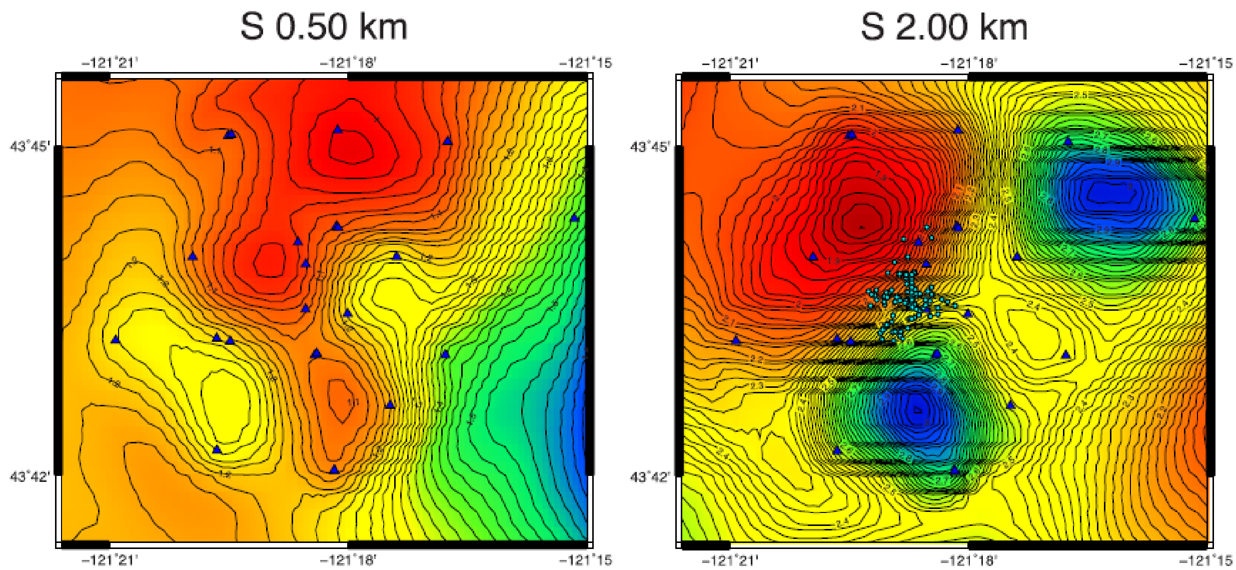

Figure A.16. Slices through the shear velocity model at 0.5 and 2.0 km depth, including the independently located seismicity (cyan circles). Continuous data from Newberry network stations (blue triangles) and nearby seismic networks (off map) were used to constrain the velocity structure beneath the site down to 5 km. The area shown here, the west flank of the volcano, is approximately a quarter of the area shown in Figure A.13, which was centered on the caldera.

A.2.9.3 3D Geophysical Model Based on Magnetotellurics, Direct Current Resistivity, and Transient Electromagnetic Methods

Magnetotelluric (MT) and related electrical methods are used to constrain the electrical resistivity structure of the subsurface. While bulk resistivity of dry rock is sensitive to temperature and composition, electrolyte carrying aqueous fluids or melt along cracks, fissures, and interconnected grain boundaries can decrease the bulk resistivity by orders of magnitude. The resistivity of fluid-saturated rocks continues to decrease with increasing temperature, up to about 250ºC (Parkhomenko 1967; Olhoeft 1981). The chemical composition of interstitial fluids, and mineralization and alteration processes leading to deposition of secondary calcite, clays, zeolite and devitrification of volcanic glass can also impact bulk resistivity (Waibel et al. 2015).

Fitterman et al. (1998) interpreted MT, transient electromagnetic, and Schlumberger DC resistivity soundings at Newberry Volcano using 1D modeling methods. Fitterman's study made use of 35 widely distributed MT soundings taken by Stanley (1982) at Newberry Volcano, concentrated on the west flank. The MT method is most sensitive to the presence of electrically conductive zones, and to the effects of 3D heterogeneities (a limitation early MT researchers viewed as a complication to 1D or two-dimensional (2D) interpretation but that has been used to good effect in modern 3D surveys). These data had a narrow frequency band (0.01 to 10 Hz), which limited the information available about near-surface resistivity structure. This information was provided by transient electromagnetic soundings inside and outside of the caldera (Fitterman 1988; Fitterman and Neev 1985; Fitterman et al. 1988) that constrained shallower conductive zones, but provided limited information on shallower resistive ones. Schlumberger DC resistivity soundings (Bisdorf 1983, 1985) provided reliable resistivity information for these shallow regions. While largely superceded by later studies that substantially increased the number and quality of MT stations and that applied 2D and 3D interpretation methods, Fitterman's combination of three complementary data sets provides constraints that are factored into the Conceptual Geologic Model; in particular the depth of a conductive horizon based on the transient electromagnetic data that is inferred by Waibel et al. (2015) to represent the 150ºC isotherm that corresponds to a zone of progressive smectite alteration, and an electrical basement based on the MT analysis, which is inferred to represent a zone of increased chlorite and potentially epidote (Fitterman et al. 1988).

Waibel et al. (2015) summarize geophysical work undertaken at Newberry Volcano by Davenport Newberry ("Davenport"). Davenport contracted with Geosystems to carry out a 3D MT survey on the west flank of the volcano in 2006, and in 2011 they contracted with Zonge International to extend the aperture of the MT survey to include the south flank and some fill-in on the west flank, as well as an extension to the northwest of the volcano. Zonge carried out transient electromagnetic measurements at each station to assist with correcting their subsequent 2D inversions for complications due to shallow 3D structure ("static shift"). Figure A.17 contains a map of the MT station locations used in the Waibel et al. study.

The result of 2D inversion of the Davenport MT data sets is shown in Figure A.18, which is a vertical section from west-to-east along profile 05 of Figure A.17. This profile runs from the west flank eastward past NWG 55-29, into the caldera and ending at the east caldera rim. The projection of Wells NWG 55-29 and Santa Fe NC-01 and of nearby MT stations onto this profile is marked in the figure. Note that a markedly different resistivity structure is found along the same profile from the 3D inversion by the OSU group and is discussed below (Figure A.20). When interpreting this 2D analysis, one must be cognizant that this data set is demonstrably 3D, so 2D interpretation must proceed with caution.

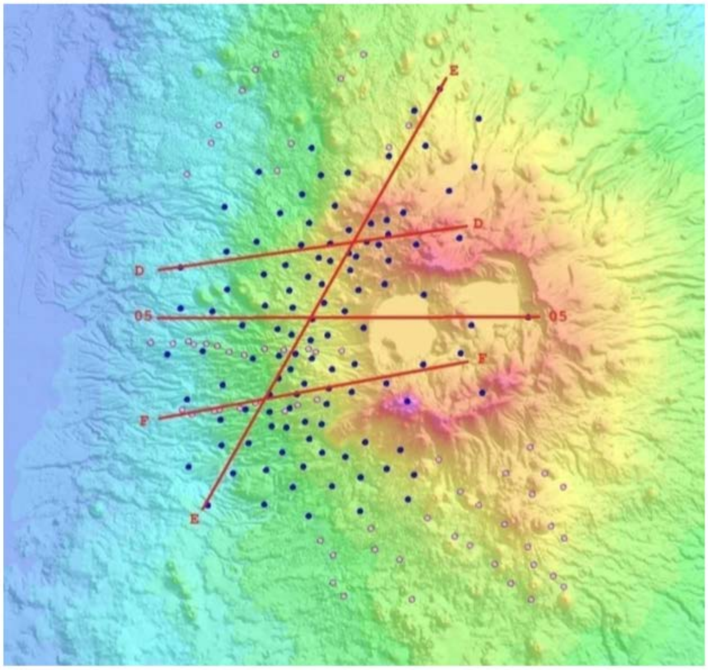

Figure A.17. Location of MT stations cited by Waibel et al. (2015). 2006 Geosystems MT stations are marked with blue dots; 2011 Zonge International MT stations are marked with open red circles. The red lines identify resistivity section profiles (05, D, E, and F) discussed by Waibel et al. (Source: Waibel et al. 2015.)

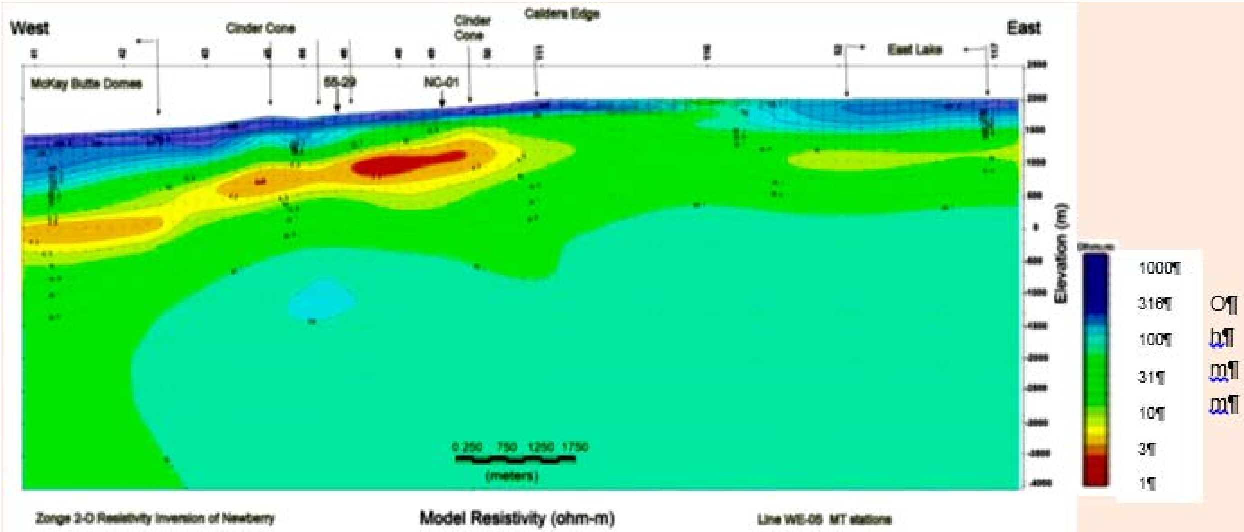

Figure A.18. West-to-east cross section from 2D MT model of Waibel et al. (2015). Dark blue areas are electrically resistive, and dark red areas are conductive; bright green areas have intermediate resistivity values in the 5 to 100 Ω·m range. The vertical scale of the model extends from -4000 m to 2000 m above sea level (the y-axis tic-mark interval is 500 m).

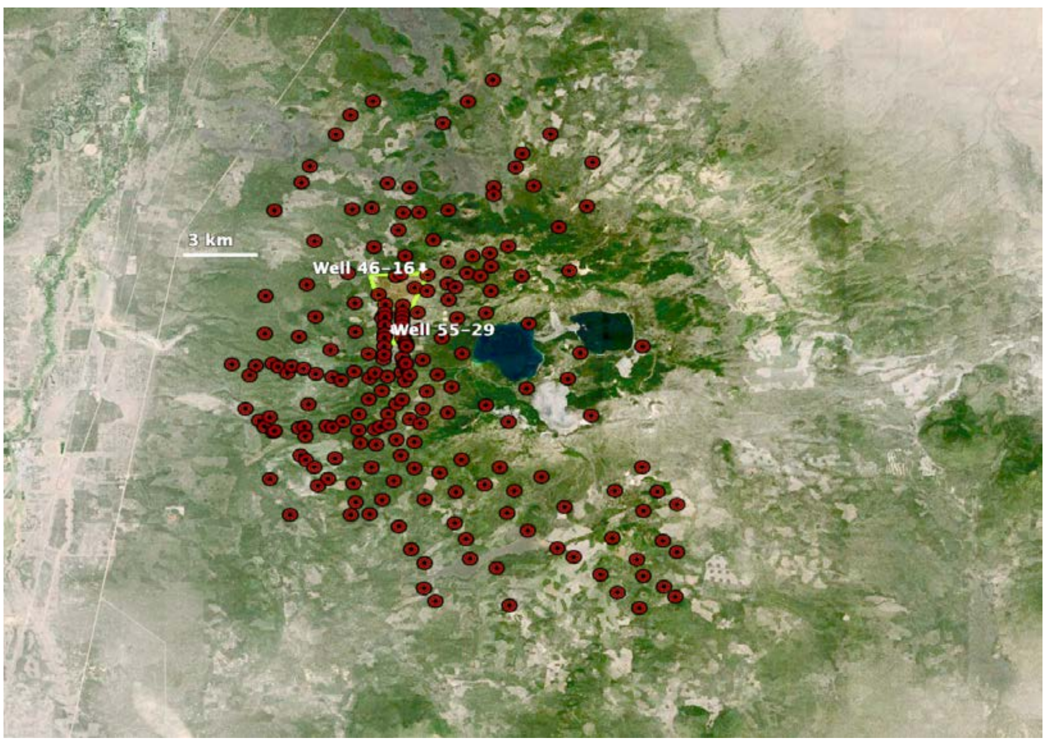

Figure A.19. Locations of Davenport MT stations from 2006 (Geosystems), 2011 (Zonge), and from NETL/OSU/Zonge in 2012 and 2014. The location of the NEWGEN FORGE site is marked as a green triangle, with Wells NWG 55-29 and NWG 46-16 identified as two of the triangle vertices. Not all of the stations collected during these surveys are shown here; some require additional processing and will be used in subsequent analyses. A distance of 8 km separates the cinder cone between the two lakes in the center of the caldera from NWG 55-29 at the bottom apex of the NEWGEN FORGE site.

In this 2D interpretation, the west flank of the volcano (left half of Figure A.18) contains two elongated conductive zones whose top surfaces are ~500 to 1000 m below local ground level (shallowest near Well NC-01). The base of these shallow conductive zones coincides with the 150ºC isotherm as measured in the wells, which is interpreted by Waibel et al. (2015) as most likely due to low-temperature devitrification of volcanic glass shards, diagentic alteration of volcanic and volcaniclastic rocks, and low-temperature thermal alteration. There is no evidence from well cores, well logs or mud logs of current or past hydrothermal circulation in the NEWGEN project area. Waibel et al. (2015) suggest that the concentration of low resistivity in these features may result from localized increases in volcaniclastic content, which facilitates clay alteration.

Other 2D profiles from Waibel et al.'s study (not shown here) reveal a vertical offset within the shallow conductive layer, close to NWG 46-16. As seen below in our own 3D analysis of the combined MT data set, this feature is confirmed (see Figure A.21), and it also overlies a sharp transition at greater depth in a 3D gravity model reported in Section A.2.9.4 3. In contrast to earlier 3D MT interpretations reported by Waibel et al., which they reported provided a lower resolution view of conductivity structure than the 2D interpretations (presumably because of the far greater memory and computational demands of 3D inversion, which restricted the number of cells used in the model), the ongoing OSU 3D study uses a cell size comparable to previous 2D studies, and also benefits from a higher density of MT data within the NEWGEN FORGE area than had been available to the previous 2D and 3D work reported by Waibel et al. (2015).

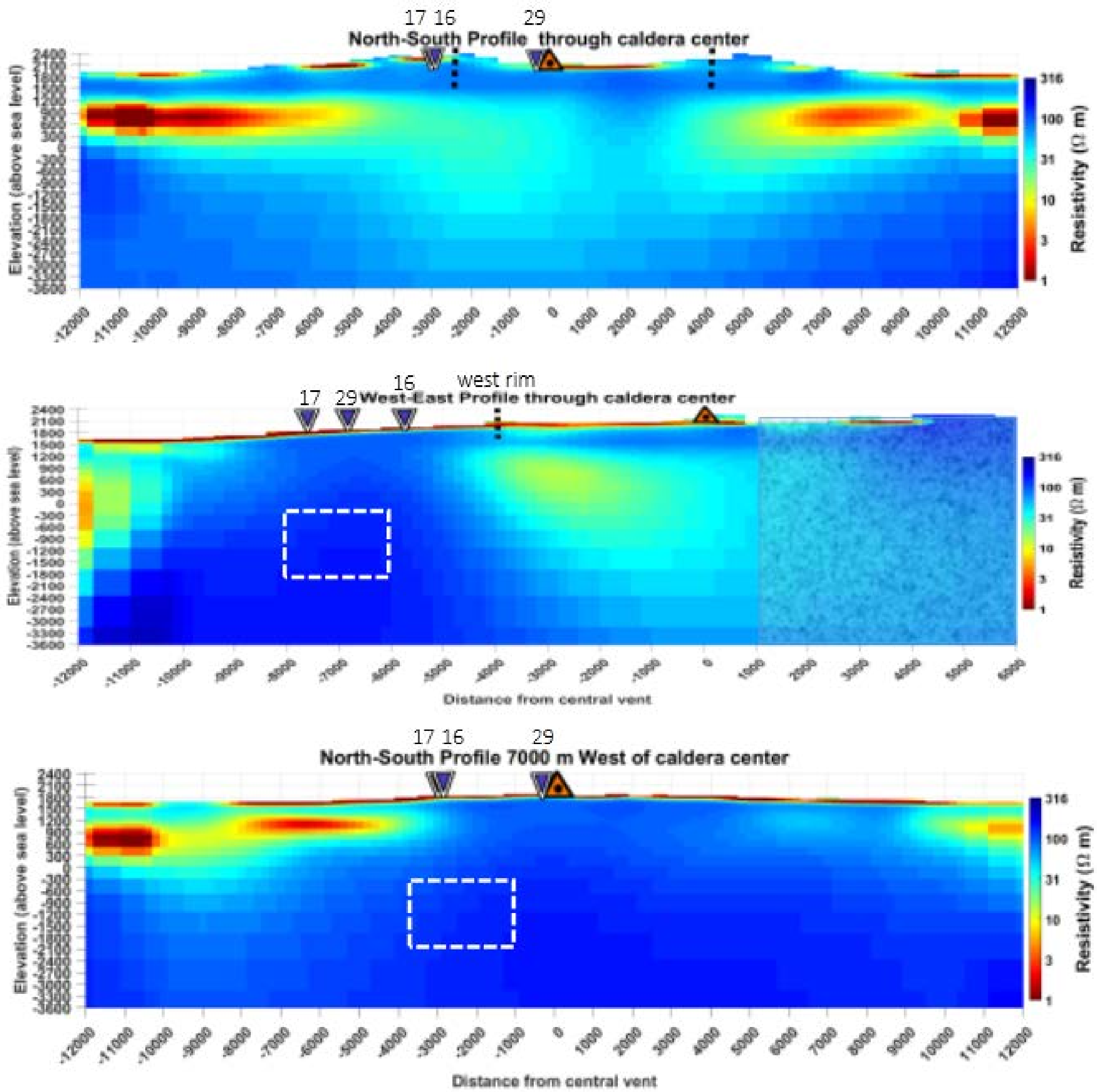

Figure A.20. OSU 3D resistivity model beneath Newberry Volcano. The elevation ranges from 2.4 km above to 3.6 km below sea level.

Additional wideband MT data were collected in and surrounding the NEWGEN FORGE site by OSU and by Zonge International in 2012 and 2014 as part of a DOE-supported NETL/OSU/Zonge project to develop innovative 4D methods combining MT, controlled source electromagnetics, microgravity, and ground deformation to monitor fluids injected during the NEGSD project. A 3D baseline resistivity model has been developed using that MT data set in combination with the 2006 Geosystems and 2011 Zonge MT data. A map of the combined data set station locations is shown in Figure A.19.

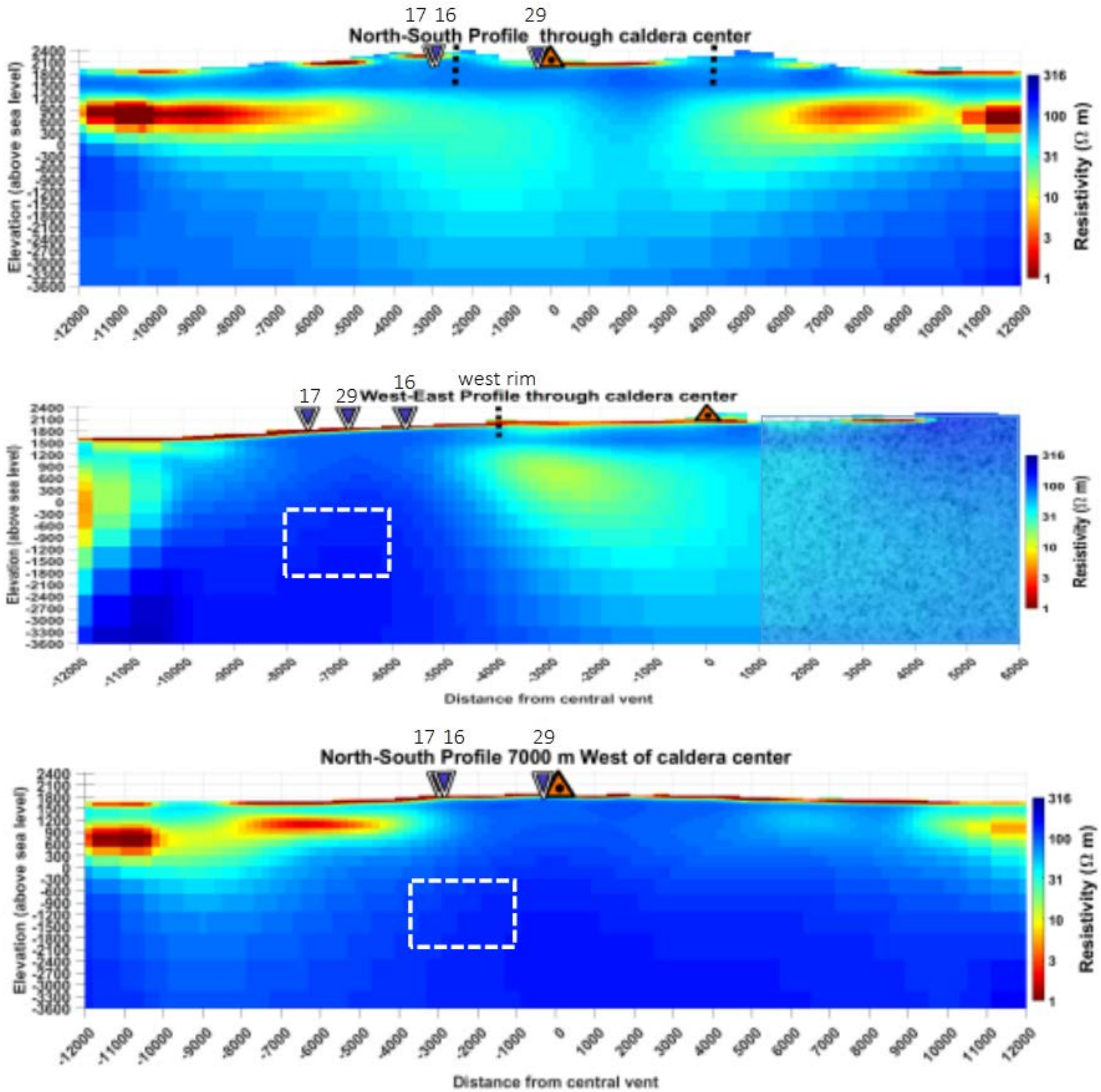

Figure A.21. Map views of OSU 3D MT resistivity model from combined MT data set (log scale: dark red = 100 (1) Ω·m, dark blue ≥ $10^{2.5}$ (316) Ω·m). The white area in the 0 m depth section indicates where the ground surface is at a lower altitude than well Pad 29. The three purple squares are the well pad locations that mark the vertices of the triangular NEWGEN area (well Pad 29 to the south, 16 to the northeast, 17 to the northwest). The black arc is the western rim of the caldera and the orange triangle in the center marks the cinder cone in the center of the caldera.

The station location map shows a high density of MT stations on the west flank of the volcano, with good coverage within the NEWGEN FORGE site particularly along its southeast and southwest margins. Future station in-fill within the core of the site and around its northern perimeter is proposed for Phase 2 of the NEWGEN FORGE project to further improve resolution of fine-scale resistivity variations, but the present data are well suited to constraining the bulk resistivity on lateral scales of several hundred meters, particularly in the upper 1500 m of the site. The 3D MT inverse modeling code *ModEM* (Kelbert et al. 2014; Meqbel et al. 2014) was used to generate the model shown in Figure A.20 and Figure A.21. The topography of the volcano was taken into account, and the model was gridded with cells approximately 200 m on a side horizontally. Vertical cell size depends on depth. While 3D inversion and interpretation of this data set using DOE supercomputer facilities continues (updated to include higher-resolution, reprocessed MT data allowing for cell sizes of 50 m horizontally), the model presented here presents a good overview of the broad-scale resistivity structure within and surrounding the NEWGEN FORGE site.

Figure A.20 shows (top) the north-to-south cross section through the 3D model centered on the cinder cone in middle of the caldera (marked with triangle). (Middle) West-to-East cross section also centered on the cinder cone in the middle of caldera. The eastern third of the section is overprinted with stippling to indicate poor resolving power in that area. (Bottom) north-to-south cross section 7 km west of the cinder cone; centered on the NEWGEN FORGE site on the western flank. Resistivity shown on a log scale, with red representing conductive and blue resistive zones (dark red = 10^0 (1) Ω·m, dark blue ≥$10^{2.5}$ (316) Ω·m. The dashed white box is the projection onto the profile of the boundaries of the NEWGEN EGS zone. The three well pad locations are marked with gold arrows. A vertical dotted black line marks the crater rims.

The top panel of Figure A.20 shows a north-to-south cross section through the OSU 3D model at depths from -3.6 k to 2.4 km above sea level. There is a very thin surface conductive layer beneath which resistivities of 30 to 90 Ω·m prevail to about 500 m below ground level (which agrees with Waibel et al.'s findings), below which are localized zones of low resistivity. The thickest of these, at about 20 Ω·m, extends beneath the northern and southern parts of the caldera to ~2000 m below the caldera floor, which also agrees broadly with Waibel et al.'s (2015) 2D results as well as Beachly et al.'s (2012) Region "a" (Figure A.15) of caldera fill of layers of tephra, porous lavas, and rhyolite domes in the upper 1 km of the caldera, and collapsed pre-caldera rocks in the lower 1 to 3 km, potentially including silicic dikes and sills. The south flank of the volcano has a ~1 km thick highly conductive zone at 0 to 1200 m above sea level. This is closely mirrored on the north flank.

The central panel of Figure A.20 is a west-to-east cross section showing the locations of Pads 16, 17, and 29, the west rim of the caldera and the caldera's central cinder cone. Caution is urged in interpreting the resistivity for the eastern half of the volcano, because MT data in that area are sparse or nonexistent; the eastern third of this cross section is overprinted with stipples to emphasize this point. The western half of the volcano, and particularly the western flank, has dense MT data coverage and may be viewed with greater confidence.

The dashed white box in this panel is the projection onto the profile of the boundaries as defined by the FORGE temperature range requirement of 175ºC to 225ºC, which are found here at depths of 1500 m to 2000 m below Pad 29. It is notable that the NEWGEN zone is centered in a resistive region (~200 Ω·m), which, at this scale, appears to be electrically homogeneous near its southernmost end (the plane of this profile). A conductive (~10 to 20 Ω·m) inward-dipping zone is found ~400 beneath the west rim of the caldera (its absence under the east rim may be a consequence of a lack of MT data there). This appears to align with the high-velocity seismic ring surrounding the caldera identified in the 3D *P-wave* tomogram described previously (Figure A.12), interpreted by Beachly et al. (2012) as an intrusive complex of competent rock; either ring-dikes or cone-sheets underlying the surface ring faults. These structures may have served as channels for fluid circulation and alteration of the diorites that have been mapped at the surface. Such alteration products may serve as conductive pathways.

This profile differs from Waibel's 2D inversion along the same line, as seen previously in Figure A.18, most notably in the absence of the 2D model's elongated conductive body that underlies much of the west flank starting at depths of 500 to 1000 m. Waibel et al. (2015) interpreted the transition from this conductive zone to a resistive zone below (corresponding to the 150ºC isotherm) as an indication of low-temperature thermal alteration, whereas the overlying more conductive zone was interpreted to be due to clay alteration. In the 3D inversion of the combined MT data set, while there is a thin conductive surface layer, the region bounded by Pads 17, 29, and 16 is relatively resistive and more homogeneous at depth than in the 2D profile. The prominent conductive zone bounded to the west by NWG 55-29 and to the east by NC-01 in the 2D model has migrated eastward somewhat in the 3D model, where it is seen to underlie the western crater rim in approximate alignment with the seismic tomographic anomaly (Beachly et al. 2012) that is collocated with the caldera ring structure. In part, differences between previous 2D and current 3D models may be due to the higher density of MT stations used in the OSU 3D inversion than had been available to Waibel et al. (2015). In addition, profiles through the OSU 3D model taken parallel to but 4 km to 7 km north of this profile, show features remarkably similar to Waibel's profile. In addition to differences between the 2D and 3D inversions that might result from improved MT station coverage for the 3D interpretation, the projection of these conductive regions immediately north of this profile may be influencing the 2D inversion. This is currently being investigated.

The bottom panel of Figure A.20 is also a north-to-south cross section (like the top panel), but it is offset from the center of the volcano 7 km to the west. It therefore crosses south-to-north through the center of the NEWGEN area on the west flank of the volcano. As in the previous panel, the dashed white box is the projection onto this profile of the boundaries of the NEWGEN EGS zone. The north-to-south section through the NEWGEN area is resistive, as is the east-to-west section. The presence of large-scale hydrothermal circulation, or remnant alteration products from water-rock reactions would be evidenced as low resistivity features of order 10 $\Omega \cdot m$ or less, which are not evident at this resolution scale.

Figure A.21 shows a series of map views of the OSU 3D resistivity model starting at the surface of well Pad 29, and extending to 4000 m below the pad, in depth intervals of 500 m. As in the Figure A.20, the eastern portion of these sections is stippled to indicate poor resolving power there due to sparse or nonexistent MT data coverage. The shallow conductive feature to the north-northwest of the caldera rim is evident in the 500 m and more prominently in the 1000 m depth sections. A conductive feature is seen to the south-southwest of the crater rim, becoming barely evident at 500 m depth, but growing in amplitude at 1000 m, and continuing until at least 2000 m depth. Lower resistivities persist at greater depth beneath the caldera than elsewhere (see previous comments about tomographic region "A"), although this high conductance masks deeper features beneath the caldera below ~2500 to 3000 m depth, at least for the current data set and inversion.

Figure A.21 reveals that at the resolution scale of several hundred meters, the NEWGEN FORGE site lies within a relatively homogeneous resistive volume. At depths of 500 m and shallower, Pads 17 and 16 lie at or just beyond the northern boundary of the homogenous resistive zone, and Pad 29 lies within it; at 1500 m depth and greater, all three pads are contained within the homogeneous resistive zone. Within the 3D resistivity model, the homogenous resistive zone extends at least to the depth of the specified FORGE EGS temperature maximum, which here is at ~2500 m depth. The NEWGEN FORGE site is bounded to its northeast by the conductive zone that extends from the northwest of the caldera rim, as well as to a second conductive zone to the northwest (at least to depths of 1500 m). The deeper resistive zones at 2000 m and below corresponds to the top of a deeper intrusive complex of stalled dikes, sills and remnant magma chamber plutons posited by Beachly et al. (2012) (Figure A.15).

A comparison between the 3D resistivity depth sections in Figure A.21 and the 3D density sections from the gravity inversion in the Section A.2.9.4 shows a transition in both resistivity and density immediately at or to the northeast of NWG 46-16 and north and west of Pad 17. It is notable that the gravity inversion was constrained by well lithology, but it was independent of the MT inversion. A synthesis of these data sets is discussed further in Section A.4.3.

A.2.9.4 3D Geophysical Model Based on Gravity

NEWGEN FORGE site characterization employs several types of geophysical data to get a better image and understanding of the subsurface geology. Gravity surveys have been conducted on the west flank of Newberry Volcano site as part of previous efforts. The various data sets were combined and processed together to provide meaningful constraints on geologic structures important to determining the suitability of the proposed site.

Gravity Surveys

Three gravity surveys were completed from 2006 to 2010 by Zonge International. In addition to the Zonge surveys, publicly available gravity data (Roberts et al. 2008) for the vicinity of Newberry Volcano were included in the overall data set. A total of 1418 gravity measurement locations were recorded for this analysis. A brief description of the surveys and preliminary data processing is presented here; more details can be found in previous reports (Zonge 2007, 2010, and 2012). The instrumentation used consists of a LaCoste and Romberg model G gravimeter and Leica Geosystems survey-grade Global Positioning System (GPS)/Global Navigation Satellite System receivers.

Gravity Data Processing

Gravity measurements are affected by several factors and each must be accounted for in order to provide the highest quality results. The LaCoste and Romberg model G is capable of measuring microgal ($\sim 10^{-8}$ m/s^2) level acceleration variations of the Earth's gravitational field with an established resolution and repeatability of 10 μGal. The gravitational field varies with the distance from the center of the Earth and thus the elevation of the instrument affects the gravity measurement. A free-air correction accounts for the contribution of the instrument elevation and is an initial step in processing gravity data after corrections for instrument drift and Earth tides have been performed. Centimeter vertical position accuracy is required to achieve a μGal level accuracy in the free-air corrected gravity readings. Real-Time Kinematic (RTK) mode GPS surveys were performed by simultaneously collecting carrier-phase GPS data at individual gravity stations and at a fixed base station location. RTK mode assists with evaluating position solution quality in the field. Repeat gravity and GPS data were also acquired at a subset of stations and observed data errors were approximately 22 μGal and 20 cm respectively.

The free-air corrected gravity data are shown in Figure A.22. Gravity data are often further reduced using the Bouguer correction method that aims to correct for any additional mass between the gravimeter and mean sea level. The approach followed here is instead to directly model the gravitational response of both the surface topography and subsurface structures and not rely on simplifying assumptions inherent with Bouguer corrections.

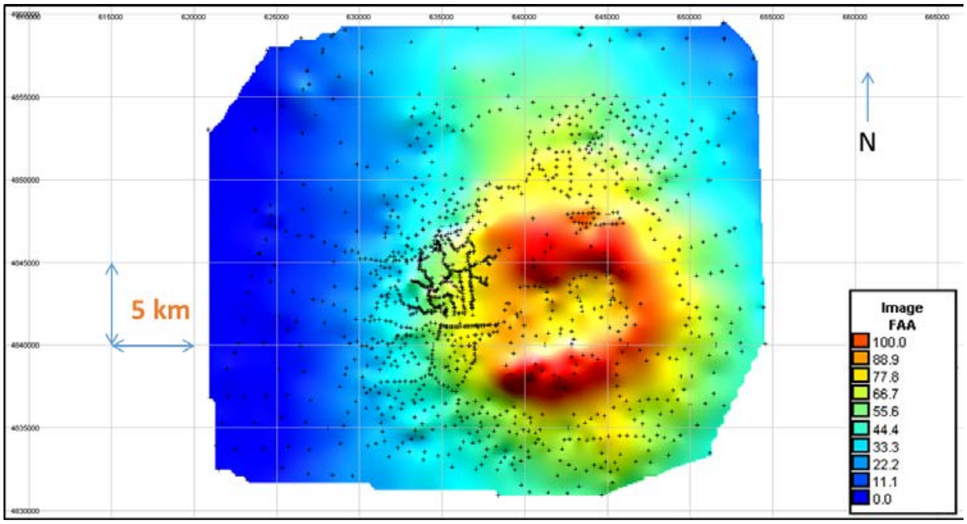

Figure A.22. Free-air anomaly map. Color map units are in mGal. Dots correspond to location of the gravity stations used in the analysis.

Gravity Modeling

Gravity modeling analysis was performed using ENcom Model Vision™ 12.0, a 3D numerical modeling software. Surface topography can be accurately measured and serves as the uppermost bounding surface of the first body included in the gravity modeling. For this analysis, a digital elevation map with a 100 m spaced grid was used to describe the surface topography. The elevation map was digitized using triangular elements to numerically define the upper surface of the gravity model. A gravitational body was defined from the upper surface down to 1250 m above sea level (ASL) and given a density of 2.2 g/cm^3.

The gravitational response of this body can then be modeled and compared to the observed gravity data. Additional subsurface structures were added to improve the fit between the modeled and observed data. In addition to the surface topography residual gravity data, results from seismic tomography surveys performed at the site were used to guide the design of additional subsurface structures for inclusion in the gravity modeling. The set of modeled gravity body consists of a single shallow body near the center of the caldera, four shallow ring structures, two mid-depth intrusive bodies, and one deep intrusive body.

Gravity Inversion

Inversion of the gravity data was also performed using ENcom Model Vision™ 12.0. A constrained inversion was performed where only the density values and depths of the anomalies were allowed to vary. The free parameters were adjusted to minimize the errors between modeled and observed gravity values.

Three main bodies with similar densities can be identified and they are represented in Figure A.23. The corresponding model parameters are listed in Table A.5. Densities of the middle and lower intrusive bodies (~2.6 to 2.7 g/cm^3) are consistent with rhyolite, basalt, or granites. The modeled density of the near-surface caldera body matches that of a low-density tephra material and the density of the shallow ring structures contained in the upper kilometer corresponds to that of welded tuff or low-density rhyolites. The density log for NWG 55-29 is shown in Figure A.24 along with average density values at specific depths and the values obtained from the gravity inversion results. Modeled bodies are in reality a composite of thin layers; however, average densities of the modeled gravity bodies are generally consistent with the density/lithology observed from well logs at the NEWGEN FORGE site (Figure A.24).

Table A.5. Gravity modeling parameters for each of the subsurface structures.

NAME	ELEVATION (m ASL)	DEPTH AT NWG 55-29 (m bgs)	THICK-NESS (m)	DENSITY ANOMALY (g/cm^3)	BACKGROUND DENSITY (g/cm^3)	DENSITY (g/cm^3)
Terrain	1800-500	0-1300	-	0.00	2.30	2.30
Caldera_NS	1950-1450	-	500	-0.35	2.30	1.95
Ring_North	1900-1100	-	800	0.12	2.30	2.42
Ring_South	1900-1100	-	800	0.20	2.30	2.50
ASL_Block	500-0	1300-1800	500	0.00	2.50	2.50
Ring_West	1900-1100	-	800	0.19	2.40	2.59
Ring_East	1900-1100	-	800	0.14	2.40	2.54
Upper_Middle_Intrusive_West	1100-500	-	600	0.24	2.40	2.64
Upper_Middle_Intrusive_East	1100-500	-	600	0.18	2.40	2.58
Middle_Intrusive_West	500-0	-	1100	0.19	2.40	2.59
Middle_Intrusive_East	500-0	-	1100	0.20	2.40	2.60
Lower_Intrusive	0-(-2000)	1800-3800	2000	0.11	2.50	2.61
WestFlank_Intrusive	(-800)-(-5000)	2600-6800	4300	0.16	2.50	2.66
Rift_Zone	(-2000)-(-5000)	(-3800)-(-6800)	3000	0.18	2.50	2.68

bgs = below ground surface

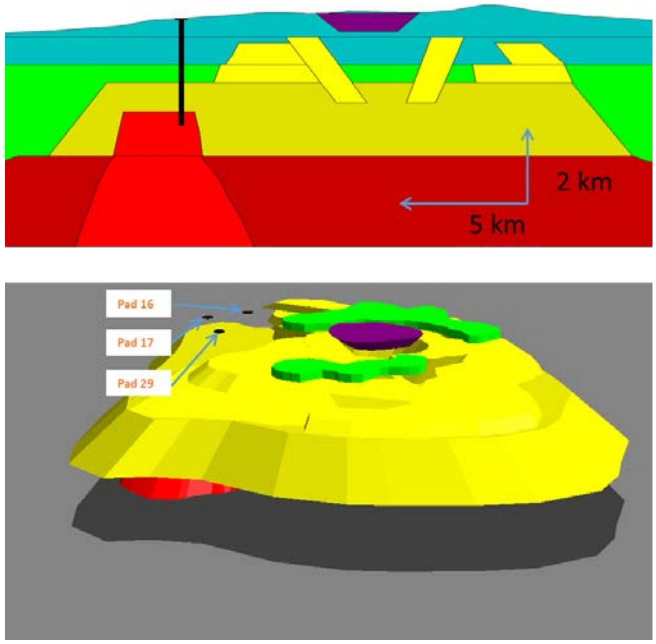

Figure A.23. A cross section through well Pad 29 (upper plot) and 3D perspective view (lower plot) of the higher density bodies responsible of the main observed gravity anomalies modeled for the NEWGEN FORGE site.

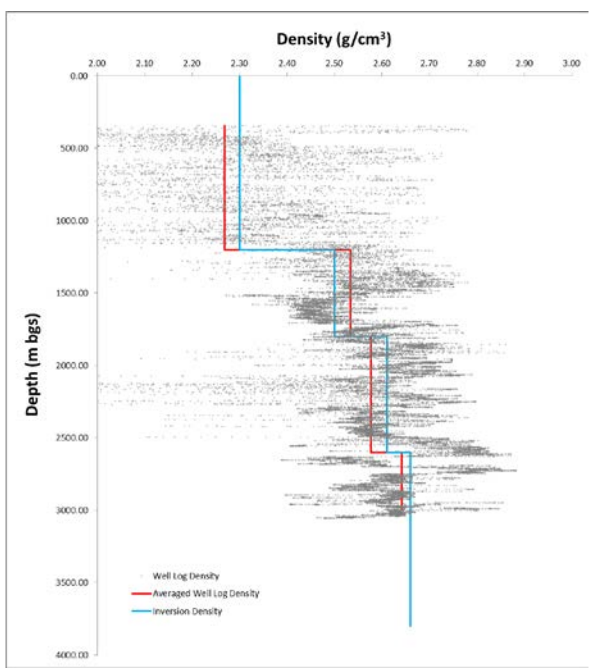

Figure A.24. NWG 55-29 density log (gray points) along with an averaged log density (red) over specific depths intervals and a comparison to the density values obtained from the gravity inversion (blue).

Final gravity data residuals show that most of the observed gravity data can be explained by the modeled gravity bodies. The inversion attempts to minimize the errors for all of the data and a residual map (not represented) illustrates that the gravity residual is in general slightly positive in the center of the area and negative toward the western edge of the domain. Edge effect artifacts can be seen on the periphery and are due to truncation of the model domain. An improved fit to the center of the area can be obtained by slightly increasing the density of all modeled bodies but will cause the western negative residual to become more pronounced. Overall, the inversion results provide good fits to the gravity data and are consistent with previous gravity modeling results and other site characterization information.

A.2.10 Geothermal Exploration

A.2.10.1 Drilling Results

The ring fractures have been the target of two wells and two core holes drilled by CE. However, no geothermal fluids were encountered in these attempts. TCH 88-21 encountered a highly sheared zone around the 1036 m (3400 ft) depth, which was initially interpreted as a ring fault dipping around 65° toward the central caldera. Only very minor fluid losses were encountered in this zone, and the equilibrated temperature profile measured across this interval was conductive, also indicating limited fluid flow or permeability in the fracture zone. NWG 55-29 was drilled within 2 miles of the caldera rim and near the projection of ring fractures, so it was possible that hole might potentially intersect one of the ring fractures. However, well data from drilling logs, mud logs, and BHTV data revealed no evidence of fractures or faults in NWG 55-29 (see below) or cuttings analysis (Letvin 2011).

Data on lost circulation encountered while drilling, which could be used to identify permeable fault or fracture zones, among other things, were compiled for eight wells and TCHs around the NEWGEN FORGE site. In general, the upper, permeable, and isothermal zones for almost all wells and TCHs showed significant problems with lost circulation. The depth of this zone varies, but upper level losses usually decreased around the 200 m (656 ft) depth. At the bottom of this zone, the temperature profiles become conductive and drilling problems minor. In all eight wells and TCHs examined major loss zones were not prevalent below 340 m (1120 ft).

A.2.10.2 Thermal Measurements and Exploration Wells

Two core holes and two relatively shallow geothermal exploratory have been drilled in the caldera (Figure A.7) base of the isothermal zone; shallow wells were drilled by the USGS (USGS N2) and Sandia (RDO-1). A maximum temperature of 265°C (509°F) was measured in USGS N-2 at its total depth of 932 m (2990 ft). A maximum temperature of 160°C (320°F) at a total depth of 411 m (1320 ft) was encountered in RDO-1.

Four deep exploratory wells have been drilled on the northwestern flank of the volcano (Figure A.7) two by CE (CE 86-21 and CE 23-22) and two by Davenport (NWG 55-29 and NWG 46-16). CE also drilled two temperature core holes (CE 76-15 TCH and CE 88-21 TCH). The temperature profiles indicate a conductive regime from an elevation of about 1700 m to total depth at -1300 m (Figure A.25). While CE 86-21 and CE 23-22 exceeded 315°C (600°F) below 2740 m (9000 ft), Spielman and Finger (1998), concluded that while adequate temperatures are present the permeability in the four CE wells was too low for a commercial geothermal resource.

A.2.10.3 Thermal Conductivity

Thermal conductivity measurements on 94 rock cores (Wells GEO N-1, GEO N-2, GEO N-3, GEO N-4, GEO N-5, Santa Fe NC-01, and Santa Fe 72-03) were compiled from Blackwell (1994). In addition, measurements on cuttings from CE 23-22 (46 samples), NWG 46-16 (9), and NWG 55-29 (14) were completed by Frone (2015). Measurements on cores and cuttings were completed following the procedures of Blackwell and Spafford (1987) on water-saturated samples. Measurements are conducted at ~20°C and need to be corrected for higher temperatures using equations for magmatic and metamorphic rocks from Vosteen and Schellschmidt (2003). The temperature correction for volcanic rocks is up to 32% lower thermal conductivity at temperatures above 275°C (Frone 2015)(Figure A.26). Final thermal conductivity values shown in Table A.6 are averages of all measurements from within the corresponding gradient interval.

A.2.10.4 Porosity and Permeability

The average porosity measured on core samples in Well GEO-N2 (the closest to NEWGEN FORGE site) is 5.3% (see Table D.7 in Appendix D).

The well data, bulk permeability, and injectivity test data for several exploration wells and core holes on the northwestern flank of the Newberry volcanic edifice in close proximity to the NEWGEN FORGE site are summarized in Table A.7. In each attempt to flow test wells, injected water boiled, flowed out of the well, and the wells ran dry because there were no formation fluids to replace the boiling water:

- Well CE 86-21 was flow tested between November and December of 1995. Water was injected at 5.4 L/s (85 gpm) and wellhead pressure (WHP) of 0.34 MPa (50 psi), and then nitrogen was pumped to 2134 m (7000 ft) through coiled tubing to lift the water column. The well unloaded but stopped flowing after 4 hours. A second injection test was conducted at 3.1 L/s (49 gpm) at a pressure of 5.5 MPa (800 psig) for 5 hours, with similar results.
- Well CE 23-22 was flow tested between December 1995 and January 1996. Water was injected at 7.6 L/s (120 gpm) and WHP of 1.4 MPa (200 psig). After injecting 15 m^3 (4,000 gallons) of 15% HCl solution, a second injection test at 5.0 L/s (80 gpm) and a 9.31 MPa (1350 psig) WHP was conducted. An attempt to flow the well by injecting nitrogen at 2530 m (8300 ft) on April 20, 1996, was unsuccessful.
- Attempts to flow Well NWG 46-16 were made from October 24–27, 2008, while the rig was still on the hole. The well was air-lifted several times at different depths, but would not flow unassisted. During these attempts, with the reduced hydraulic pressure in the hole, a section of poorly cemented tuff became unstable and bridged the well effectively preventing any further flow testing.
- Well NWG 55-29 was flow tested in July 2008 while the drill rig was still on the hole. The well was air-lifted several times, in stages of increasing depth, but would not flow unassisted. Each time the well released only the small amounts of water and noncondensable gases that had accumulated in wellbore. At the end of the test, CO_2 gas readings were in excess of 30,000 ppm without air assist. On July 19, 2008, a 30-minute injection test gave no indication that the formation was capable of accepting injection water at a surface pressure of 6.7 MPa (970 psig). In September and October 2010, two injection tests were conducted to cool the wellbore for BHTV logging and establish baseline injectivity. Injection rates were 0.63 kg/s (5000 lb/hr) and 1.32 kg/s (10,500 lb/hr), and calculated injectivities were only 0.013 kg/s-bar (0.007 kph/psi) and 0.026 kg/s-bar (0.014 kph/psi), respectively.
- From 2010 to 2014, several well tests and model runs were performed on NWG 55-29 as part of the NEGSD (AltaRock 2015). An initial permeability 1×10^{-17} m^2 was used, consistent with native state modeling and limited measurements. After stimulation, a bulk permeability of 7×10^{-17} m^2 was modeled in the 200 m surrounding the well. Based on injection and fall-off data analysis, the near-well permeability was estimated to be ~1.44×10^{-15} m^2 and 1.34×10^{-15} m^2, respectively, which is

consistent with model results in which elements within 50 m of the well required permeabilities of 1 to 1000 × 10^{-16} m^2 in order to match the pressure versus flow records.

- NWG 55-29 was flowed twice during the NEGSD. Each time the well was shut-in at the end of an injection period with an initial WHP of ~180 bar (2600 psi) and allowed to heat up for 7 and 4 days. Initially, the well began flowing on its own at 9.5 and 12.6 L/s (150 and 200 gpm) due to the reservoir pressure created by prior water injection. The initial flow rate declined while the flowing water heated up. Eventually, the water temperature reached the boiling temperature for water at the elevation of the wellhead, 93.8°C (201°F), and the well began geysering. During the geyser period, the flow was characterized by four to six short periods of high flow 1200 to 1900 L (300 to 500 gallons) per hour followed by long periods with no flow from the well. Thus, the average flow was approximately 3.2 L/s (50 gpm) and the total flow over 30 and 48 hours was approximately 363 and 440 m^3 (96,000 and 116,000 gallons).

To conclude, test results for all of the wells found injectivities several orders of magnitude lower than the lowest permeability of typical geothermal producers—geothermal well injectivities typically range between 1.8 and 1800 kg/s-bar (1 to 1000 kph/psi) (Spielman and Finger 1998). Bulk permeability for CE 23-22 was determined to be 0.26 mD. By comparison, permeability in geothermal fields such as Coso and the Salton Sea range from 25 to 300 mD (Spielman and Finger 1998).

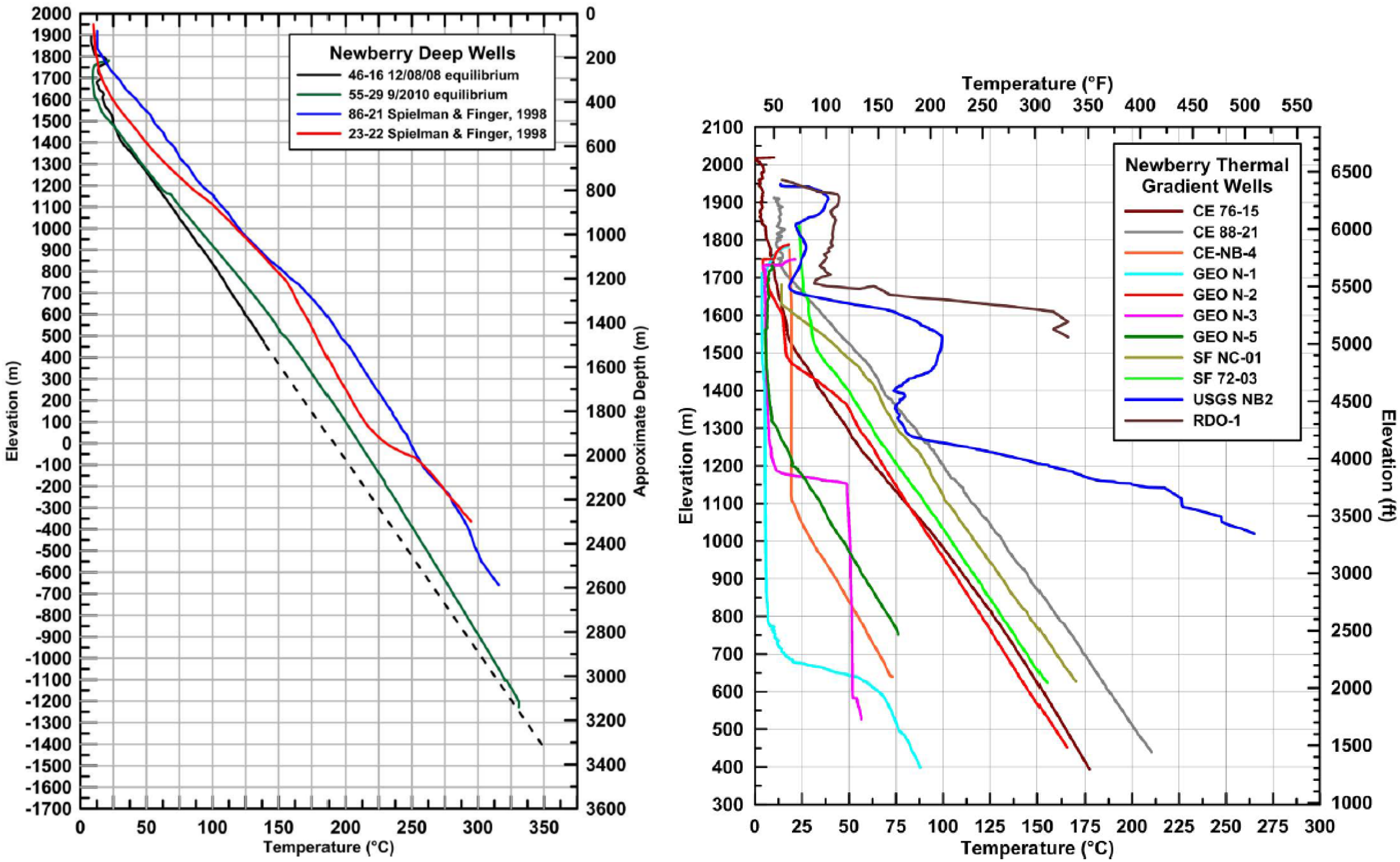

Figure A.25. Equilibrated temperatures of core holes and exploration wells at Newberry Volcano from Frone (2015). Depths are relative to mean sea level. Wells locations are shown in Figure A.7.

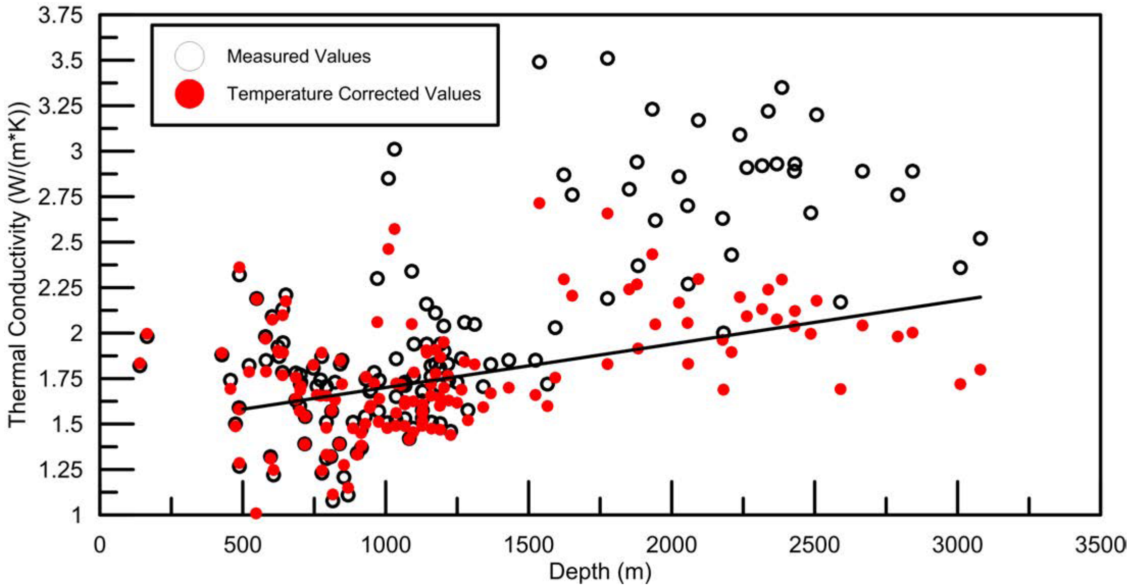

Figure A.26. Thermal conductivity versus depth for measured values on cores and cuttings. Open circles are measured values. Red filled circles are temperature-corrected values, corrected for in situ temperatures using equation from Vosteen and Schellschmidt (2003). (From Frone 2015).

Table A.6. Thermal gradient and thermal conductivity (from Frone 2015).

WELL NAME	LAT. (WGS84)	LONG. (WGS84)	ELEVA-TION (m)	DEPTH INTERVAL (m)	GRADIENT (°C/km)	σ	THERMAL CONDUCTIVITY (W/(m.K))	σ	N
CE 23-22	43.7430	-121.2871	1946.8	800-1175	158.9	1.46	2.09	0.35	6
“	“	“	“	1250-1850	88.0	0.55	2.32	0.35	5
“	“	“	“	2025-2436	138.3	2.01	2.14	0.11	10
NWG 46-16	43.7516	-121.3013	1882.8	600-1439	112.8	0.04	1.61	0.07	3
NWG 55-29	43.7261	-121.3158	1772.4	650-1175	135.2	0.06	1.52	0.12	6
“	“	“	“	1300-1950	108.6	0.04	1.95	0.21	5
“	“	“	“	2000-2875	99.4	0.02	1.93	0.16	8
Santa Fe 72-03	43.7015	-121.2741	1990.3	600-1366	136.9	0.09	1.60	0.11	16
CE 76-15	43.7513	-121.2796	2060.0	500-750	132.1	0.08	1.61	0.25	-
“	“	“	“	800-100	170.2	0.14	1.68	0.25	-
“	“	“	“	1400-1634	119.1	0.09	1.82	0.25	-
CE 86-21	43.7359	-121.2899	1908.7	400-1000	132.4	0.30	1.63	0.25	-
“	“	“	“	1300-2000	105.7	0.22	1.86	0.25	-
CE 88-21 TCH	43.7335	-121.2904	1900.0	200-400	184.2	0.82	1.53	0.25	-
“	“	“	“	800-1476	147.2	0.13	1.74	0.25	-
CE NB-3	43.6688	-121.1878	1960.0	1275-1311	106.2	2.83	1.76	0.25	-
CE NB-4	43.7817	-121.2914	1775.0	650-1134	115.6	0.17	1.66	0.25	-
GEO N-1	46.6383	-121.2417	1786.1	1200-1388	95.6	0.26	1.86	0.08	3
GEO N-2	43.7269	-121.3114	1790.7	600-1335	128.9	0.06	1.51	0.15	8
GEO N-3	43.8316	-121.2449	1752.6	1198-1216	52.8	0.37	1.70	0.16	4
GEO N-4	43.7090	-121.1372	1908.0	540-615	98.0	1.39	1.93	0.2	4
GEO N-5	43.6802	-121.3103	1731.3	550-980	121.6	0.13	1.61	0.35	13
Santa Fe NC-01	43.7269	-121.2999	1834.9	500-1207	138.8	0.09	1.56	0.11	15

Thermal conductivity values are averages of all measurements from within the corresponding gradient interval. Error estimates are based on measurement repeats of 20 cores and 20 cutting samples. The average repeatability for samples is 0.08 and 0.10 w/m*k for core and cuttings, respectively.

Table A.7. Well data and injectivity test results from nearby Newberry wells and temperature core holes (Spielman and Finger 1998; AltaRock 2011).

WELL	TEST DATE	TOTAL DEPTH (m)	MAX STATIC TEMP. (°C)	BOTTOM-HOLE GRADIENT (°C/km)	INJECTION RATE (kph)	WHP (psig)	INJECT-IVITY (kph/psig)	INJECT-IVITY (A) (gpm/psig)
CE 76-15(b)	11/18/95	1634	177	NA	1	300	0.0015	0.0030
	11/18/95				2	300	0.0031	0.0062
CE 86-21(c)	12/02/95	2804	317	86-98	42.5	50	0.11	0.2196
	04/18/96				25	800	0.022	0.0439
CE 23-22	01/08/96	2927	294	86-98	60	200	0.026	0.0519
	01/21/96				40	1350	0.024	0.0479
CE 88-21 TCH	NA	2804	317	NA	NA	NA	NA	NA
NWG 55-29	08/2008	1486	211	93	NA	970	NA	NA
	09/2010				5	751	0.007	0.014
	10/2010				10.5	1153	0.014	0.030

(a) Water level was approximately 775 ft in all the wells; therefore, liquid head at zero WHP was assumed to be 333 psi. This is added to WHP to calculate injectivity.

(b) Temperature core hole

(c) According to Spielman and Finger (1998), holes were discovered in the 13⅜-inch casing after this test. The second test on CE 86-21 was after casing repair.

NA = not available.

A.2.11 Conditions at the Proposed NEWGEN FORGE Site Area

NEWGEN proposes that its FORGE activities start at two drilling pads with existing deep wells, Pad 29 and Pad 16, and eventually use another drill pad, Pad 17 (Figure A.27). Note that the triangle shown in the map links the potential NEWGEN FORGE wells and drill sites. The entire Davenport Newberry Holdings (DNH) lease area shown on the map is available. In this section, the subsurface conditions encountered at NWG 55-29 and NWG 46-16 are presented, as well as a prognosis for drilling at Pad 17.

A.2.11.1 Conditions at Pad 29 from the Well NWG 55-29 Wellbore

This section describes the subsurface conditions encountered at Well NWG 55-29, and these conditions can be expected in future wells that may be drilled on Pad 29. Because this well was characterized for use in the NEGSD, these data are considered the most robust of any well completed at Newberry Volcano.

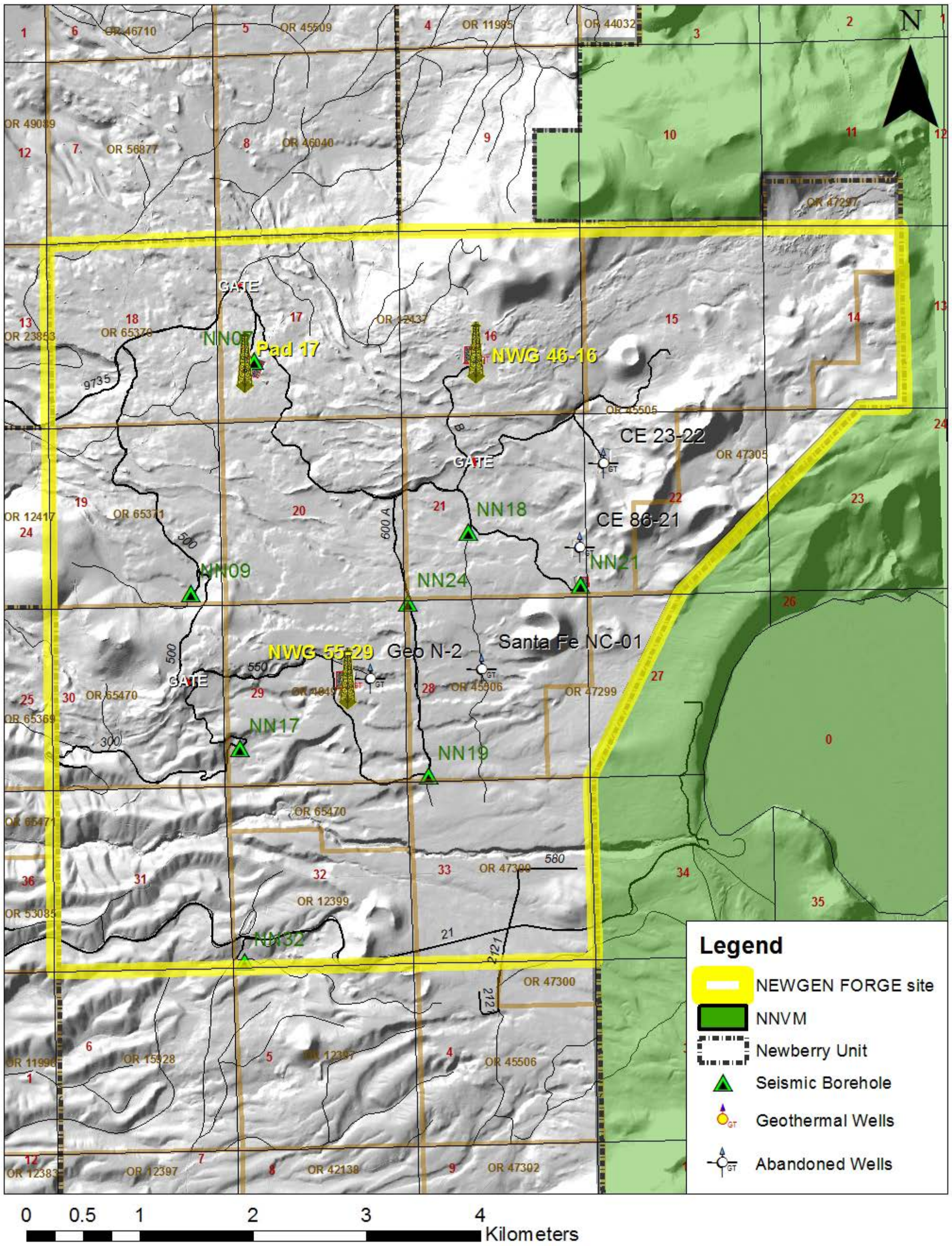

Figure A.27. Proposed NEWGEN FORGE site. DNH leases cover all but the map edges (outside heavy dashed lines).

Pad Setting

NWG 55-29 was drilled in an area of the west flank away from any surface expressions of the caldera ring fractures mapped elsewhere. LiDAR analysis of the mapped ring fractures northeast of Pad 29 reveals curved vent fissures and tentatively correlated vent alignments that end more than 3 km (1.9 mi) from the Pad. Dip-slip fault offset along the ring fractures was not observed in the LiDAR surfaces. Pad 29 is located on the edge of a gravity high anomaly identified by Gettings and Griscom (1988) and confirmed by the present study (cf. Section A.2.9.4). The open-hole interval of Well NWG 55-29 extends between 1903 m (6242 ft) to 3066 m (10,060 ft) total measured depth (TMD). The well first intersects microcrystalline granodiorite at a measured depth of 2627 m (8620 ft). This is the first of 12 granodiorite (average thickness 29 m) or felsic (average thickness 9 m) dikes or sills with alternating subvolcanic basalts to total depth.

Drilling History and Lessons Learned

Drilling NWG 55-29 began April 13, 2008, and was completed to 3066 m (10,060 ft) TMD on July 22, 2008. The upper zone of the well from the surface to approximately 305 m (1000 ft) had significant lost circulation and borehole stability issues because of the rubble zones, cinder, and unaltered tuffs encountered while drilling. Highly viscous lost circulation mud pills and cement plugs were used with varying degrees of success. Mud losses were inevitable and were managed with excess mud volume in the drilling of the upper part of the hole. When drilling reached the altered volcanic layer containing smectite, chlorite, and kaolinite in the 305 m (1000 ft) interval, the permeability decreased rapidly and major loss zones ceased.

Below the surface casing shoe at 338 m (1108 ft), the wellbore is characterized by a conductive gradient of 109 to 128°C/km (6 to 7°F/100 ft). At these conditions, mud coolers and high-temperature tools were necessary during drilling. Loss zones encountered in the deeper part of the well were intermittent and less problematic than in the upper 305 m (1000 ft) intervals. The rate of penetration was highly variable and dependent on lithology and the presence of fractured intervals.

Casing Profile

The casing profile of NWG 55-29 (Figure A.28) begins with a 30 in. conductor casing set to 40 m (130 ft), followed by 20 in. surface casing set at 338 m (1108 ft), and 13⅜ in., 72 lb/ft L-80 rating casing set at 1339 m (4391 ft). The 9⅝ in. production casing was set from 1277 to 1970 m (4189 to 6462 ft). In 2014, 9⅝ in. casing was tied back from 1277 m to the surface in order to plug casing leaks that developed in the 13⅜ in. casing during the 2012 stimulation. A 7-in. perforated liner, installed in 2014, extends from 1970 to 3066 m (6462 to 10,060 ft). Below 854 m (2800 ft), well inclination builds over 10° due east to a maximum deviation of 15° at TD. The total easterly drift from the wellhead to TD is 530 m (1740 ft).

Lithology and Mineral Alteration below Pad 29

Lithologies below Pad 29, described from 10-ft interval drill cuttings from NWG 55-29, include a wide variety of volcanic, volcanoclastic, and hypabyssal units, ranging from ash flows and debris flows, to silicic domes, mafic flows, and mafic, granodiorite, and felsic dikes (Epoch 2008a). The lithology is heterogeneous, but is grouped into the following general categories in the report:

- Unaltered Volcanic Sequence, 42.7 to 951.0 m (140 to 3120 ft)
- Intercalated Bleached Ash Tuff, Lava and Crystal Lithic Tuff, 951 to 1463 m (3120 to 4800 ft)
- Chloritized Tuffs, 1463 to 1722 m (4800 to 5650 ft)
- Chloritized Volcanic Sequence (tuffs, basalts, andesites, rare felsic dikes), 1722 to 2627 m (5650 to 8620 ft)
- Granodiorite Intrusive and Basalt Subvolcanic, 2627 to 2956 m (8620 to 9700 ft)
- Basalt, Altered Basalt, and Felsic Dikes 2956 to 3066 m (9700 to 10,060 ft).

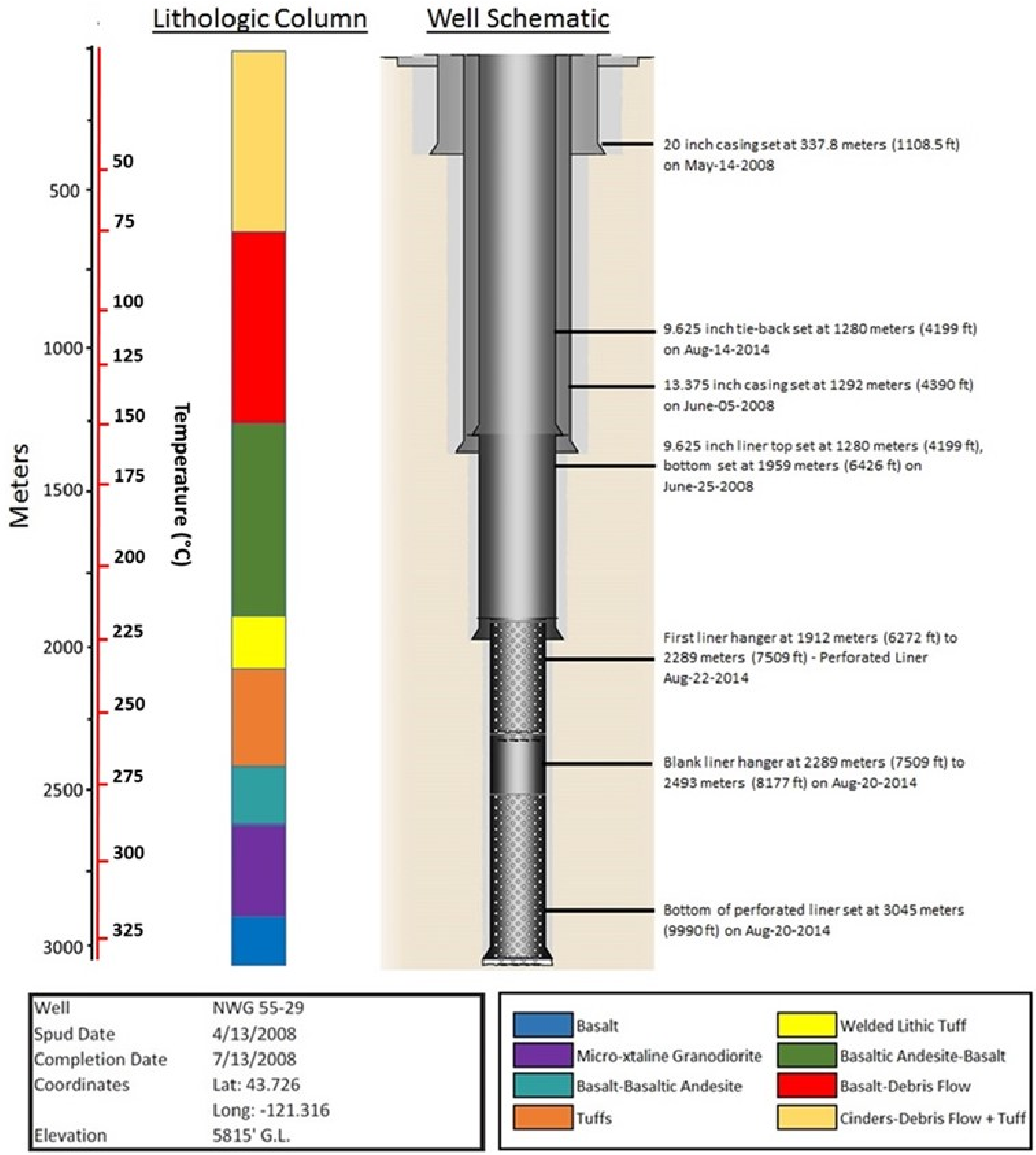

Figure A.28. Newberry NWG 55-29 wellbore and casing profile.

Geophysical Logging Data and Stress Orientation

Induction, spectral density, dual-spaced neutron, temperature, natural gamma ray, and caliper logs were obtained in NWG 55-29 by Halliburton during the drilling operation in the summer of 2008 using their high-temperature, high-pressure, hostile slimhole logging suite.

In addition to the open-hole log suite, both static and injecting pressure-temperature (PT) surveys were conducted after drilling operations. Further PT surveys conducted at the NEGSD site during 2010 and 2014 used fiber-optic distributed temperature sensing systems to track hydraulic stimulation.

The Sandia BHTV was run in October 2010 as part of the NEGSD using a logging truck from the USGS in Menlo Park, California. The image log spans from the casing shoe at 1970 m (6462 ft) to 2701 m (8860 ft), the depth at which the tool stopped working due to high temperature. The borehole breakouts seen in the BHTV showed a consistent azimuth indicating that the minimum horizontal stress, S_{hmin} is oriented at 092 ±16.6° (Figure A.29) relative to true north (Davatzes and Hickman 2011). This azimuth of S_{hmin}, in combination with the attitude of the majority of natural fractures revealed in the image log, is also consistent with normal faulting. The consistency of the breakout azimuth, without localized rotations, taken in combination with the extremely low rate of seismicity in the region and the weak expression of natural fractures in the image log, suggests that there has been little recent or active slip on fractures in the vicinity of the well (Davatzes and Hickman 2011; Cladouhos et al. 2011a).

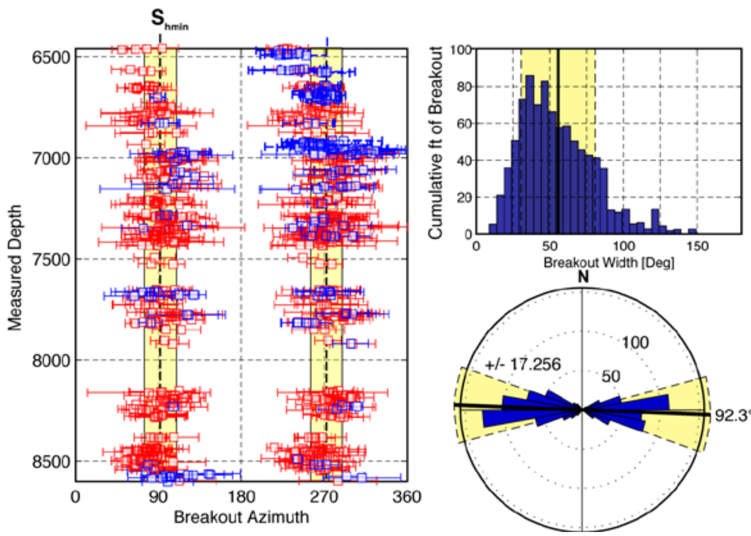

Figure A.29. Statistics of breakout occurrence in NWG 55-29. Left panel shows the vertical distribution of breakouts versus measured depth (ft), where horizontal bars indicate breakout width, red breakouts correspond to high-quality picks of paired breakouts, and blue breakouts are lower quality picks of single breakouts, typically in areas of poor image quality. Vertical yellow-filled boxes show the mean S_{hmin} azimuth plus-or-minus one standard deviation as calculated using circular statistics and weighted by the vertical extent of individual breakouts. The upper right histogram shows the distribution of breakout widths. The lower right rose diagram summarizes the cumulative height (ft) of breakouts in 10° azimuthal bins.

Determining the magnitudes of the three principal stresses is more difficult. In a normal faulting regime, the maximum principal stress is vertical (S_V) with a magnitude related to the weight of the lithostatic overburden. The minimum horizontal stress (S_{hmin}) at a given depth is best determined from a mini-frac, a well test in which S_{hmin} is determined from the fluid pressure at which tensile fracturing occurs. An accurate mini-frac requires a short (15 m) section of relatively unfractured wellbore to be isolated. Isolation allows for sufficient pressure buildup to cause tensile fracturing, provides a narrow depth range over which to calculate S_{hmin}, and ensures that the measured pressure response is due to a tensile failure and not hydroshearing. Because NWG 55- 29 has over 1000 m of open hole and isolating a short section would have required a drilling rig, it was not feasible to conduct a mini-frac to determine S_{hmin} prior to the first stimulation in 2012. S_{hmin} and the rest of the stress model was constrained based on reasonable geomechanical assumptions derived from injection tests and material properties (Davatzes and Hickman 2011; Cladouhos et al. 2011a). Based on this stress model (Table A.8) and a stimulation model, it was estimated that a WHP of 90 to 110 bar (1350 to 1550 psi) could initiate hydroshearing and a maximum WHP of 130 to 150 bar (1950 to 2150 psi) would have been needed to create a significant EGS reservoir (Cladouhos et al. 2011b).

Table A.8. Stress model around the NWG 55-29 wellbore.

COMPONENT	GRADIENT (MPa/km)	DIRECTION
S_v	24.1	vertical
S_{Hmax}	23.5	2° (N-S)
S_{hmin}	14-9–15.8	92° (E-W)
pH	8.8	Fluid pressure

The stimulation results of NEGSD also provide information about the stress magnitudes. See Section A.3 for further information. The experience during NEGSD at NWG 55-29 highlights the importance of performing tests designed to measure stress magnitudes (i.e., mini-fracs) during drilling. Any wells drilled as part of the NEWGEN FORGE project will include stress measurements at multiple depths.

Description of Rock Cuttings from NWG 55-29

The cuttings from NWG 55-29 were analyzed in detail for a graduate research thesis completed at The School for Renewable Energy Science at the University of Iceland the University of Akureyri (Letvin 2011). The interval chosen, 1707 to 2620 m (5600 to 8600 ft), spans the upper open-hole interval and extends above the casing shoe at 1970 m (6462 ft).

In general, the grade and degree of alteration increases with depth with some heterogeneity related to local conditions. Deeper, older units may have experienced multiple episodes of intrusion during the past tens of millions of years, unrelated to Newberry volcanism. Younger, less permeable dikes might be relatively unaltered, but surrounded by small contact aureoles. Fracture zones and zones that contained primary permeability, such as autobreccia and scoria zones, and have hosted hydrothermal fluids in the past show a greater degree of alteration than less permeable host units.

The most common pore-filling minerals in the cuttings from NWG 55-29 include calcite, quartz, hematite, and chlorite, with trace amounts of pyrite and epidote. Although these minerals often occur in veins, nearly all of these minerals can also be found filling primary vesicles throughout the full section of core analyzed. The occurrence of these minerals in both pore types suggests the same fluid chemistry accessed all open spaces, resulting in consistent mineral assemblages. The exception is opaline silica, which is associated with vesicles and not veins.

In addition to the precipitation of minerals in vesicles and fractures, several of the secondary minerals are distributed throughout the host rock. These minerals include pyrite, chlorite and hematite. Chlorite occurs interstitially at grain boundaries and as a replacement of primary minerals. Pyrite is generally located at grain boundaries. In addition to chlorite, other replacement phyllosilicates identified by X-ray diffraction analysis include illite/muscovite and kaolinite (see discussion below).

Paragenesis of NWG 55-29 Cuttings

Cutting and thin section analysis indicates that volcanic extrusives were initially altered by early chlorite replacement and quartz precipitation in both vesicles and fractures (Table A.9). At shallow depths, the analysis of Bargar and Keith (1999) documented well-developed clay alteration in fractured zones, which has also been supported by fracture studies by Fetterman (2011) and Fetterman and Davatzes (2011). However, in the NEGSD and NEWGEN depth intervals (>1800 m [6000 ft] depth) expandable clays such as smectite or mixed layer phases such as chlorite-smectite or illite-smectite are absent, and phyllosilicates are limited to chlorite, illite/muscovite, and kaolinite. Thus, the geothermal system has a clay-enriched cap, and the NEWGEN FORGE interval (175 to 225°C) lies well below this cap, as evidenced by the lack of expandable clays, consistent with surface resistivity measurements (Fitterman 1988). The most common vein-filling minerals are calcite and quartz, but chlorite and hematite also are common. Veins show repeated opening, regardless of mineral filling. The lack of a consistent pattern in the layering or in the cross-cutting relationship in veins by these minerals indicates repeated pulses of precipitation. The presence of quartz and calcite in many veins suggests precipitation associated with up-welling and down-welling fluids because of the relative impact of temperature on their solubility given the large temperature gradients in this borehole. The vertical extent of the fluid flow is uncertain, but there is no clear evidence of an extensive hydrothermal system (Letvin 2011).

Table A.9. Post-emplacement mineral alteration identified in wellbore NWG 55-29.

DEPTH INTERVAL (m)	MINERAL ALTERATION
0 to 951	Unaltered volcanic sequences; mud log notes (Epoch 2008a) show minor alteration to green clays, zeolites (e.g., natrolite), and kaolinite in some zones below about 274 m
360	Smectite becomes more common
506	Calcite first appears
870	Dominant type of alteration is calcite and smectite in veins and vugs
1341	Chlorite becomes more dominant but is heterogeneous with increasing intensity below 1524 m
1829 to 1951	Low-grade greenschist facies alteration (albite-chlorite-calcite) with epidote noted in increasing abundance below 1768 m
2134	Increasingly complex and abundant alteration products (chlorite-epidote-calcite-pyrite), with minor silicification noted at 2201 m; mud log notes a general lack of permeability
2187	Strong chloritization with an altered zone is found at 2262 m
2591	Higher greenschist facies alteration (chlorite-actinolite-albite-epidote)
2865	Basaltic to felsic dikes and sills are more abundant with increasing evidence of contact metamorphism

Potential FORGE Use of NWG 55-29

Potential future uses of Well NWG 55-29 for FORGE related R&D projects include:

- high-temperature instrument testing up to 320°C
- surface instrumentation can be deployed above the fractured network already created around NWG 55-29 to image fluids and deformation

- water can be injected into NWG 55-29 using the same equipment, permits, and methods as in 2014 to create a flow and deformation signal that can be used to test imaging technologies
- placement and testing of velocity calibration tools, such as either download instrument string or downhole seismic sources
- NWG 55-29 can be used in conjunction with NWG 46-16 to perform cross-hole seismic imaging to image vertical structures between these two deep wells

Further details of potential NEWGEN FORGE activities at NWG 55-29 can be found in the Statement of Work and R&D Implementation plan.

A.2.11.2 Conditions at Borehole GEO N-2

The core from GEO N-2 is of special interest for EGS design at the NEWGEN FORGE site, because the core was preserved, unlike core from CE core holes at Newberry Volcano, and is available for petrologic and mechanical study. The deepest core in GEO N-2 (1306 m [4285 ft]) is above the likely NEWGEN reservoir depth (1820 to 2440 m [6000 to 8000 ft]); therefore, collecting new core from deeper reservoir rocks will be a goal of the NEWGEN FORGE project. Nevertheless, analysis of the GEO N-2 core provides a useful reference point.

Background on GEO N-2

Drill hole GEO N-2 was drilled in 1986 by GEO Newberry Crater, Inc., at an elevation of 1779 m about 2.8 km outside the western rim of the caldera and 1 km away from NWG 55-29 (drilled in 2008). The drill site was chosen on the basis of a geophysical anomaly; the sites for most of the west flank drill holes at Newberry Volcano were selected because of electromagnetic or surface resistivity anomalies. A temperature profile for the geothermal well shows a bottom-hole temperature of 167°C (Figure A.25). The silica content of sampled fluids increases substantially near the bottom of the GEO N-2 drill hole due to the influx of thermal fluids (Bargar and Keith 1999). The well has since been plugged, but a core from it has been retained at the University of Utah, and has been analyzed for natural fracture formation, mineralogy, and rock mechanical properties.

Geologic Characteristics of Natural Fractures in Core

GEO N-2 core was analyzed by Fetterman and Davatzes (2011) for fracture formation and how it contributes to overall porosity or reduction in porosity due to hydrothermal mineral alteration and precipitation. They identified six stages of fracture evolution:

1. *Unfractured* – A control sample of cohesive basalt or andesite with no macroscopic, through-going fractures.
2. *Single Fracture* – A macroscopic structure representing a discontinuity in the rock defined by two distinct surfaces and lacking fault rock or closely spaced, linked macroscopic fractures.
3. *Linked Fractures* – A set of interconnected but mostly parallel fractures forming a network that still lack fault rock in the host rock. Fault rock and/or vein material between the two contact surfaces might be slickensided.
4. *Proto-Breccia* – Macroscopic splay fractures begin forming perpendicular to and creating large, isolated rock clasts adjacent to the central fault zone.

5. *Breccia* – Macroscopic fractures forming a network of interconnecting cracks and breccia. Typically, this system of fractures accommodates the majority of shearing as evidenced by localized, often discontinuous fault rock development.
6. *Fault Rock* – Extensive, continuous fractures with a center that is no longer clearly identifiable as fragments of host rock (protolith) in hand sample forming a distinct fault core. Typically associated with a well-developed damage zone of macroscopic fractures between the host rock and the fault rock.

Porosity was mapped from core photos and thin sections to characterize both macroscopic and microscopic porosity. The measured porosity was categorized as "Open" or present day open pores and "Skeletal" or the sum of open porosity and porosity that has been healed by hydrothermal mineral alteration and precipitation. X-ray diffraction analysis was done on rock samples to determine the mineralogy of both the host rock and the fracture filling minerals.

The crystalline host rock contains primarily fine-grained plagioclase, quartz, olivine, amphibole, and pyroxene. The primary porosity was found to be in vesicles that contained quartz and carbonates. There are also trace amounts of iron oxides, sulfates, sulfides, chlorites, and other clays from hydrothermal alteration. The fracture fill consists of mostly quartz with some calcite and dolomite, and the fracture surfaces are lined with chlorite. The fractures also contain other various clays and phylosilicates. Hematite is abundant in fracture fill in stage 2, and in stage 3, the fractures contained anhydrite.

Generally, the rocks have relatively low primary and secondary porosity; fracture permeability was enhanced in fracture evolution stages 2–4, but permeability was reduced in stages 5–6. The fracture roughness was observed to increase during stages 2–4 during fracture formation but decreased during the formation of breccia and fault gouge. The porosity begins at nearly 0% in stage 1 and reaches as high as 65% in stage 4. Most of the porosity is composed of elevated matrix permeability along fractures from within 2 cm of the fracture damage zone. Skeletal porosity also peaks at stage 4 but is mostly found within the fracture damage zone.

Rock Mechanics Testing of GEO N-2 Core

Two core samples were tested for mechanical properties: GEO N-2 4219.5–4221 and GEO N-2 4281–4282.5, named for the measured depth interval from which they were taken in the well (Figure A.30). Sample plugs 1 in. in diameter by 2 in. long were drilled from the cores vertically (V) and horizontally (H) to analyze mechanical anisotropy. The results of the analysis of five samples are presented by Wang et al. (2016) and summarized in Table A.10 below.

This study represents a small data set for the GEO N-2 core, and because of the high amount of variability of all of the cores tested at Newberry Volcano and within each core, more testing is required to fully characterize the mechanical behavior of these rock formations. New cores will be collected during the NEWGEN FORGE project, most efficiently as sidetracks from Well NWG 46-16, which is described in the next section.

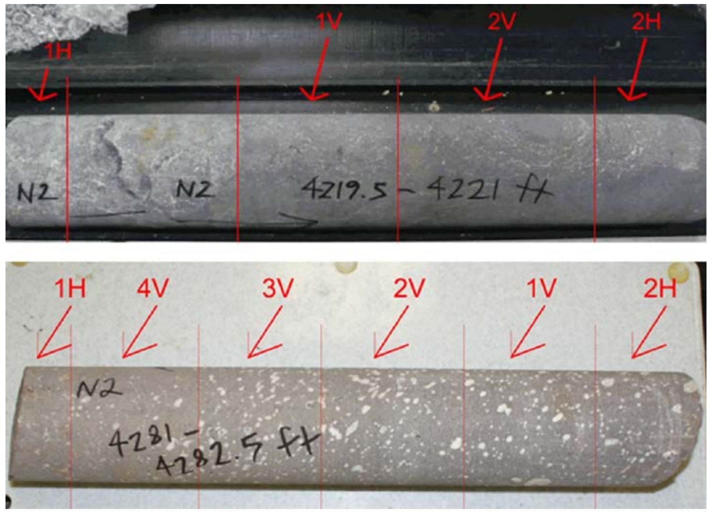

Figure A.30. Core samples from Well GEO N-2 from 4219.5 to 4221 ft MD (top), and from 4219.5 to 4221 ft MD (bottom) showing the location of 1 in. in diameter by 2 in. long sample plugs.

Table A.10. Summary of elastic, strength, and Mohr-Coulomb properties of GEO N-2 core. The parameters for a horizontal core, which is very low strength, are highlighted in green, and a vertical core, which is very high strength, are highlighted in red.

SAMPLE	COMPRESSIVE STRENGTH (MPa)	YOUNG'S MODULUS (MPa)	POISSON'S RATIO	UNIAXIAL COMPRESSIVE STRENGTH (MPa)	COHESION (MPa)	INTERNAL FRICTION ANGLE
GEO N-2 4219.5 2H	127.93	20.46	0.20	75.25	22.06	29.2
GEO N-2 4281 1V	120.69	24.45	0.26	-	-	-
GEO N-2 4281 2H	44.04	7.20	0.39	4.18	1.14	32.8
GEO N-2 4281 2V	100.64	9.31	0.30	27.18	7.84	30.1
GEO N-2 4281 3V	220.80	39.69	0.25	176.47	61.35	21.3

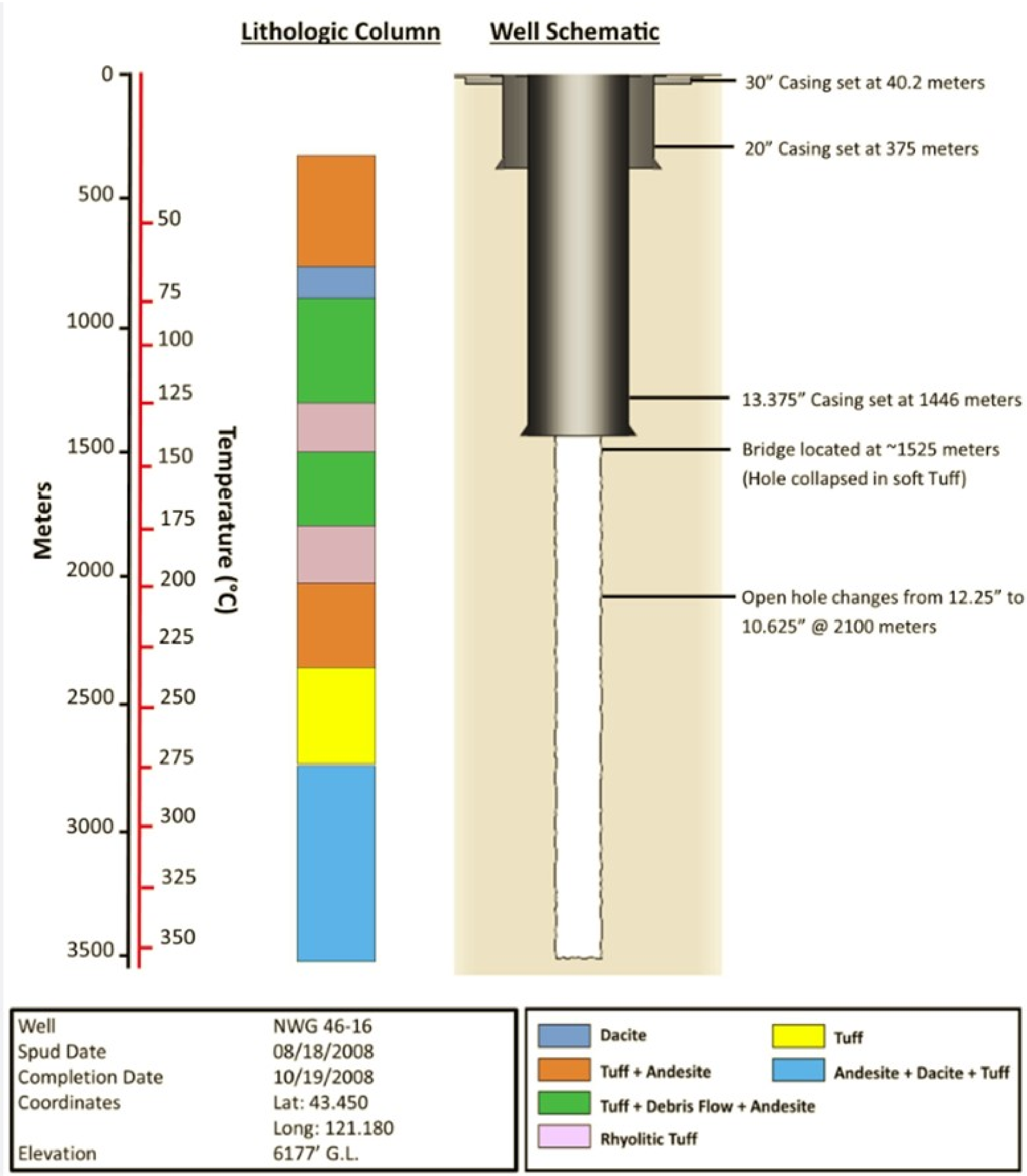

Figure A.31. Well NWG 46-16 completion, geology, and temperature.

A.2.11.3 Subsurface Conditions at Pad 16 from the Well NWG 46-16 Wellbore

This section describes the subsurface conditions encountered at Well NWG 46-16. These conditions can be expected in sidetracks or multi-laterals in the existing well or in future wells that may be drilled on Pad 16.

The second well Davenport drilled at Newberry was NWG 46-16. The well was sited to drill through a west-northwest striking linear gravity boundary. The well pad was located on the northern side of the boundary, and the well was directionally drilled southward, across this feature.

Drilling Summary

NWG 46-16 was initiated in August 2008 and completed at a TMD of 3553 m (11,599 ft) on 19 October 2008. The well is completed with 13⅜-in. surface casing to 1444 m (4736 ft), 12¼-in. open hole to 2100 m (6888 ft) and 10⅝-in. open hole to TMD, the true vertical depth (TVD) is 3493 m (11,461 ft). Figure A.31 is a well summary diagram showing the temperature, lithology, and casing profiles for the well.

Geology and Temperature Data

Rock formations encountered have been identified as belonging to the Newberry and Deschutes Formations from surface to 1366 m (4480 ft), and John Day Formation from 2332 m (7650 ft) to total depth. Below the casing shoe is a section of tuffs and debris flows to about 2057 m (6750 ft), below which is a section dominated by basaltic andesite lava flows to about 2301 m (7550 ft). Tuffs dominate again to about 2743 m (9000 ft), then lavas to about 2896 m (9500 ft), then tuffs again to about 3124 m (10,250 ft). The bottom section of the well is dominated by lavas except for a tuff section between 3261 m (10,700 ft) and 3353 m (11,000 ft). Drill cuttings show the same gradational weathering and diagenesis, grading to thermal metamorphism, as observed in NWG 55-29. Low-grade greenschist facies occurs below 1829 m (6000 ft). Below 2438 m (8000 ft), greenschist facies metamorphism increases to chlorite-albite-epidote (Epoch 2008b)

Mineral Alteration Observed in NWG 46-16

Drill cuttings show the same gradational weathering and diagenesis, grading to thermal metamorphism, as observed in Well NWG 55-29. Low-grade greenschist facies occurs below 1829 m (6000 ft). Below 2438 m (8000 ft), greenschist facies metamorphism increases to chlorite-albite-epidote. Evidence of past hydrothermal activity is observed in the cuttings from this well. At 1310 m (4300 ft), silica cementing in a microbreccia is observed. At 2255 m (7300 ft), fragments of drusy epidote and quartz vein minerals are observed. Intermittent traces of quartz and epidote vein minerals are observed occasionally through the rest of the hole, with an increase in the vicinity of 3383 m (11,100 ft) (Epoch 2008b; Waibel et al 2015).

Geophysical Logging Data

The following logs were run in NWG 46-16 during the drilling and completion operations:

- caliper/dip log from ~1462 to ~3536 m (4600 to ~11600 ft)
- gamma log from ~1463 to ~ 3536 m (4600 to ~11,600 ft)
- density log from ~1463 to ~3536 m (4800 to ~11,600 ft)
- resistivity log from ~1463 to ~3505 m (4800 to ~11,500 ft)
- density log from ~1463 to ~3536 m (4800 to ~11,600 ft)
- temperature logs from the surface to 3505 m (11,500 ft).

Flow Test Results

Attempts to flow the well were made from October 24–27, 2008, while the rig was still on the hole. The well was air-lifted several times at different depths, but would not flow unassisted. During these attempts, with the reduced hydraulic pressure in the hole, a section of cemented tuff became unstable and bridged the well, with some of the bridging fragments ultimately entering the casing from below, effectively stopping the flow tests.

NWG 46-16 was reopened in September 2013 as part of the Sigma Cubed microseismic monitoring program. The well was opened to atmosphere to bleed off the pressure, and then shut-in toward the end of the day to re-build WHP. The same exercise was repeated for 3 days with a goal of stimulating fluid flow within the fractures to create seismic noise that could be detected by the Sigma Cubed instruments. The flow line was a 4-in. pipe with a 90° elbow at the end to direct the flow upward. After the master valve was opened, a strong gas flow, reflective of the 550 psi WHP, commenced. After a period 1 to 3 hours, or at approximately 300 psi flowing WHP the flow changed from gas to a light brown liquid, indicative of drilling fluid that had been left in the hole. The temperature of the liquid started out as slightly warm and increased over time. The flow of the liquid lasted for about 1 hour, then changed to gas flow with short bursts of liquid flow (Waibel et al. 2015).

Waibel et al (2015) noted that a static WHP of 550 psi would indicate a depression of the water column over 1000 ft. Degassing of CO_2 within the liquid column appears to have been enough for the well to flow on its own during the 3-day test. No downhole noise was detected by the Sigma^3 array, which may indicate that either no formation debris were jostled during the flowing of the well or monitoring equipment were not within range to pick up any flow noise. Waibel et al (2015) labeled NWG 46-16 as the Newberry geothermal discovery well because of the druze epidote and epidote-quartz crystal clusters observed in the cuttings between 7330 ft to 9400 ft. Increases in CO_2 gases were observed in those zones (Figure A.32). Gas analysis from the 3-day test performed in 2013 concluded that majority of the gas sample collected were also CO_2 gas (Table A.11). It is difficult to distinguish the depth source of the CO_2 gas. The CO_2 detected during the 2013 flow test may be from the deep fracture zone or shallower zone between 2000 and 5000 ft. Further casing integrity logs such as Pressure, Temperature, Spinner, downhole camera, and/or caliper survey can be performed on NWG 46-16 to confirm the casing integrity of the 13⅜-in. casing.

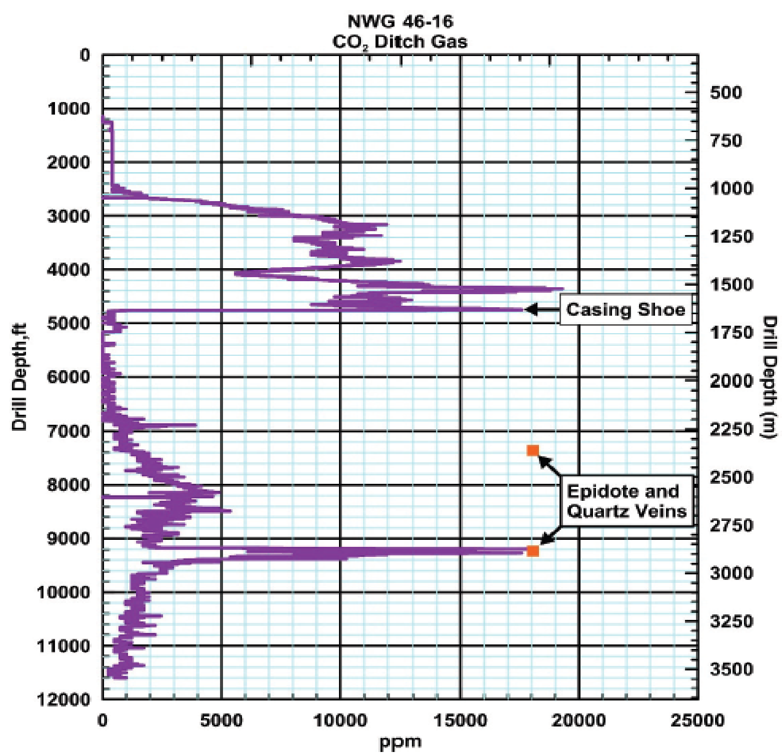

Figure A.32. CO_2 gas concentrations measured during drilling on Well NWG 46-16.

Table A.11. Gas analysis from Well NWG 46-16 (courtesy of USGS).

20130925	NWG 46-16	NWG 46-16	NWG 46-16
Date	9/6/2013	9/9/2013	9/10/2013
vol-%			
He	0.0014	0.0002	0.0002
H_2	<0.0002	0.0327	0.0418
Ar	0.0012	0.0013	0.0008
O_2	0.0006	0.0335	0.0023
N_2	4.4861	0.7393	0.6969
CH_4	2.0361	0.2695	0.3251
CO_2	92.2157	98.5465	98.5737
C_2H_6	0.0003	0.0003	<0.0002
H_2S	<0.0005	0.0077	<0.0005
CO	<0.001	<0.001	<0.001
Sum	98.7414	99.6311	99.6408
$\delta^{13}C$-CO_2	-4.58	-5.84	-5.98

With the blockage formed downhole at approximately 1525 m (5000 ft) no additional evidence was collected to confirm the existence of a hydrothermal system. Initial temperature logs were collected immediately after drilling, before the wellbore temperature equilibrated. Logs attempted in December 2008 only reached 1525 m (4737 ft) due to the blockage that formed after the flow testing. If a conductive temperature profile is assumed (like NWG 55-29) extrapolation of the December 2008 shallow temperature profile to depth gives a bottom-hole temperature of 350°C and a FORGE depth interval, temperature between 175°C and 225°C of 1800 to 2200 m (Figure A.25). The evidence of formation fluid flow can only be obtained via an equilibrium temperature and pressure survey. Additional logging will be conducted during NEWGEN Phase 2 to assess the current condition of the downhole blockage and validate the static bottom-hole temperature if a well workover or redrill is performed on NWG 46-16.

FORGE Use of NWG 46-16

Possible NEWGEN FORGE activities at NWG 46-16 and Pad 16 include:

- Clean out blockage at 1525 m.
- Sidetrack or sidewall cores at three different reservoir depths (1800, 2000, and 2200 m).
- Run BHTV to image borehole breakouts for stress orientations, fracture orientations, and find unfractured zones for stress magnitude measurements (see next bullet).
- Measure stress magnitude at multiple depths (1800, 2000, and 2200 m). This may require innovative techniques such as straddle packers. Perhaps stress measurements can be performed in sidetracks drilled for cores.

- Install downhole seismic monitoring equipment or downhole seismic source for velocity calibration.
- Cross-hole seismic survey paired with NWG 55-29.
- Completing current NWG 46-16 hole with production interval from 1800 to 2200 m, the depth range of the FORGE temperature requirement of 175 to 225°C.
- Sidetracking 46-16 in Phase 3.

Further details of potential NEWGEN FORGE activities at NWG 46-16 can be found in the Statement of Work and R&D Implementation plan.

A.2.11.4 Conditions at Pad 17 from Borehole TG 17-N

A geothermal well was not drilled on Pad 17 once Davenport operations were halted after the drilling of Well NWG 46-16. However, as part of the Innovative Exploration project, Davenport did drill temperature gradient hole TG 17-N on the north side of Pad 17 to a depth of 290 m (950 ft); this borehole was used as seismic monitoring station NN07 during the NEGSD. Lessons learned during the drilling of borehole TG 17-N can be used to demonstrate what can be expected when drilling the first 290 m (950 ft) of any new wells at Pad 17. Drilling TG 17-N was particularly difficult because of drilling losses and unstable rock conditions. In the upper 15 m of the borehole, formation collapse halted drilling twice and each time the borehole had to be cemented back to the surface. Between 15 and 290 m, the borehole had to be periodically refilled with cement at the end of nearly every drilling day to stabilize conditions and enable additional deeper drilling. In the end it took 22 days to drill to the total borehole depth and then an *additional* 40 days to set a 5-in. casing within the hole. Finally, conductively heated reservoir rock material was encountered at a depth of 168 m (550 ft). The well was isothermal from the surface to 168 m, 5 to 6°C (41 to 43°F), and below that level, the temperature increased 6°C between 175 to 225 m. At that temperature gradient of 120°C/km, which is comparable to that measured in Well NWG 46-16, a temperature of 175°C would be reached at 1600 m and 225°C at 2000 m.

A.3 Newberry Volcano EGS Demonstration

In 2009, AltaRock, in partnership with Davenport, was awarded a DOE grant funded by the American Recovery and Reinvestment Act to demonstrate EGS technology at Newberry. NEGSD was initially planned to consist of three phases:

- **Phase 1:** Extensive planning and permitting from 2010 to spring 2012. This included creating public outreach campaigns and the Induced Seismicity Mitigation Plan and planning the stimulation program.
- **Phase 2:** Initial stimulation of NWG 55-29 in 2012; NWG 55-29 workover and re-stimulation in 2014; drilling of NWG 55A-29 production well and subsequent stimulation.
- **Phase 3:** Well interconnectivity test; power plant planning and construction.

The goal of the demonstration was to create a functioning EGS in a hot and impermeable volume of rock using new stimulation and characterization techniques. Many of the technologies and characterization methods have been verified and field tested. During 2014, a significant volume of rock was stimulated, enhancing both the permeability and the volume of the fractured reservoir at depth. Unfortunately, the funding expired in the fall of 2015; therefore, NEGSD ended midway through Phase 2, prior to drilling the production Well NWG 55A-29.

A.3.1 Summary of Results

The following summary is taken from Cladouhos et al. (2015b, 2015c) and AltaRock (2014, 2015).

During Phase 1, the NEGSD project team studied existing data and gathered new regional and wellbore data to develop a comprehensive geoscience and reservoir engineering model of the resource underlying the demonstration site. AltaRock formulated a detailed plan to conduct Phase 2 operations, which included seismic monitoring, stimulation, drilling, and testing. Concurrently, the team assembled a large array of project information to conduct public outreach and inform regulatory agencies. The completed tasks include implementing a public relations campaign by distributing information and determining stakeholder concerns through the use of public meetings, website and social media, and providing detailed project plans and background information to aid the Environmental Assessment and the Phase 1 stage-gate review.

Phase 2 of NEGSD began in late May 2012, with the drilling of four new MSA monitoring holes (NN17, NN19, NN21, and NN24) to depths between 213 and 246 m. Seismic equipment was installed at seven borehole sites and eight surface sites in early August 2012. After the MSA was ready, the 7-week stimulation of NWG 55-29 began. The WHP reached 167 bar (2450 psi), 40,000 m^3 (11 million gallons) of water were injected, and over 175 microearthquakes were located, illuminating a cloud of microearthquakes extending 500 to 800 m from the injection well with a bimodal distribution of depths. While the horizontal extent of the microseismic cloud was impressive, about 90% of the events were above the casing shoe, suggesting that injected fluid had leaked from the casing to stimulate relatively shallow and cool rock. After confirming that the casing did have a leak in 2013 the well was repaired at the beginning of the 2014 field season through a casing tie-back to the surface, isolating all casing problems observed in 2012.

In the fall of 2014, about 9500 m^3 (2.5 million gallons) of groundwater was injected during a total of 4 weeks of hydraulic stimulation. Wellhead pressures greater than 165 bar (2450 psi) were required to improve injectivity of the well, which was significantly higher than expected. A permanent injectivity improvement from 0.009 to 0.045 (L/s)/bar (0.01 to 0.05 gpm/psi) was achieved. However, much of the stimulation was run near the limits of the pumps, wellhead, surface piping, and permits, thus limiting the ability to further improve injectivity. During the 2014 stimulation, locations for 398 microseismic events were determined using the MSA installed in 2012. Event locations determined by different methods define an fracture network and potential EGS reservoir that extends at least 200 m (656 ft) from the wellbore. Microseismic event locations, well log data, and moment tensor solutions (Cladouhos et al. 2015b; AltaRock 2015) were used to design an optimal well path for a second well, NWG 55A-29, the producer in an EGS couplet (Figure A.33).

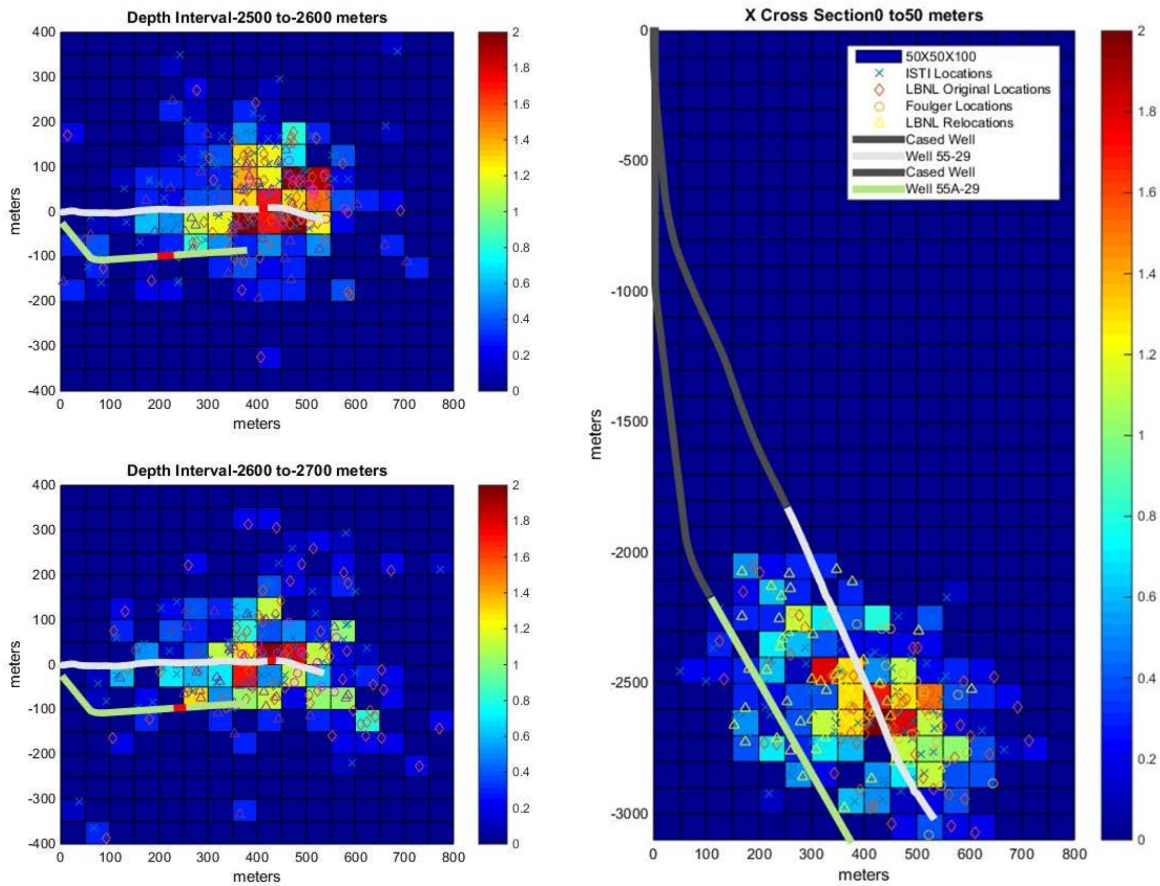

Figure A.33. Seismic density plot for NWG 55-29. Map at depth slices of 2400 **to** 2500 m (top left) 2700 to 2800 m (bottom left). Red sections of the proposed well path are well intersections with the depth slices. Cross section at 0 to 50 m south of the well (right). White path is stimulated well (NWG 55–29) and green path is producer (NWG 55A–29) planned during the final phase of NEGSD.

A.3.2 Implications of NEGSD Stimulation of Stress Magnitude Model

Based on an assumed stress model and numerical modeling (Cladouhos et al. 2011b), it was predicted that microseismicity and injectivity improvement would initiate at a WHP of 90 bar (1350 psi) and that pressures ranging from 130 to 150 bar (1950 to 2200 psi) would be sufficient to reach the required reservoir volume goal. The 2012 stimulation (Cladouhos et al. 2013a, 2013b) seemed to confirm this prediction with injectivity improvements and deep seismicity (>8000 ft, >2.4 km) initiating at a WHP of 93 bar (1360 psi) and four additional deep seismic events occurring at a WHP of 132 bar (1910 psi). Thus, the need to exceed 160 bar (2400 psi) WHP to promote stimulation in 2014 was unexpected. The practical effect is that the stimulation pumps reached their maximum pressure of 200 bar (2900 psi) on September 29, the sixth day of the stimulation. Surface equipment, shoe depth, and regulatory agreements also specified that the stimulation pressures be kept below 207 bar (3000 psi), so the pump performance was not the only limit preventing significantly higher pressures.

Figure A.34 shows the assumed stress and measured fluid pressure profiles in NWG 55-29. This figure shows that if tensile failure did not occur in the formation below the cemented shoe then the minimum principal stress gradient during the stimulation must have been greater than 0.86 psi/ft. That is, in the open hole, the dashed blue line, showing the measured fluid pressure gradient, is left of the solid blue line, showing a minimum principal stress gradient of 0.86 psi/ft. This is a much higher rock fracturing gradient, 0.7 psi/ft, than modeled prior to stimulation (Cladouhos et al. 2011b) and also higher (i.e., 0.6 to 0.65 psi/ft) than assumed during geothermal well drilling and testing in a normal faulting regime.[4]

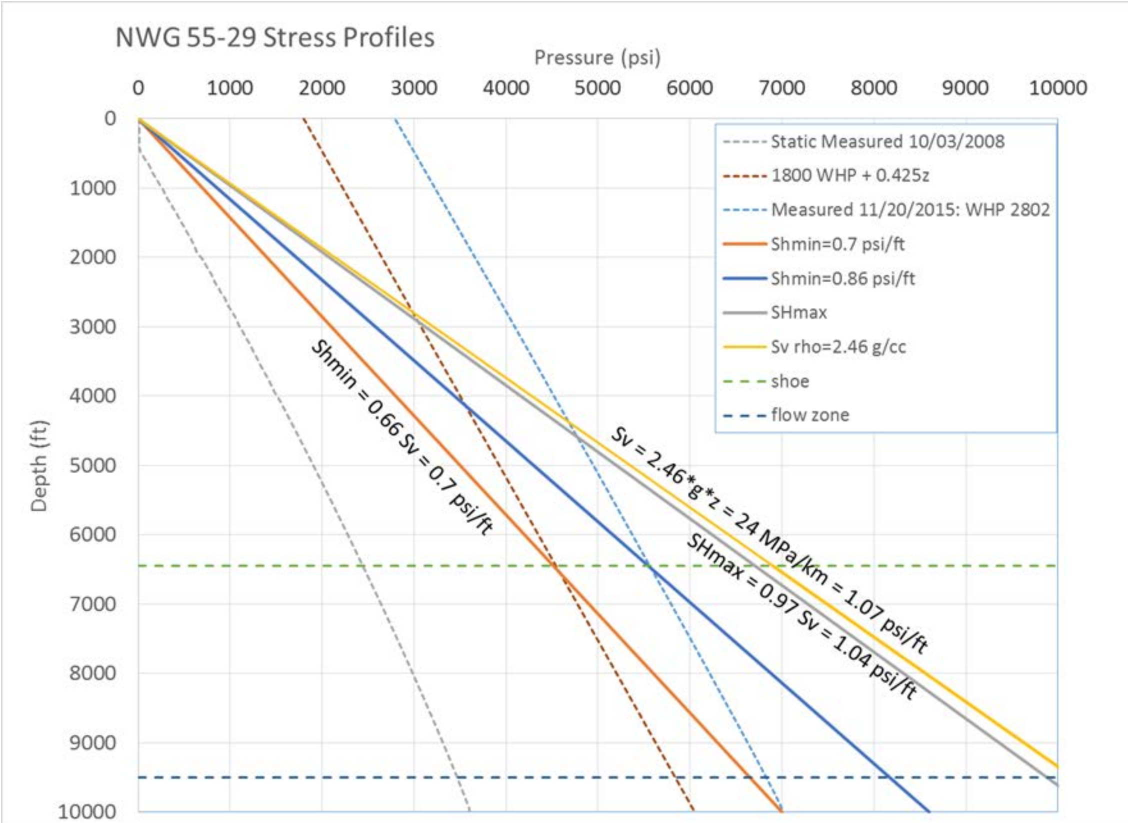

Figure A.34. Summary of measured downhole fluid pressures (subvertical dashed lines) and hypothesized stress profiles (solid lines). The open-hole interval is marked by horizontal dashed lines.

The high minimum principal stress gradient and thus high fluid pressures needed to initiate hydroshearing and enhance permeability are also reflected in the results of the 100 seismic moment tensors (AltaRock 2015). The moment tensors are consistent with horizontal compression over a wide azimuthal range, and relatively weaker vertical stress. Though this strain and apparent stress configuration derived from the microearthquakes is internally consistent, it is inconsistent with the local and regional strain field (Section A.2.4).

Possible factors for the inconsistency between predicted stress and stimulation results include:

1. Changes in stress regime with depth in NWG 55-29. The BHTV reached a depth of 2701 m (8860 ft) before failing due to high temperature. Most of the fluid loss zones before and after stimulation occurred below this depth. It is possible that a stress change below 2701 m accounts for both the change in well permeability and the inconsistency between a stress model derived from BHTV analysis and stimulation analysis.

[4] Lou Capuano, Jr., personal communications.

2. Heterogeneous stress regimes due to the location of 55-29 on the flank of a volcano. Volcanic features such as ring fractures, instrusives, magmatic pressure, the volcano's topography, and nested calderas may be responsible for a heterogeneous stress environment. The BHTV survey may have surveyed a block with consistent stress, but that block was not representative of the full stimulation volume as had been assumed.
3. The fluid injection itself significantly modified the stress field adjacent to the well in addition to simply raising pore fluid pressures.

Altarock (2015) concluded that the most likely explanation for the discrepancy between expected (pre-stimulation) stress magnitudes and orientations and those derived during the stimulation was due to the fluid injection itself (#3 above). In that case a production-injection well pair with a low pressure production well and a high-pressure injection well, would also modify the stress field in a complex way. Additional modeling during NEWGEN Phase 2B and stress data collection during NEWGEN Phase 2C will further investigate and model the stress regime at the NEWGEN site to better understand this apparent paradox.

Stress models have been a challenge at EGS projects in the past, starting at Fenton Hill (see recent re-analysis by Norbeck et al. 2016 and references therein). Even at conventional geothermal fields in extensional regimes (i.e., Dixie Valley, Hickman et al. 1999), the stress can be heterogeneous in a single well. While more data and analysis are needed to better understand the stress state at the NEWGEN site, this will be true of any future EGS site. At NEWGEN, a significant start has already been made toward characterizing the stress state needed to design a successful EGS. The field, analytical, and theoretical methods further developed and tested at NEWGEN FORGE to characterize stress, will be necessary and applicable at any potential EGS sites.

A.4 NEWGEN Conceptual Geologic Models: Methodologies, Results and Interpretation

The Conceptual Geologic Model for the NEWGEN FORGE site provides a unified framework in which to *identify the target reservoir units*, to constrain their *spatial extent*, and to characterize properties of relevance to EGS. Achieving a coherent view of conditions within the target reservoir units has involved synthesizing and coregistering multiple data sets with complementary sensitivity to one or more parameters of interest and, where possible, extending known values from well data by use of models derived from downhole and surface geological and geophysical data sets. The data sets and methodologies used to interpret them are described in detail in Section A.2. Here, the key sources of constraints on the specified EGS parameters are summarized.

The *temperature profile* within the target reservoir units is constrained by borehole equilibrium temperature measurements from deep wells (Section A.2.10.2) backed by thermal conductivity measurements of rock cores and cuttings (Section A.2.10.3), diffusive heat flow models (Section A.4.2), and coupled THMC models (Section A.4.1) that make use of *constraints on porosity and permeability* obtained from measured well data, bulk permeability data, and injectivity test data (Section A.2.10.4). Additional constraints on porosity and permeability also can be inferred from seismic (Section A.2.9.2) and magnetotelluric (Section A.2.9.3) models. *Fluid content* at the NEWGEN FORGE site is limited to a shallow aquifer or aquifers that extends to depth of 150 to 300 m below ground surface (Section A.2.7.1), beneath which increasing alteration of the volcanic minerals to clays, zeolites, and other moderate temperature minerals decreases permeability substantially to form a thick low-permeability zone, as observed on cores, well logs, mud logs and low electrical resistivity values (Section A.2.11). *Structural characteristics* have been defined by decades of geologic studies (Section A.2) as well as by recent high-resolution LiDAR mapping, by seismic tomographic and waveform modeling, and by magnetotelluric and gravity inversions. The site lithology and petrology have been defined by cores, well and mud logs, and surface sampling, and geophysical models provide a basis for interpolating between well-ties. The *stress regime* has been evaluated by regional seismic focal mechanism studies (Section A.2.4), by interpretation of faults and volcanic features aligned along structural controls, borehole breakouts, and the NEGSD stimulations.

Important constraints on the suitability of the NEWGEN site to serve as the FORGE were derived from the NEGSD project (Section A.3). The creation of a fracture network during a successful EGS stimulation, measurements of injectivity, extensive microseismic monitoring and measurements of induced seismicity, complementary surface geophysical data sets obtained during monitoring efforts, and comparisons between predicted stress and the mechanical response of the stimulation efforts have provided confirmation that conditions near NWG 55-29 meet FORGE requirements (summarized in Section A.3.2).

The Conceptual Geologic Model is intended to be a dynamic rather than static view of conditions in and surrounding the NEWGEN FORGE site. As a FORGE Phase 1 deliverable, it is intended to demonstrate the suitability of the site based on the characterization undertaken to date, but it also highlights areas of greater and lesser uncertainty, providing guidance for additional characterization work during Phase 2 of the FORGE project. As part of subsequent phases, fully coupled multi-physics/chemistry models will be developed for ongoing characterization and, ultimately, development of EGS process control methodologies. While development of new fully coupled models was not a component of FORGE Phase 1, the existing data inventory includes a fully coupled model and a thermal model that were outcomes of other projects at the Newberry site. These are described in the following sections.

A.4.1 Coupled Thermal-Hydrological-Mechanical-Chemical Model

A THMC model has been developed in two steps with the ultimate goal to capture both the local chemical and mechanical changes in the rock caused by the stimulation as well as the potential long-term response and sustainability of the larger-scale geothermal reservoir. A THMC model of the west flank of Newberry Volcano (Figure A.35) was created using THOUGHREAC. It encompasses the zone stimulated in 2012 and 2014 and a several kilometer region of the west flank from the surface down to the supercritical region, likely close to a postulated cooling intrusive body (Sonnenthal et al. 2012).

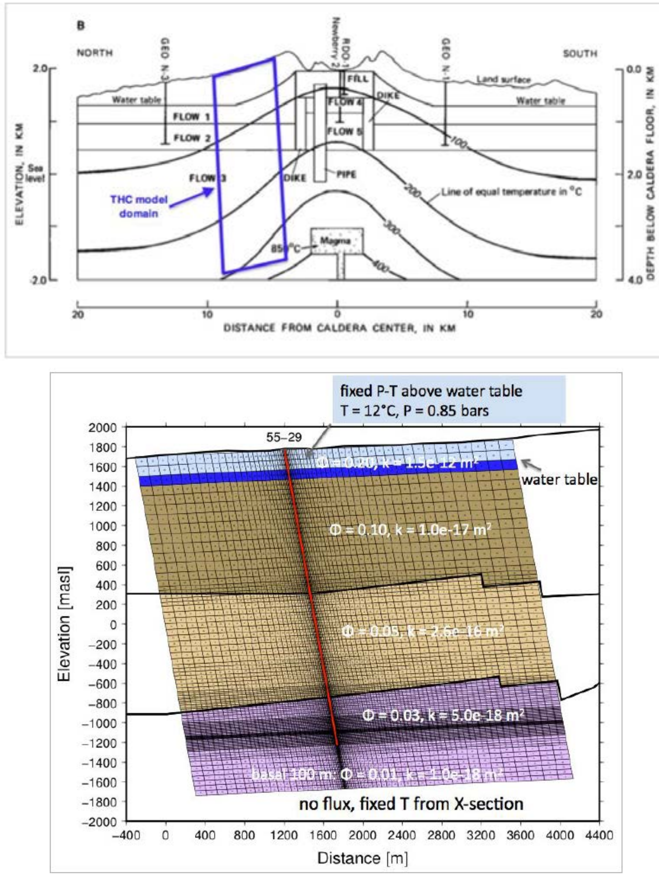

Figure A.35. Top: Location of the THMC domain (in blue) superimposed on east-west cross section from Sammel et al. (1988). Bottom: Equivalent numerical mesh showing hydrogeologic units, assigned porosity and permeability values, and thermal and hydrological boundary conditions.

To simulate the development of the observed hydrothermal mineralogy, the model used the pre-alteration mineralogy and shallow groundwater chemistry as the initial geochemical conditions, assuming that modeled temperature and pressure distributions were relatively constant over several thousand years. The close correspondence of modeled and observed epidote distributions support the observation that past hydrothermal activity took place under thermal gradients similar to current values, whereas calcite and sulfide abundances at depth likely require a magmatic gas component. Multicomponent geothermometry was used to estimate potential temperatures of equilibration of waters, and to evaluate the effects of kinetics on calculated mineral equilibration temperatures.

Based on this initial model, a 3D Thermal-Hydrological-Mechanical model was then developed by Sonnenthal and colleagues in 2015 using the TOUGHREACT-ROCMECH code (Kim et al. 2012, 2015). In addition to full multiphase reactive-transport capabilities, TOUGHREACT-ROCMECH also couples thermo-hydromechanical rock deformation (poroelasticity), shear and tensile failure, with coupling to porosity and permeability changes.

The Thermal-Hydrological-Mechanical model has captured the approximately fourfold increase in injection rates quite closely, as well as the spatial distribution of permeability increases and pressure changes due to the stimulation. The overall spatial distribution of microseismicity has been captured with an approximately 0.1 MPa increase over the hydrostatic pressure.

In addition to Thermal-Hydrological-Mechanical processes, mineral-water reactions and potentially THMC processes can affect the permeability of the fracture system. Even without significant changes in permeability, the geochemistry of waters and gases, provide valuable data for calibrating reservoir properties such as fracture surface area, porosity, and fracture-matrix interaction. The reaction extent also can be used to calibrate reactivities that can be used for long-term reservoir management simulations. Preliminary geochemical data from the 2014 stimulation flowback waters provide some insight into the water-rock reactions that have taken place over the short time period of the stimulation. Future work will include new data on fracture distributions, orientations, and stress conditions.

A.4.2 Thermal Model

Frone (2014, 2015) has proposed a thermal conductive model using a 2D finite-difference approach of the integrated response to past intrusive activity at Newberry Volcano. The exact intrusive history and geometry is unknown and is likely far too complex to be accurately resolved. In the model, a single large intrusion is thus used to represent the cumulative thermal energy input of many smaller intrusions.

Measured thermal conductivity values were used when possible (Blackwell 1994), otherwise lithologic averages were used (Figure A.36). A constant value of 0.85 kJ/(kg.K) was used for the specific heat capacity. The 50°C isotherm was determined from well data (cf. Section A.2.10.2). This isotherm produced a smoother boundary that mitigates the effects of the shallow cold water flow and was thus used to set the upper constant temperature boundary for the 2D model. The base of the model has a constant conductive regional heat flow input of 90 mW/m^2 for all model iterations (Blackwell and Richards 2004; Blackwell et al. 2011). The side boundaries of the model were reflective.

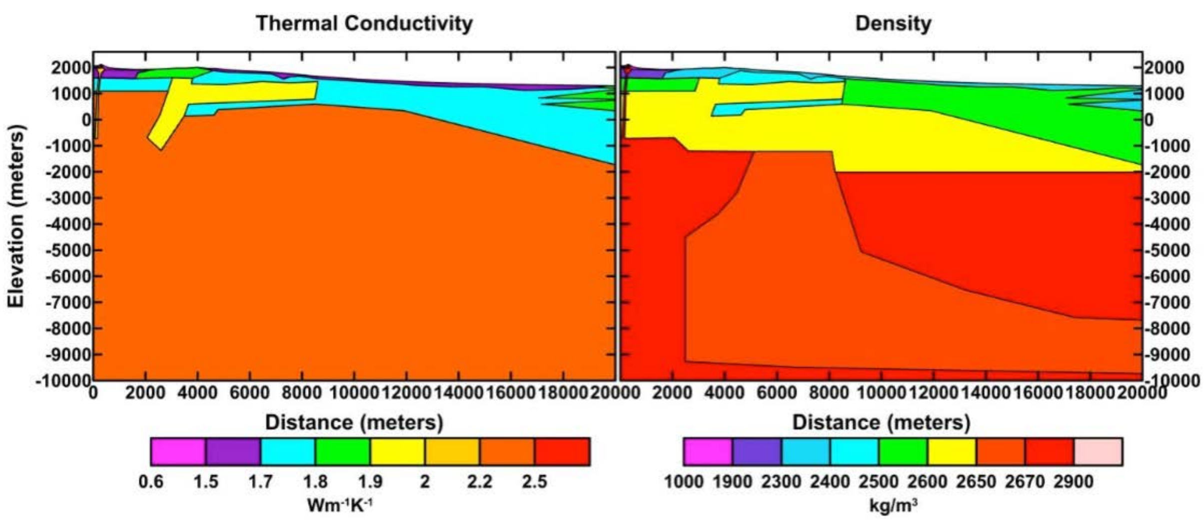

Figure A.36. 2D cross sections with thermal conductivities and densities used in the thermal model.

Tomography and waveform modeling have been used to constrain different sized magma bodies centered under the caldera (Beachly et al. 2012). The tomography results are consistent with a large hot-fractured pluton or a magma chamber on the order of ~60 km^3 in volume. Forward waveform modeling by Beachly et al. (2012) established a smaller, better constrained 1.6 to 8 km^3 magma body at a depth of 3 to 6 km.

The long-term thermal history of the volcano was modeled with the base of the magma body varying along with the other dimensions. A continuum from a single magma pulse to a constant magma body were calculated at 100,000-year intervals. For all model iterations, the total model duration was 500,000 years (the age of the volcano) and magma temperature was 1000°C. The intrusion temperature of 1000°C was used to represent a 750° to 850°C granitic intrusion with 150° to 250°C additional heat to approximate latent heat (30 to 50 cal/g). The best fit with well temperature data and tomography information is observed for a magma body with periodic recharge every 200,000 years, which corresponds the periodicity of the large caldera-forming eruptions at Newberry Volcano (Donnelly-Nolan et al. 2004). The top of this magma body would be at –3700 m and have a radius of about 8 km (Figure A.38).

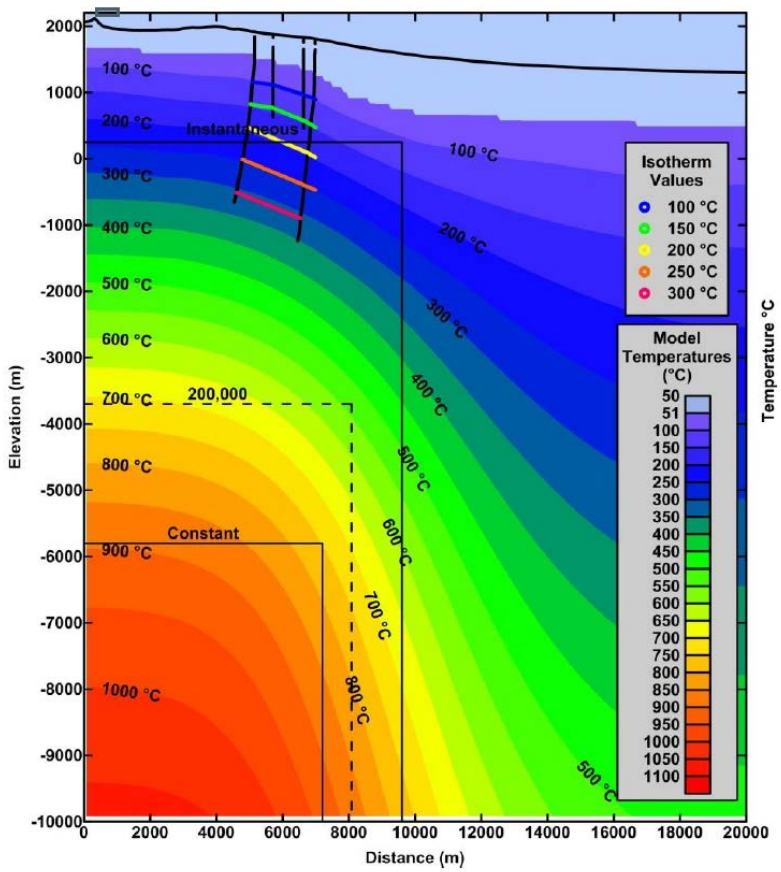

Figure A.37. Steady-state thermal model of the western half of the volcano along an east-west cross section of the volcano seen from the north. Locations of NWG and CE wells on west flank show as inclined black lines. The measured equilibrium temperatures in the wells were converted to isotherms, which are shown connecting the wells. Note the depression of the isotherms from east (left) to west (right). The boxes represent three different configurations of the magma chamber that fit the observed temperatures. The observed temperature isotherms and the wells used to generate them are shown. Solid black line at the top of the figure (at 2000 m) is the topographic surface. The background contour map is the final temperature field for the model with a 200,000-year recharge rate.

The total energy potential of the modeled magma body is nearly 175 EJ within the entire volume and ~80 EJ outside of the Newberry Volcanic Nation Monument above 250°C and shallower than 3.5 km. The total amount of energy used by the United States in 2012 has been estimated at ~100 EJ (EIA 2014), although it is not possible to produce and convert all of the heat at Newberry Volcano to useable energy at 100% efficiency, this number gives a good idea of the enormous amount of heat available at the volcano.

A.4.3 Representation in EarthVision

During FORGE Phase 1, a considerable volume and diversity of site characterization information has been assembled. NEWGEN has developed a coherent and self-consistent understanding of the target reservoir depth, temperature profile, thermal conductivity, fluid chemistry, permeability and porosity, structure and lithology of the target formation, regional and in situ stress directions, and extent of microseismicity, transmissivity, and impedance/injectivity. This process has guided the thinking about where there may be shortcomings in the existing data sets and models, and how they could be addressed during the next phase of the FORGE program. The assimilation and coregistration of such a diverse data set can be aided by applying toolsets developed for the resource exploration industry. For this purpose, EarthVision™, which is a software environment for 3D model building, analysis, and interpretation suitable for developing maps and cross sections, reservoir characterization, incorporating well-ties, and providing volumetric visualization and analysis, was used. Preliminary FORGE Phase I efforts to build a 3D visualization framework will continue to be refined throughout the lifetime of the NEWGEN FORGE project. The initial EarthVision reference models for Newberry Volcano were constructed as part of the NETL/OSU/Zonge project to monitor the EGS stimulation effort at NWG 55-29 (Mark-Moser et al. 2016), independent of the current FORGE effort. The EarthVision models provided by that project team have been further developed using new content from the FORGE Phase 1 project (particularly results from new 3D gravity and MT inversions), which results in the figures shown here.

Within this framework, the visualization and synthesis problem for Phase 1 of FORGE has been approached from two vantage points. First, a geophysical 3D data volume is presented in EarthVision (Figure A.38 and Figure A.39 in Section A.4.3.1), in which each object within the geophysical volume represents a different geophysically derived data layer (e.g., a feature identified from its electrical resistivity, seismic P-wave velocity, density derived from 3D inversion gravity inversion, etc.). Second, a geological 3D data volume is presented in EarthVision (Figure A.40 and Figure A.41 in Section A.4.3.1), in which each object represents a geological observation (e.g., a constraint on lithology from well cores and cuttings, surface expressions of faults, cinder cone alignments, etc). The ultimate goal is to merge the geophysical and geological data volumes into an EGS parameter visualization volume that would delineate the parameters most directly governing EGS potential (e.g., permeability, stress field, injectivity, etc.). While these parameters and their uncertainties are quantified in Section A.5, at present the EarthVision models are organized into distinct geological and geophysical parameter sets that were used during FORGE Phase 1 to co-register and compare constraints on formation extent and characteristics. During the proposed Phase 2 of FORGE, the derived parameters in Section A.5 would be refined and incorporated into this 3D visualization environment.

A note on the display of uncertainties in EarthVision: At the current FORGE Phase 1 stage, the EarthVision model is conceptual (i.e., qualitative rather than quantitative, in line with the FORGE Phase 1 goal of developing a Conceptual Geologic Model). Therefore the visualizations provided below represent conceptual data layers rather than rigidly constrained geologic layers. They are interpretations based on the current state of knowledge. Most importantly, the visualizations do not display the uncertainties in the various parameters that are subsequently discussed in Section A.5. On the contrary; in the absence of constraining information, the assumption in the visualizations displayed below is that layer horizons are continuous and extend to the outer boundaries of the model in the horizontal direction. The limitations of this assumption become evident, because there are relatively few constraints on subsurface conditions on the eastern half of the volcano. Fortunately, the data density in and surrounding the NEWGEN FORGE site on the western flank of the volcano is high, so this artifact of the present state of the visualizations is less of an issue in the area of greatest significance to FORGE.

The qualitative, and where available, the quantitative and/or probabilistic uncertainties in the parameters of relevance are described in Section A.5. During the proposed Phase 2 of FORGE, the EarthVision model will continue to be developed as new data sets are acquired and parameter uncertainties are refined so the conceptual aspects of the geologic model will be transformed into quantitative ones; those uncertainties will propagate into the EarthVision visualizations as well.

A.4.3.1 Major Geophysically Delineated Units

Figure A.38 displays the major units identified from geophysical signatures as follows:

a. Intrusive bodies. Caldera ring fractures displayed here coincide with mapped surface ring faults, extended here to a maximum depth of ~3 km and with a lateral thickness to match seismic tomography (Beachly et al. 2012) and also on the west flank the electrically conductive zone present beneath the ring fault in the OSU 3-D MT model. The seismic P-wave anomalies are indicated (fast, slow) by tomography and waveform modeling (Beachly et al. 2012). The gravity high at the west flank (Waibel et al. 2015, and the present NEWGEN study) coincides with the tomographically inferred intrusive zone.

b. Same as (a) but an isosurface of 5.5 km/s P-wave velocity (from Beachly et al. 2012), is inferred to correspond to the zone of increased rock competence.

c. Same as (b) but with the horizon above the seismically competent layer defined by MT data to be associated with increased chlorite and potentially epidote alteration (Waibel et al. 2015. Atop this is an electrically more conductive zone (note the gap at the western flank) whose top surface is inferred to represent the 150ºC isotherm, a zone of decreased smectite alteration (Waibel et al. 2015).

d. Same as (c) but transient electromagnetic sounding results define the zone of progressive smectite alteration (Fitterman 1988) above which lie surface deposits (not well resolved from existing geophysics), and thick caldera fill, which is resolved by seismic tomography (Beachly et al. 2012) and MT (Waibel et al. 2015 and the present NEWGEN study).

e. Perspective view of major geophysically detected units with the zone of increased chlorite and epidote removed to show internal units.

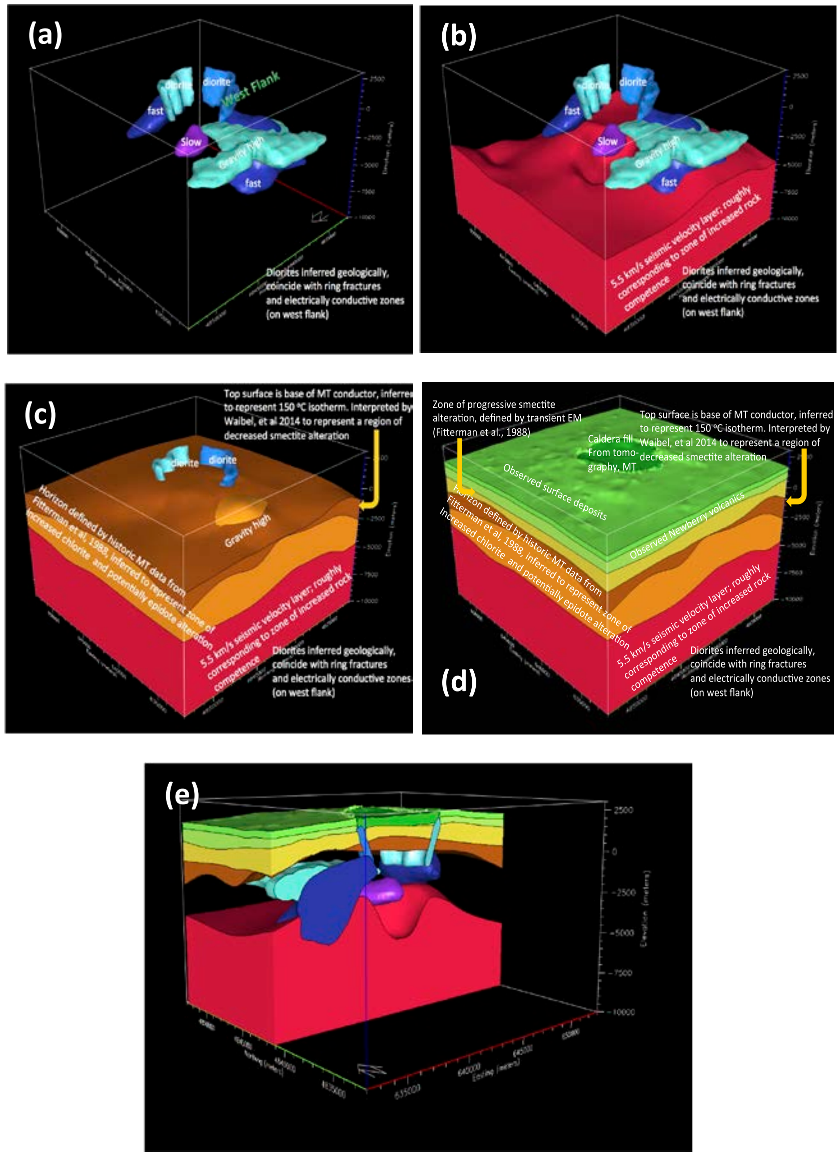

Figure A.38. Representative geophysical data layers displayed in EarthVision viewed from northwest looking toward southeast (western flank/NEWGEN FORGE site on the right-hand side).

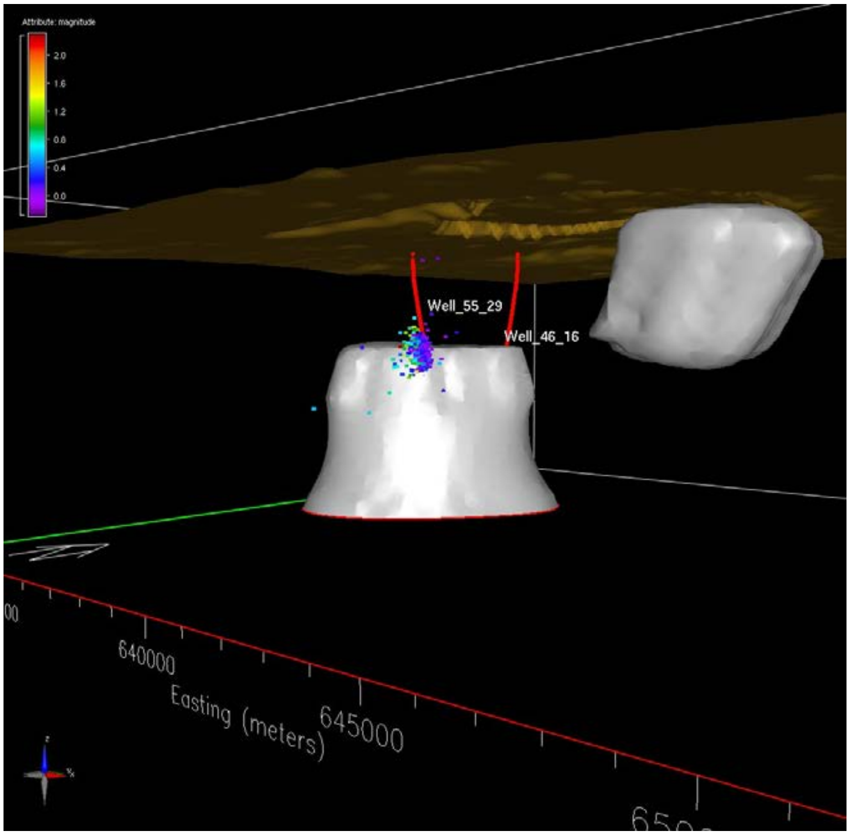

Figure A.39. Two main geophysical units defined by density from 3D gravity inversion (from present study) showing two wells NWG 55-29 and NGW 46-16 with the cluster of microseisms from the 2014 NEGSD stimulation displayed. The view is westward looking and the Newberry Volcano caldera can be seen from below in the topographical layer colored in dark yellow.

Figure A.39 displays the results of this project's 3D gravity inversion with the locations of seismic events superimposed. The "West Flank Intrusive" is in the center, as identified in Table A.5 (density 2.66 g/cm^3; 0.16 gm/cm^3 above surrounding formation density). The "Ring East" unit from Table A.5 is displayed on the right (density 2.54 gm/cm^3; 0.14 gm/cm^3 above surrounding formation density). The colored dots are the microseism locations from the 2014 deep EGS stimulation.

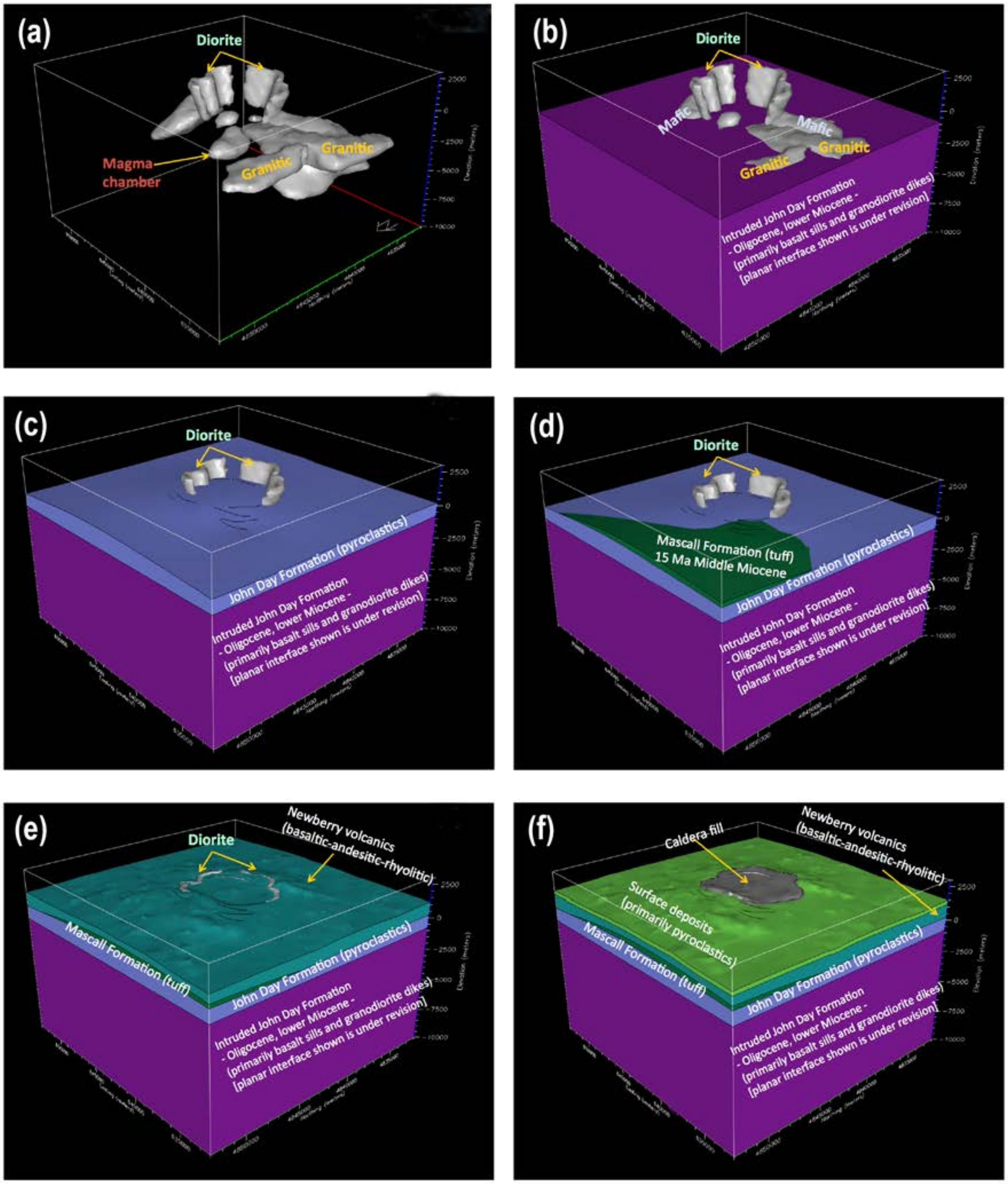

Figure A.40. Geological data layer showing intrusive bodies mapped at the surface or identified through well cores and mud logs, with areas at depth between wells interpolated by assigning bulk petrologic classifications to geophysically defined intrusive bodies. Geologic formations mapped from cross sections have been overlain on the intrusive bodies.

Note that the cluster of microseisms from the 2014 EGS stimulation at NWG 55-29 appears to conform approximately to the boundary of the West Flank Intrusive. This is seen in the gravity inversion (Figure A.23). The West Flank Intrusive's northern and eastern boundaries approximately overlap the region of higher resistivity at depth beneath the west flank, as delineated by the OSU 3D resistivity model (Figure A.21). The possibility that the eastern boundary of the gravity and the MT anomalies that we associate with this intrusive body could be an artifact of sparser data coverage proximal to the western rim of the caldera and interior to the east of the NEWGEN FORGE site has been considered. While the spatial resolving power of both MT and gravity methods will be lower toward and inside of the caldera because of the sparser sampling there, stations to the immediate east of the FORGE site are sufficient to delineate the eastern boundary of both density and resistivity anomalies; consequently. This is not taken to be an artifact of station coverage, but a deep structural boundary. Whether the clustering of microseisms along this intrusive body's boundary is coincidental to the location of NWG 55-29, or reflects a physical constraint on the local stress field will require additional site characterization and modeling to determine.

Figure A.40 displays visualizations of the major formations inferred from geological data. In the figure, (a) shows the major intrusive bodies identified from existing surface maps, geologic cross sections, and well lithology. The large-scale lateral continuity of the formations identified in this figure is an artifact of the visualization method employed; in areas distant from wells described in Section A.2.10 (see Figure A.7 for well locations), continuity of formations is not stratigraphically constrained. This is discussed in more detail below.

Please note that the bodies labeled as "granitic" for convenience are not interpreted to be uniformly granitic, but zones where microcrystalline granodiorite dikes are interbedded with basalt and basalt-basaltic andesite, as directly sampled in cores from NWG 55-29. In the figure, (b) is the same as (a) but with the Intruded John Day formation overlayed on intrusive bodies. The bottom of this formation is not defined in this model, so for convenience it has been extended to the base of this visualization volume. (c) is the same as (b) but with the John Day Formation on top of the Intruded John Day formation. (d) is the same as (c) but with the Mascall Formation on top of the John Day Formation. (e) is the same as (d) but with an overlay of the Newberry volcanics sequences. (f) is the same as (e) but with surface pyroclastics.

A.4.3.2 Stratigraphic Continuity

Waibel et al. (2015) examined the issue of lithologic correlations between wells and the continuity of formations at Newberry Volcano. By comparing the geochemical analyses of previously collected local and regional surface rocks with subsurface rock samples from Newberry Volcano, and also by factoring in gamma ray logs, cutting notes, and general stratigraphic relations, Waibel et al. determined a similarity coefficient for each pair of samples, which represents the average of elemental concentration ratios between each sample pair.

Four similarity coefficients were calculated for each sample pair; one for the major element compounds, one for trace elements, another for rare Earth elements, and a combined value for all elements analyzed. The correlation between the composition of each member of a rock sample pair was determined from the similarity coefficients. Waibel et al. (2015) determined that the data sets with the highest compositional correlations were the cuttings of NWG 55-29 and the cores from temperature gradient hole N-2.The wellhead for N-2 is located 370 m east of the wellhead of for NWG 55-29, while at ~1200 m depth, they are separated by ~200 m. Waibel et al. concluded that the gamma ray logs were uncorrelated, whereas the chemical composition correlations were much stronger. Even so, there is not a consistent dip of thickness of the chemically correlated units between the two wells. The correlation between lithologies at 55-29 and N-2 is seen in Figure A.41. This reveals that N-2 contains proportionally more basaltic lava flows and distinct interbedded silicic units than NWG 55-29. NWG 55-29 has less defined lava flows and more interbedded debris flows between thinner basalt flows.

Waibel et al. (2015) examined lithologic correlations between other well pairs, but the most relevant to the NEWGEN FORGE site is that of 55-29 and N-2 (Figure A.42), and also 55-29 and 46-16 at the northeastern edge of the FORGE site. As with N-2, there was little correlation between the gamma ray logs between 55-29 and 46-16, but the chemical composition shows similarity between a thick silicic (silica ~73wt %) zone in 46-16 between –450 m and –875 m (7800 to 9200 ft TVD) and distinct silicic zones in 55-29 around –475 m, –725 m, and –800 m that appears to be a metamorphosed tuff unit with chlorite and trace euhedral pyrite as an alteration mineral within the tuff. A less silicic (silica 67 wt%) zone between –1000 m and –1240 m (9,500 to 10,400 ft TVD) in 46-16 and –925 m and –1200 m (8900 to 9800 ft TVD) in 55-29 are also compositionally correlated. Between these two correlated units there is a thin (<10 m) andesite unit. Above these zones is another basaltic andesite that is correlated between the two wells. An intrusive micro-granodiorite intersected in the final 15 m of 55-29 may be correlated with zones in 46-16 at –1325 m, –1450 m, and –1500 m, although this is based solely on the gamma logs. The deep micro-granodiorite sampled in Well NWG 55-29 is chemically similar to a glass, and a rhyolite flow in samples from 1390 m and 1355 m (1290 ft and 1400 ft TVD) in 55-29 and may represent the intrusive equivalent of an erupted rhyolite flow.

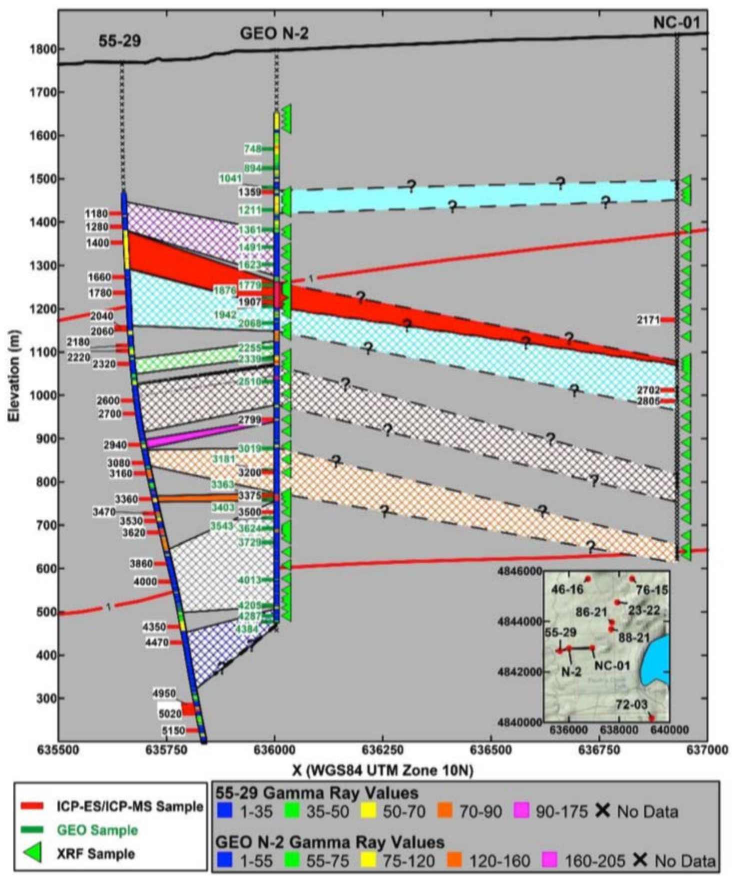

Figure A.41. Well traces colored by gamma ray log values for NWG 55-29 and GEO N-2; NC-01 does not have an available gamma ray log. Symbols show the location and depth of geochemical samples; label values refer to measured depth in feet. Colored boxes represent correlated lithologies, cross hatched lithologies are mafic, and solid boxes are silicic. The solid black line at the top is the topographic surface and the solid red lines show the upper and lower surfaces of the 10 Ω·m conductor from the Waibel et al. (2015) MT survey. X-axis units are Universal Transverse Mercator locations along the cross section. Inset map shows the location of the cross section in relation to other west flank wells. (Source: Waibel et al. 2015)

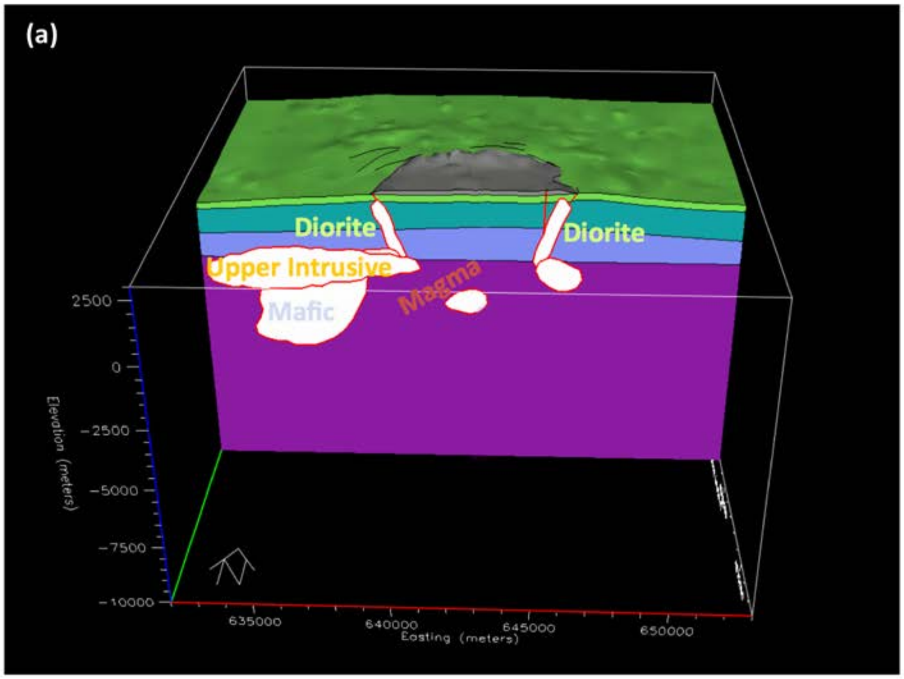

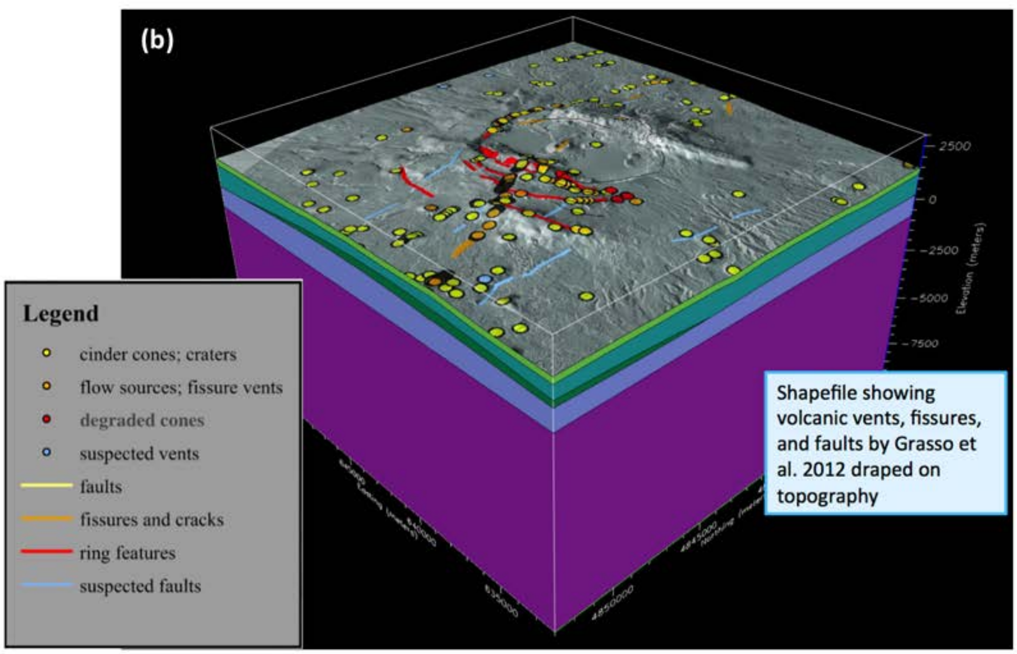

Figure A.42. a) West-to-east cross section through geologic data volume as displayed in EarthVision. b) Overlay of high-resolution LiDAR surface topography with faults and volcanic features indicated.

A.5 NEWGEN Parameter Summary and Uncertainty

Table A.12 summarizes critical NEWGEN parameters for the target reservoir depth that are discussed in the ensuing sections.

Table A.12. Summary of critical NEWGEN parameters for target reservoir depth.

PARAMETER	AVERAGE VALUE	UNCERTAINTY	BASIS FOR UNCERTAINTY
Extent of target reservoir rock unit	9.4 km^2 (2340 acres) and 4.1 km^3 volume based on temperature 38 km^2 (9400 acres) 77 km^2 (19,120 acres) (Section A.5.11 and A.5.1.2)		2340 acres are the sub-surface area accessible from three existing pads assuming up to 1000 m of directional drilling. 9400 acres are the NEWGEN FORGE area. 19,120 acres in Newberry Geothermal Unit
Structure and lithology of target formation, includes petrology	Chloritized tuffs and volcanic sequence (granodiorite with average thickness of 29 m or felsic with average thickness 9 m dikes or sills with alternative subvolcanic basalts to depth) (Section A.5.1.3)		Lithology at NEWGEN FORGE Site based on drill cuttings from Wells NWG 55-29 and 46-16 and core from core hole GEO N-2; detailed petrologic and mechanical analyses performed on samples Granodiorite is present at depth in Well NWG 55-29, while extrusive andesite is located at depth in core hole GEO N-2 Structure defined by decades of geologic studies (Section A.2) as well as by recent high-resolution LiDAR mapping, by seismic tomographic and waveform modeling, and by magnetotelluric and gravity inversions.
Target reservoir depth and temperature profile	1750 TO 2250 m depth 175-225 °C between 1750 m and 2250 m depth (Section A.5.1.2)	0.01 m °C (measurement errors for both)	Temperatures at the target reservoir depth are based on measurements in wells at the NEWGEN FORGE Site, so uncertainty is low.

Table A.12. (contd)

PARAMETER	AVERAGE VALUE	UNCERTAINTY	BASIS FOR UNCERTAINTY
Thermal conductivity	1.93 to 1.95 W/(m.K) in NWG 55-29 in Table A.6 (also Section A.5.1.4)	0.21 W/(m.K)	Direct measurements on core samples and cuttings (Blackwell 1994; Frone 2015).
Fluid content and chemistry	Negligible (Section A.5.1.5)	NA	Fluid content of target rock formation established during flow tests in three different wells at and in close proximity to the NEWGEN FORGE site; once injected water boiled and flowed out, no existing formation fluids were available to replace the injected water
Permeability and porosity of target formation	Average bulk permeability of 2.6 10^{-16} m^2 Porosity of 5 to 6.4% (Section A.5.1.6)		The injectivity during well tests showed low formation permeability; permeability and porosity measurements made on cores from Well GEO N-2 in close proximity to the NEWGEN FORGE site
Geophysical surveys	Seismic Tomography Magnetotelluric Microgravity Borehole Geophysics Fiber-Optic Distributed Temperature Sensing (Section A.5.1.7)	Uncertainty varies from method to method. A rigorous uncertainty analysis and propagation of errors will be performed in the next generation of the geologic model.	
Regional and in situ stresses, includes regional stresses, in situ stress directions	Normal faulting stress regime with S_{hmin} oriented approximately east to west (Section A.3.2) Local stress at NWG 55-29: Sv = 24.1 MPa/km SHmax = 23.5 MPa/km Shmin = 14.9 - 15.8 MPa/km (Section A.5.1.8)		Focal mechanisms from earthquakes >M 4.0. Breakouts observed by BHTV at NWG 55-29

Table A.12. (contd)

PARAMETER	AVERAGE VALUE	UNCERTAINTY	BASIS FOR UNCERTAINTY
Seismicity – Extent of micro seismicity, transmissivity, and impedance	None greater than M_L 5.0 (Richter magnitude) within 100 km; None within 10 km of the site No local recorded micro seismic events with M>0.5 monitored 2010-2012 (Section A.5.1.10)		Observations of the regional seismic network PNSN

A.5.1 Parameters Summary

A.5.1.1 Extent of Target Reservoir Unit

As indicated in Section A.2.6.1, individual formation identification is of only marginal interest for our purposes; the composition of the rocks is more important with respect to the tendency to fracture. Given that the temperature profile below the shallow aquifer is governed by conductive heat transport, the thermal conductivity of the rocks, as well as other material properties also defines the target reservoir. These qualities are not tied to specific formations.

The NEWGEN FORGE site is a contiguous subset of the Davenport Newberry Geothermal Unit on the western flank of Newberry Volcano, as indicated in Figure A.27. The area of the NEWGEN FORGE site (the boundaries are marked in yellow in the figure) encompasses ~40 km^2 (≃15 mi^2 [≃9400 ac]). While this entire area is available for operations (such as noninvasive geophysical characterization that may require observations over a wide spatial aperture that extends beyond the NEWGEN FORGE zone), the surface footprint of the NEWGEN FORGE site for testing EGS (pads, wellheads, and supporting infrastructure) is the area of 5 acre each of Pads 17, 16, and 29 (see Figure A.7). From each of these pads, directional drilling could easily access the subsurface formation up to 1000 m from the surface location of the drill rig; that is a subsurface area of 3.14 km^2 (780 acres). The subsurface area accessible from the three pads covers 25% of the total NEWGEN FORGE operating area, encompassing ~9.4 km^2 (≃2340 ac).

Identification of the target reservoir volume within the NEWGEN FORGE site (rather than the more classically defined target reservoir unit) depends on identification of a contiguous subsurface zone where temperatures of 175ºC to 225ºC are reached between depths of 1.5 and 4.0 km, concurrently with permeability of order 10^{-16} m^2. Among other requirements, the target reservoir volume must contain brittle rock suitable for EGS stimulation under the prevailing stress regime. We consider each of these requirements in turn as we place bounds on the extent of and uncertainty of the target reservoir volume.

A.5.1.2 Temperature

At NWG 55-29, the full span of FORGE target temperatures of 175ºC to 225ºC are reached at depths from 1472 m to 1892 m. This depth range is contained in a basaltic andesite-basalt unit bounded on the bottom by a welded lithic tuff, both within the John Day Formation (Figure A.8).

At NWG 46-16 (the northeast NEWGEN FORGE pad), the full FORGE target temperature range is projected to be reached at depths from 1752 m to 2182 m. This depth range is contained within tuff + debris flow + andesite, rhyolitic tuff, and tuff + andesite units of the Mascall Formation (Figure A.9). A well bridge event that clogged NWG 46-16 below ~1432 m depth precluded equilibrium temperature measurements at target formation depths, but point extrapolation of a nonequilibrium series of temperature logs as well as continuation of the conductive temperature gradient in the upper part of the well yields the values cited above.

Frone et al. (2014) applied a numerical 2D time-dependent finite-difference heat flow model of the western flank to match observed downhole equilibrium temperatures (Figure A.25). The locations of the wells are shown in Figure A.7 and the 2D thermal model in Figure A.37. Wellbore lithology, seismic tomography, and 3D MT were used to constrain the structure, which resulted in the thermal conductivity profile seen in Figure A.36. Within the scale-length of the NEWGEN FORGE site, Frone's 2D density profile (Figure A.36), compares reasonably well with the present NEWGEN study's 3D gravity model (Figure A.23). The extension to using 2D averaged thermal conductivities also seems reasonable on this basis.

The N-NE profile connecting NWG 55-29 to NWG 46-16 defines the western edge of measured downhole temperatures. All downhole equilibrium temperature measurements lie on or east of this line. On and east of this line, the fit of Frone et al.'s (2014) model to observed temperatures at the other well sites on the west flank provides confidence that the conductive heat flow regime holds throughout that area. To the west of this line, because there are no direct downhole equilibrium temperature measurements, other observations have to be taken into account. Examination of the NEWGEN 3D MT study results shows no significant lateral variations in electrical resistivity at depths of 1400 to 2500 m below the surface of the NEWGEN FORGE site. Variations in resistivity would be expected if a significant quantity of interconnected interstitial fluids or secondary reaction products were contained within the rock matrix, or if there were strong temperature anomalies or significant compositional transitions. The absence of these within the NEWGEN FORGE site is suggested by the uniform resistivity structure within this area, at least within the MT data set's lateral resolving power of several hundreds of meters.

At Pad 17, 2 km west of NWG 46-16, there are no deep temperature measurements. The westward dip to the isotherms in the Frone et al. (2014) model depresses the isothermal surfaces by ~500 m at Pad 17 relative to those at NWG 46-16, deepening the projected target reservoir volume in the northwest section of the NEWGEN FORGE site well Pad 17) to ~2252 m to 2682 m. This depth range is projected to be contained within the John Day Formation (Figure A.8), but no well has been drilled at that pad to confirm the lithology or temperature.

On thermal grounds, the target formation volume is therefore contained within depths of ~1472 m (shallowest at NWG 55-29) to ~2682 (deepest at well Pad 17), providing the full FORGE temperature range of 175 to 225°C. Here we assume that the thermally defined target formation volume spans (but is not limited to) a 1000 m radius around each of the potential NEWGEN FORGE drilling sites; therefore, 3.14 km^2 (780 acres) per pad and 9.4 km^2 (2340 acres) total. The thickness of the target formation volume is ~420 m to 450 m throughout that area. Taking an average value of 435 m formation volume thickness, and the NEWGEN FORGE surface area of 9.4 km^2, the total target formation volume is 4.1 km^3.

A.5.1.3 Lithology

The structure and lithology of the target formation comes directly from drilling at the NEWGEN FORGE site. Subsurface conditions encountered at NWG 55-29 and NWG 46-16 provide direct evidence of the lithology and petrology of the target formation. The lithologies below Pad 29, described from 3 m (10 ft) interval drill cuttings from NWG 55-29, include a wide variety of volcanic, volcanoclastic, and hypabyssal units, ranging from ash flows and debris flows, to silicic domes, mafic flows, and mafic, granodiorite, and felsic dikes (Epoch 2008a), as previously described in Section A.2.11. The target formation exists in a chloritized volcanic sequence (tuffs, basalts, andesites, rare felsic dikes) found between depths 1722 and 2627 m (5650 and 8620 ft).

NWG 55-29 was drilled in an area of the western flank away from any surface expressions of the caldera ring fractures. LiDAR analysis of the mapped ring fractures northeast of Pad 29 reveals curved vent fissures and tentatively correlated vent alignments that end more than 3 km (1.9 mi) from the pad. Dip-slip fault offset along the ring fractures was not observed in the LiDAR surfaces. Pad 29 is located on the edge of a gravity high anomaly identified by Gettings and Griscom (1988) and confirmed by the present study (cf. Section A.2.9.4). The open-hole interval of Well NWG 55-29 extends between 1903 to 3066 m (6,242 to 10,060 ft) TMD. The well first intersects microcrystalline granodiorite at a measured depth of 2627 m (8620 ft). This is the first of 12 granodiorite (average thickness 29 m) or felsic (average thickness 9 m) dikes or sills with alternating subvolcanic basalts to total depth.

A.5.1.4 Thermal Conductivity

Thermal conductivity measurements on 94 rock cores (Wells N-1, N-2, N-3, N-4, N-5, NC-01, and 72-03) were compiled from Blackwell (1994). In addition, measurements on cuttings from CE 23-22 (46 samples), NWG 46-16 (9), and NWG 55-29 (14) were completed by Frone (2015). These results show a range of 1.53 to 2.23 W/(m.K) for all cores and a range of 1.93 to 1.95 W/(m.K) for the target depth in NWG 55-29.

A.5.1.5 Fluid Content

The fluid content of the target formation appears to be negligible. In attempts to flow test wells, injected water boiled, flowed out of the well, and then quickly ran dry because there were no formation fluids to replace the boiling water (Section A.2.10.4). Well NWG 55-29 was flow tested and only released small amounts of water and noncondensable gases that had accumulated in the wellbore. At the end of the test, CO_2 gas readings were in excess of 30,000 ppm without air assist. A later injection test gave no indication that the formation was capable of accepting injection water at a surface pressure of 6.7 MPa (970 psig). Test results for all of the wells at and near the NEWGEN FORGE site demonstrated injectivities several orders of magnitude lower than the lowest permeability of typical geothermal producers—geothermal well injectivities typically range between 1.8 and 1800 kg/s-bar (1 and 1000 kph/psi)(Spielman and Finger 1998).

A.5.1.6 Porosity and Permeability

The average porosity measured on core samples in Well GEO-N2 (the closest to NEWGEN FORGE site) is 5.3 % (see Table D.7 in Appendix D). The permeability measured in only two of the samples at present, GEO N-2 4219.5 2H and GEO N-2 4281 3V, are 2.96 10^{-22} m^2 and 7.4 10^{-21} m^2, respectively, which is an initial indication of more vertical permeability than horizontal permeability. From 2010 to 2014, several well tests and model runs were performed on NWG 55-29 as part of the NEGSD (AltaRock 2015). An initial permeability 1×10^{-17} m^2 was used, consistent with native state modeling and limited measurements. Test results for all of the wells found injectivities (Table A.7) several orders of magnitude lower than the lowest permeability of typical geothermal producers. Bulk permeability for CE 23-22 was determined to be 2.6×10^{-16} m^2 (Spielman and Finger 1998).

A.5.1.7 Geophysics

The various geophysical methods employed on the NEWGEN FORGE site are detailed in Section A.2.9 and their integration in the Geological Model with discussion of the uncertainties are presented in Section A.4.3. In addition high-resolution induction, spectral density, dual-spaced neutron, temperature, natural gamma ray, and caliper logs were obtained in NWG 55-29 by Halliburton during the drilling operation in the summer of 2008 using their high-temperature, high-pressure, hostile slimhole logging suite. In addition to the open-hole log suite, both static and injecting PT surveys were conducted after drilling operations. Further PT surveys conducted during the NEGSD project in 2010 and 2014 used fiber-optic distributed temperature sensing systems to track hydraulic stimulation. The Sandia BHTV was run in October 2010 as part of the NEGSD using a logging truck from the USGS in Menlo Park, California, to produce an image log revealing the orientation of fractures in NWG 55-29.

A.5.1.8 Regional Stress

South of Newberry, Crider (2001) using focal mechanisms from earthquakes >M 4.0, obtained a stress tensor with 1) the least compressive stress sub-horizontal ($S_{hmin} = \sigma_3$) and oriented east to west or slightly east-northeast to west-southwest (264°±29°), 2) the greatest compressive stress near vertical ($S_V = \sigma_1$), and 3) the intermediate stress approximately north to south ($S_{hmax} = \sigma_2$). Furthermore, other geologic stress indicators in LiDAR imagery, including dikes, cinder cones, and normal faults, yield stress directions within and adjacent to the proposed FORGE location that are consistent with those results (Cladouhos et al. 2011b). The offset and attitude of these features suggest a normal faulting stress regime with roughly east-to-west extension. The fault scarps show only minor variation in strike, suggesting that these structures reflect the geologically recent direction of the least compressive principal stress, S_{hmin}, around Pad 17. In a normal faulting stress regime with S_{hmin} oriented approximately east to west, an EGS reservoir is expected to grow in a north-to-south direction due to activation of steeply dipping fractures as seen in similar stress regimes (e.g., Heffer 2002; Cornet et al. 2007). This conclusion was supported by the analysis of BHTV data acquired in NWG 55-29 (Figure A.29), and the propagation of microseismic events recorded during stimulation activities at the NEGSD project site.

A.5.1.9 Local Stress Field

The borehole breakouts seen in the BHTV at NWG 55-29 showed a consistent azimuth indicating that the minimum horizontal stress, S_{hmin}, is oriented at 092 ±16.6° (Figure A.29) relative to true north (Davatzes and Hickman 2011). This azimuth of S_{hmin}, in combination with the attitude of the majority of natural fractures revealed in the image log, also is consistent with normal faulting. The consistency of the breakout azimuth, without localized rotations, taken in combination with the extremely low rate of seismicity in the region and the weak expression of natural fractures in the image log, suggests that there has been little recent or active slip on fractures in the vicinity of the well (Davatzes and Hickman 2011; Cladouhos et al. 2011a).

The NEGSD experiment at NWG 55-29 showed that the minimum principal stress gradient during the stimulation must have been greater than 0.86 psi/ft (Section A.3.2). This high minimum principal stress gradient and thus high fluid pressures needed to initiate hydroshearing and enhance permeability also are reflected in the results of the 100 seismic moment tensors (AltaRock 2015). The moment tensors are consistent with horizontal compression over a wide azimuthal range, and relatively weaker vertical stress. Though this strain and apparent stress configuration derived from the microearthquakes is internally consistent, it is inconsistent with the local and regional stress field (Section A.2.4).

The experience during NEGSD at NWG 55-29 highlights the importance of performing tests designed to measure stress magnitudes (i.e., mini-fracs) during drilling. Any wells drilled as part of the NEWGEN FORGE project will include stress measurements at multiple depths.

A.5.1.10 Seismicity

Historic earthquake data demonstrate that Newberry Volcano is essentially aseismic (Wong et al. 2000). No earthquakes greater than M_L 5.0 (Richter magnitude) are known to have occurred within 100 km (62 mi) before 1980. Since the expansion of the PNSN into Oregon in 1980, only six $M_L \geq 3.0$ earthquakes have been detected within 100 km (62 mi), most in a single 1999 swarm located 98 km (61 mi) to the southeast. No earthquakes have ever been located within 10 km (6 mi) of the proposed FORGE location. Four microseismic events ($M_L \leq 2.2$) were recorded 10 to 15 km (6 to 9 mi) from NWG 55-29 in 2004 and 2005 at depths between 4 and 8 km (2.5 to 5 mi). Monitoring of natural microseismicity between 2010 and 2012 using a seven station surface MSA did not detect any local events with M >0.5.

A.5.2 Preliminary Analyses for Quantifying Uncertainties in the Characterization Data

At the NEWGEN FORGE site, significant amount of data, either direct measurements (e.g., porosity, permeability, thermal conductivity) or proxy “soft” data (seismic velocity, resistivity, density) have been collected/inferred and integrated for characterizing the site to identify locations of hydrothermal reservoirs and characterize the geothermal resources. Initial EarthVision models have been developed for 3D visualization of the geophysical/geological data volume.

In order to quantify the uncertainty associated with the derived parameters and to guide the uncertainty reduction with further data acquisition and integration, the derived parameters can be defined in a probabilistic manner to enable the associated uncertainty to be quantified. The resulted probability distributions of hydrogeological, thermal, and mechanical parameters and model output variables (e.g., simulated temperature profiles) enable reliable risk assessment and decision-making, for example, by evaluating the exceedance probability of a temperature and its gradient over required thresholds and permeability below a threshold at a certain depth of the target reservoir away from the existing boreholes.

Quantifying the uncertainties of the parameters can be started with deriving probability distributions, multivariate cross-correlation, as well as geostatistical attributes (e.g., spatial variogram) given the spatial distributions of multivariate characterization data of intrinsic properties (e.g., porosity, permeability, thermal conductivity) of the solid matrix.

Figure A.43 shows the spatial variograms of well log porosity, dry density, and thermal conductivity at Wells GEO-N1, GEO-N2, GEO-N4, and GEO-N5. The data are from the depths of 1400 ft to 4150 ft. Figure A.44 and Figure A.45 show the cross-correlation and marginal/individual probability density functions of the three properties, respectively. These figures indicate certain levels of spatial variability and heterogeneity in the properties of interest and that their spatial patterns are slightly different. Representing the parameter uncertainties in the forms of joint probability distribution and geostatistical models enable robust conditional simulations of the property fields at un-sampled locations with unbiased estimates and quantified uncertainty.

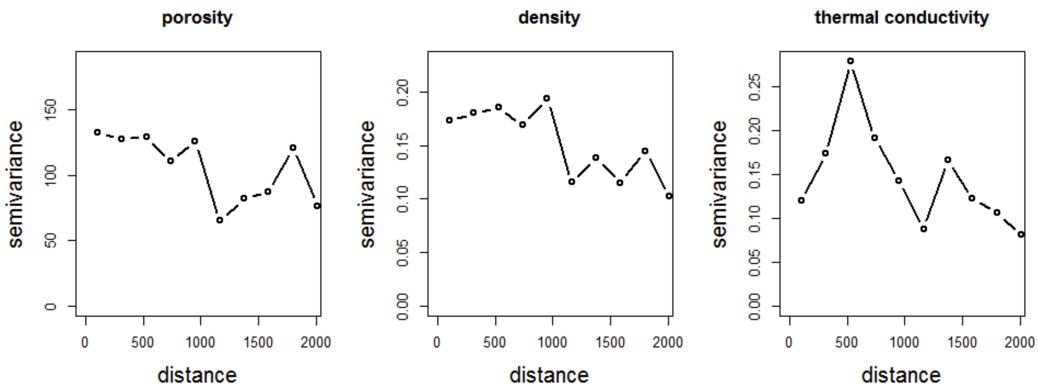

Figure A.43. Geostatistical analysis (spatial semivariance) of well log porosity, dry density, and thermal conductivity at Wells GEO-N1, GEO-N2, GEO-N4, and GEO-N5. The data are from the depths of 1400 ft to 4150 ft. The spatial correlation patterns of the three properties are slightly different.

The uncertainty associated with thermal conductivity are further illustrated by comparing its probability distribution at Well NWG 55-29 with the probability distribution across 15 Newberry wells (Figure A.46). It is clear that thermal conductivity is positively skewed with a larger mode and mean than the thermal conductivity across the wells in the region, but the uncertainty ranges are very close, around 1.5~2.3 W/(m.K).

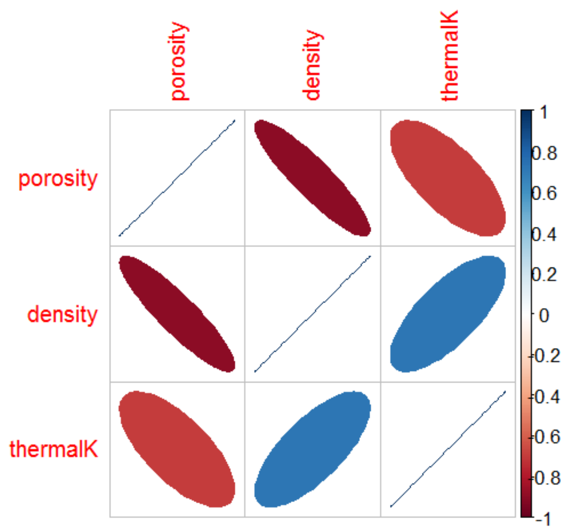

Figure A.44. Cross-dependence structure of collocated porosity, dry density, and thermal conductivity at Wells GEO-N1, GEO-N2, GEO-N4, and GEO-N5. The data are from the depths of 1400 ft to 4150 ft. Blue indicates positive correlations, red means negative correlations.

Figure A.47 shows the uncertainty in thermal gradient and permeability in terms of probability distributions with available measurement data. Thermal gradient seems to follow a normal distribution with a mean of 122.9ºC/km and standard deviation of 28.5ºC/km. A uniform distribution is assumed for permeability as a prior uncertainty measure, and the distribution can be updated as more data for permeability are collected with hydrogeological tests in the study area.

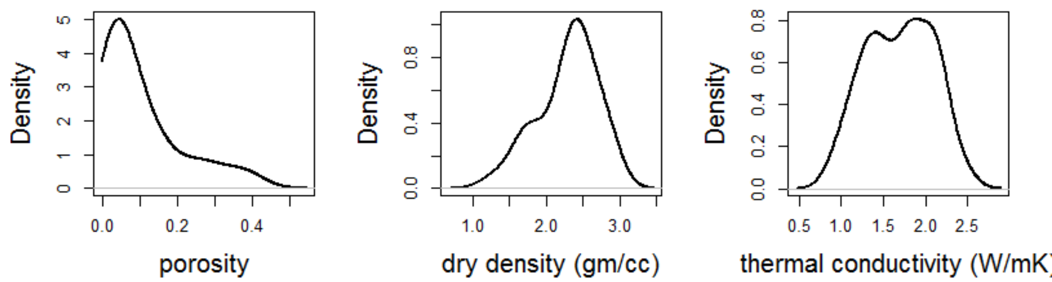

Figure A.45. Fitted probability density functions of well log porosity, dry density, and thermal conductivity at GEO Wells N1, N2, N4, and N5.

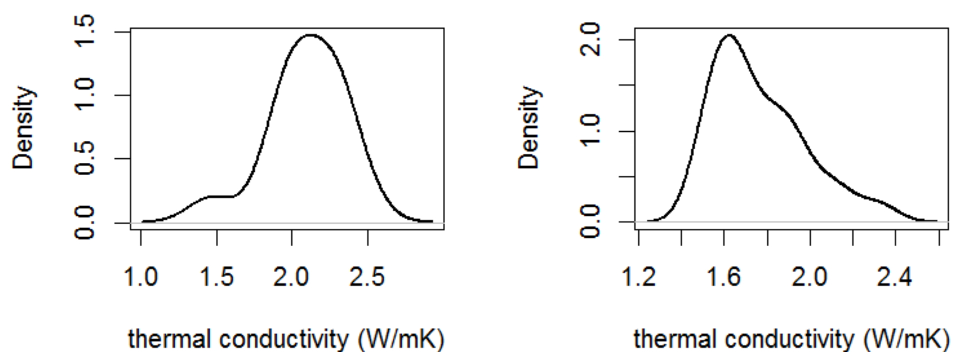

Figure A.46. Fitted probability density functions of thermal conductivity at Well NWG 55-29 (left) and across 15 Newberry wells (right).

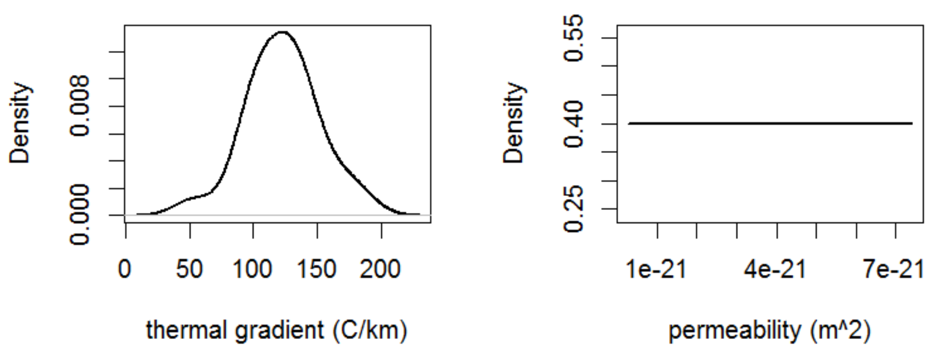

Figure A.47. Fitted probability density functions of thermal gradient and permeability across Newberry wells.

These analyses are initial steps of uncertainty quantification to provide uncertainty estimation and quantification capability in assimilating the large, diverse data for building and parameterizing the conceptual-mathematical models, in calibrating and integrating diverse hard and soft data to ensure efficient updating of auditable, fully traceable, and defensible models, and in developing and improving numerical models toward a better understanding of the NEWGEN FORGE geothermal system.

A.5.3 Future Approach for Uncertainty Quantification, Propagation, and Reduction

There are different sources of uncertainty in a typical geothermal exploration study which involves data acquisition and interpretation for characterization and monitoring, and analytical/numerical modeling for predictions and decision-making. Uncertainties are normally associated with quality of data and its spatiotemporal coverage and resolution, mode assumptions (structural uncertainty), and uncertain parameter values (parametric uncertainty).

At the NEWGEN FORGE site, significant amount of data, either direct measurements (e.g., porosity, permeability, thermal conductivity) or proxy “soft” data (seismic velocity, resistivity, density) have been collected/inferred and integrated for characterizing the site to identify locations of hydrothermal reservoirs and characterize the geothermal resources. Initial EarthVision models have been developed for 3D visualization of the geophysical/geological data volume. Information about fracture and fault and stress fields are also obtained. However, it is never possible to fully characterize a subsurface field given data limitation due to accessibility and affordability. A successful practice is usually to reduce the uncertainty to an adequately low level. Here the most relevant sources of uncertainty comes from 1) geophysical and geological data interpretation regarding the boundaries of the different geophysical/lithological units (although the geophysical surveys such as seismic, gravity, resistivity, and gamma ray logs in general are very consistent and are complementary to each other, there are locations with property discontinuity or without data coverage), 2) the spatially varying mineralogy, and 3) the spatial variability/heterogeneity in hydrogeological, thermal, and mechanical properties.

In order to quantify the uncertainty associated with the derived parameters and to guide the uncertainty reduction with further data acquisition and integration, the derived parameters will be defined in a probabilistic manner to enable the associated uncertainty to be quantified. The resulted probability distributions of physical and geometric parameters and model output variables (e.g., simulated temperature profiles) will enable reliable risk assessment and decision-making, for example, by evaluating the exceedance probability of a temperature and its gradient over required thresholds and permeability below a threshold at a certain depth of the target reservoir away from the existing boreholes.

We will adopt a suite of uncertainty quantification approaches that have been developed and applied for various subsurface characterization and modeling studies, with the purpose to make the best use of the available data sets, to evaluate data worth and redundancy and therefore to identify locations for further data acquisition, and to reduce uncertainty in the derived parameters and the numerical model predictions. Ultimately, it will provide robust geological models to fully address the uncertainties in the lithology and their interfaces/properties. Probability distribution functions will be derived for the structure boundary/geometry as well as for the major hydrogeological, thermal, and geophysical properties at un-sampled locations for more systematic evaluation of uncertainties and more reliable predictive modeling. The products for decision-making will be in a probabilistic manner (e.g., exceedance probabilities) instead of a set of deterministic values.

In some cases, e.g., seismic tomography 3D MT, 3D gravimetry, sensitivity analyses of model parameters (e.g., seismic *P-wave* and *S-wave* velocity, electrical resistivity, density) can be carried out numerically. OSU is currently undertaking a series of 3D MT sensitivity analyses by perturbing the 3D resistivity models that result from inversion of the full combined MT data set by embedding a series of highly conductive bodies of varying dimensions and depths within those models. The ability to resolve features at each position within the model volume depends on the locations of recording stations, the frequency bandwidth of the data recorded at each station, and the conductance of the earth volume overlying and adjoining each of the perturbing features. While this is computationally expensive, involving multiple cycles of forward and inverse modeling as well as a considerable amount of supercomputer time to explore fully, so completion of this task is not compatible with the scope of work and resource levels of FORGE Phase 1, by continuing this during Phase 2 it will be possible to determine the minimum size, conductance, and aspect ratio of any conductive feature, at any position within the model, that rises above the threshold of resolvability. This process is being used to guide the design of an array of additional MT stations that we plan to occupy during Phase 2 of FORGE, to increase the spatial resolving power of the

MT data set. Similar activities will support seismic and gravimetry planning. Coupled with an evaluation of the *Jacobian* (i.e., the matrix of partial derivatives that shows the sensitivity of the geophysical observations to changes in model parameters), the geophysically inferred parameter uncertainties can be quantified probabilistically. Having quantified the spatial resolution limits and model parameter sensitivities of the key geophysical data sets through this process, the next step is to transform this information into uncertainties on derived parameters such as porosity and permeability. This can be guided by adoption of parametric models that link geophysical observables to derived EGS parameters. Campanyà et al. (2015) calibrate the electrical resistivity obtained from MT data using laws relating electrical conductivity to porosity and permeability, to extrapolate the porosity-permeability values measured in boreholes. They derived a generalized version of Archie's law to determine the cementation exponent of different types of rocks from porosity and electrical conductivity data. Permeability values were calculated from porosity, electrical conductivity and cementation exponent data. The influences of the parametric variables were tested, showing which variables create more instability in the final results. This provides a good theoretical framework for mapping the uncertainties in geophysical parameters into the space of EGS parameters.

All the prior uncertainties associated with geological structure or physical parameters, are to be represented given hard and soft information (some inference models involved), and the parameter/factor space (usually multi-dimensional) are then explored using efficient sampling approaches to enable ensemble simulations of forward models (e.g., coupled THMC model, thermal conductive model, 3D velocity model), and further reduction of uncertainty in the parameters and model predictions can be achieved via data assimilation (e.g., Ensemble Kalman filter) and model calibration (e.g., Markov Chain Monte Carlo Bayesian) when relevant observational data (e.g., thermal profiles, deformation) are available.

The Uncertainty Quantification study, integrating the physical/geometric properties of the geologic formation, hydrogeological, thermal, and mechanical parameters, and their geostatistical attributes or spatial patterns, will include but not be limited to the following components:

- Prior/initial parametric uncertainty: probability distributions for all quantitative properties (continuous or categorical factors, e.g., porosity, permeability, thermal conductivity, lithological units) will be derived based on prior ranges or statistical attributes of the properties using entropy theory, or fitted directly from measurement values.
- Geostatistical modeling: Given the spatial distributions of multivariate characterization data of intrinsic properties (e.g., porosity, permeability, thermal conductivity) of the solid matrix, spatial correlation patterns and cross-dependence structure can be obtained. The resulted spatial variogram and cross-correlation models can be used for robust conditional simulations of the property fields at un-sampled locations with UNBIASED estimates and QUANTIFIED uncertainty. Multiple realizations of the fields can be visualized in EarthVision and serve as exploratory model inputs for thorough evaluation of thermal and THMC models. Geostatistical models of stratigraphic/geophysical interfaces can also be inferred based on well log information, which enables stochastic mapping of the interfaces at locations away from the boreholes.
- Efficient sampling techniques: efficient sampling, such as Quasi Monte Carlo, Latin Hypercube sampling, probabilistic collocation method, will be used to generate the most representative scenarios for risk (e.g., exceedance probability) analysis, for systematic evaluation of the relative significance (i.e., impacts on temperature/stress distributions and other end-products) of each factor/parameter in the numerical models, and for uncertainty propagation in an effective manner.
- Uncertainty propagation and response surface evaluation: The ensemble model simulations enable statistical analysis of the impacts of major parameters on model outputs (e.g., stress or temperature distributions). The parameter contributions can be screened such that only a subset of parameters are

identified to be critical and will be the focus for detailed characterization. Meanwhile, the developed relationships between the parameters and model outputs can be used as emulators for model calibration.

- Uncertainty reduction: Data assimilation (e.g., Ensemble Kalman filter) and model calibration (e.g., Markov Chain Monte Carlo Bayesian) will be used to reduce parametric and prediction uncertainty with constraints from observations. We will also evaluate data worth and redundancy with uncertainty maps to provide guidance on location, time, and types of additional data acquisition for most effective uncertainty reduction. Probabilistic joint distributions of the major parameters will be derived within each stratigraphic/geophysical units to help further reduce the parametric uncertainty. In addition, model selection approaches will be used to identify the most accurate geophysical data interpretation approach(s). Data quality can also be improved with robust outlier detection and gap filling in spatial and temporal data series.

These analyses are to provide uncertainty estimation and quantification capability in assimilating the large, diverse data for building and parameterizing the conceptual-mathematical models, in calibrating and integrating diverse hard and soft data to ensure efficient updating of auditable, fully traceable, and defensible models, and in developing and improving numerical models toward a better understanding of the NEWGEN FORGE geothermal system.

A.6 References

Achauer, U., J.R. Evans, and D.A. Stauber. 1988. "High-resolution seismic tomography of compressional wave velocity structure at Newberry Volcano, Oregon Cascade Range." *Journal of Geophysical Research* 93(10):135–10,148.

Ake, J., R. LaForge, and F. Hawkins. 2001. "Probabilistic seismic hazard analysis for Wickiup Dam - Deschutes project, central Oregon." U.S. Bureau of Reclamation Seismotectonic Report 2000-04, U.S. Bureau of Reclamation, pp 71.

AltaRock (AltaRock Energy, Inc.). 2011. Phase I Report. Newberry EGS Demonstration, DOE Award: DE-EE0002777. August 26.

AltaRock (AltaRock Energy, Inc.). 2014. Phase 2.1 Report. Newberry EGS Demonstration, DOE Award: DE-EE0002777. June 4.

AltaRock (AltaRock Energy, Inc.). 2015. Phase 2.2 Report. Newberry EGS Demonstration, DOE Award: DE-EE0002777. July 3.

Bargar, K.E. and T.E.C. Keith. 1999. "Hydrothermal Mineralogy of Core from Geothermal Drill Holes at Newberry Volcano, Oregon." USGS Professional Paper 1578, U.S. Geological Survey, pp 92.

Bauer, H.H. and J.J. Vaccarro. 1987. "Documentation of a deep percolation model for estimation ground-water recharge." USGS Open-File Report 86-536, U.S. Geological Survey, pp 180.

Beachly, M.W., E.E.E. Hooft, D.R. Toomey, and G.P. Waite. 2012. "Upper crustal structure of Newberry Volcano from P-wave tomography and finite difference waveform modeling." *Journal of Geophysical Research* 117(B10311):17.

Bisdorf, R.J. 1983. "Schlumberger soundings near Newberry caldera, Oregon." U.S. Geological Survey Open File Report 83-825:51.

Bisdorf, R.J. 1985. “Schlumberger sounding results over the Newberry Volcano area, Oregon.” Geothermal Resources Council Transactions 9, Part II, 389–394.

Blackwell, D. 1994. “A Summary of Deep Thermal Data from the Cascade Range and Analysis of the ‘Rain Curtain’ Effect.” Open File Report O-94-07, (Oregon) Department of Geology and Mineral Industries (DOGAMI).

Blackwell, D.D. and M.C. Richards. 2004. Geothermal Map of North America, American Association of Petroleum Geologists, Tulsa, Oklahoma, scale, 1:6,500,000.

Blackwell, D., M. Richards, Z. Frone, J. Batir, A. Ruzo, R. Dingwall, and M. Williams. 2011. “Temperature-At-Depth Maps for the Conterminous U.S. and Geothermal Resource Estimates.” *Geothermal Resources Council 2011*, Annual Meeting, San Diego, California.

Blackwell, D.D. and R.E. Spafford. 1987. “Experimental methods in continental heat flow.” *Geophysics - Field Measurements*. Series: Methods in Experimental Physics, ISBN: 9780124759671. Elsevier, vol. 24, pp. 189-226. DOI: 10.1016/S0076-695X(08)60599-2.

Bott, J.D.J. and I.G. Wong. 1993. “Historical earthquakes in and around Portland, Oregon.” *Oregon Geology* 55:116-122.

Braunmiller, J., J. Nabelek, B. Leitner, and A. Qamar. 1995. “The 1993 Klamath Falls, Oregon earthquake sequence: Source mechanisms from regional data.” *Geophysical Research Letters* 22(2):105–108.

Campanyà, J., A.G. Jones, J. Vozár, V. Rath, S. Blake, R. Delhaye, and T. Farrell. 2015. “Porosity and Permeability Constraints from Electrical Resistivity Models: Examples Using Magnetotelluric Data.” In *Proceedings World Geothermal Congress 2015* April 19-25, Melbourne, Australia.

Cladouhos, T., S. Petty, O. Callahan, W. Osborn, S. Hickman, and N. Davatzes. 2011a. “The Role of Stress Modeling in Stimulation Planning at the Newberry Volcano EGS Demonstration Project.” In *Proceedings: Thirty-Sixth Workshop on Geothermal Reservoir Engineering*, Stanford University, Stanford, California, January 31–February 2, SGP-TR-191.

Cladouhos, T., M. Clyne, M. Nichols, S. Petty, W. Osborn, and L. Nofziger. 2011b. “Newberry Volcano EGS Demonstration Stimulation Modeling.” *GRC Transactions*, pre-print by request.

Cladouhos, T.T., W.L. Osborn, and S. Petty. 2012. “Newberry Volcano EGS Demonstration – Phase I Results.” In *Proceedings of the Thirty-Seven Workshop on Geothermal Reservoir Engineering*, Stanford University, Stanford, California, January 30-February 1, SGP-TR-194.

Cladouhos, T.T., S. Petty, Y. Nordin, M. Moore, K. Grasso, M. Uddenberg, M. Swyer, B. Julian, and G. Foulger. 2013a. “Microseismic Monitoring of Newberry Volcano EGS Demonstration.” In *Proceedings of the Thirty-Seventh Workshop on Geothermal Reservoir Engineering*, Stanford University, Stanford, California, February 11–13.

Cladouhos, T.T., S. Petty, Y. Nordin, M. Moore, K. Grasso, M. Uddenberg, and M. Swyer. 2013b. “Improving Geothermal Project Economics with Multi-zone Stimulation: Results from the Newberry Volcano EGS Demonstration.” In the *47th U.S. Rock Mechanics/Geomechanics Symposium*, San Francisco, California, June 23–26.

Cladouhos, T.T., M.W. Swyer, M. Uddenberg, and S. Petty. 2015a. “Results from Newberry Volcano EGS Demonstration.” In *Proceedings of the Fortieth Workshop on Geothermal Reservoir Engineering*, Stanford University, Stanford, California.

Cladouhos, T.T., S. Petty, M. Swyer, M. Uddenberg, K. Grasso, and. Y. Nordin. 2015b. “Results from Newberry Volcano EGS Demonstration, 2010–2014.” *Geothermics* http://dx.doi.org/10.1016/j.geothermics.2015.08.009.

Cole, D.L. 2006. “Groundwater Quality Report for the Deschutes Basin, Oregon.” DEQ Laboratory and Water Quality Divisions, Portland, Oregon, pp 59.

Cornet, F.H., T. Bérard, and S. Bourouis. 2007. “How close to failure is a granite rock mass at a 5 km depth?” *International Journal of Rock Mechanics and Mining Sciences* 44:47–66.

Crider, J.G. 2001. “Oblique slip and the geometry of normal-fault linkage: mechanics and case study from the Basin and Range in Oregon.” *Journal of Structural Geology* 23:1997–2009.

Dames and Moore. 1994. “Revised Report, Newberry Geothermal Project Hydrology Baseline Study Newberry Volcano, Oregon.” For CE Exploration Company, Portland, Oregon, pp 268.

Davatzes N.C. and S.H. Hickman. 2011. Preliminary Analysis of Stress in the Newberry EGS Well NWG 55-29. *GRC Transactions* 35:323–332.

Draus, E. 2002. Magnetic Stratigraphy of the Middle Miocene (Early Barstovian) Mascall Formation, Central Oregon. GSA Abstracts with Programs, Annual Meeting, Denver, Colorado.

Donath, F.A. 1962. Analysis of basin-range structure, south-central Oregon. *Geological Society of America Bulletin* 73:1–16.

Donnelly-Nolan, J.M, D.E. Champion, M.A. Lanphere, and D.W. Ramsey. 2004. New thoughts about Newberry Volcano, Central Oregon USA. *Eos, Transactions of the American Geophysical Union* 85(47) Fall Meeting Supplement, Abstract V43E-1452.

Donnelly-Nolan, J.M., and R.A. Jensen. 2009. Ice and water on Newberry Volcano, central Oregon. *Geological Society of America Field Guide 15*, pp. 1–10.

Donnelly-Nolan, J.M., W.K. Stovall, D.W., Ramsey, J.W. Ewert, and R.A. Jensen. 2011. Newberry Volcano – Central Oregon’s Sleeping Giant. Downloaded from http://pubs.usgs.gov/fs/2011/3145/ on March 16, 2016.

EIA (U.S. Energy Information Administration). 2014. Annual Energy Outlook 2014 with projections to 2040. Washington, D.C.

Epoch (2008a). NWG 55-29 mud log. Internal report to Davenport Power, LLC, 07/18/2008.

Epoch (2008b). NWG 46-16 mud log. Internal report to Davenport Power, LLC, 12/05/2008.

Fang, Y., S.A.M. den Hartog, D. Elsworth, C. Marone, and T. Cladouhos. 2015. “Anomalous distribution of microearthquakes in the Newberry Geothermal Reservoir: Mechanisms and implications.” doi:10.1016/j.geothermics.2015.04.005

Ferns, M.L., and J.D. McClaughry. 2006. Preliminary geologic map of the Powell Buttes 7 ½' quadrangle, Crook County, Oregon. Open-File Report O-06-24, Oregon Department of Geology and Mineral Industries, Portland, Oregon.

Fetterman, J.A. 2011. Porosity Evolution in Newberry Volcano Geothermal System: Feedback between Deformation and Alteration. M.S. thesis, RES, The School for Renewable Energy Science in affiliation with the Universities of Iceland and Akureyri, pp 74.

Fetterman, J.A., and N.C. Davatzes. 2011. Fracture Generated Porosity Evolution in the Newberry Volcano Geothermal System, OR: Feedback between Deformation and Alteration. *GRC Transactions*, pre-print by request.

Fitterman, D.V. 1988. Overview of the structure and geothermal potential of Newberry Volcano, Oregon. *Journal of Geophysical Research* 93(B9):10059–10066.

Fitterman, D.V., and D.K. Neev. 1985. Transient Sounding Investigation of Newberry Volcano, Oregon. *GRC Transactions* 9, Part II, pp. 407–410.

Fitterman, D.V., W.D. Stanley, and R.J. Bisdorf. 1988. Electrical structure of Newberry Volcano, Oregon. *Journal of Geophysical Research* 93(B9):10119–10134.

Frone, Z. 2015. Heat flow, termal modeling and whole rock geochemistry of Newberry Volcano, Oregon and heat flow modeling of the Appalachian Basin, West Virginia. Dissertation thesis, Southern Methodist University.

Frone, Z., A. Waibel, and D. Blackwell. 2014. "Thermal modeling and EGS potential of Newberry Volcano, Central Oregon." In *Proceedings, Thirty-Ninth Workshop on Geothermal Reservoir Engineering* Stanford University, Stanford, California, February 24–26, 2014,SGP-TR-202.

Gannett, M.W., K.E. Lite, D.S. Morgan, and C.A. Collins. 2001. Ground-water hydrology of the upper Deschutes Basin, Oregon. USGS Water-Resources Investigations Report 00–4162, U.S. Geological Survey, pp 78.

Gettings, M.E. and A. Griscom. 1988. Gravity Model Studies of Newberry Volcano, Oregon. *Journal of Geophysical Research* 93(B9):10109–10118, doi:10.1029/JB093iB09p10109.

Grasso, K., T. Cladouhos, and G. Garrison. 2013. Groundwater Monitoring and EGS: The Newberry EGS Demonstration. American Geophysical Union Annual Meeting, December 2013.

Grasso K., T. Cladouhos, S. Petty, G. Garrision, M. Uddenberg, M. Swyer, and Y. Nordin. 2014. Deep Stimulation at Newberry Volcano EGS Demonstration. Paper H43A-0940, American Geophysical Union Annual Meeting, December 2014.

Grasso, K., A. Meigs, and T. Cladouhos. 2012. Origin of faults, fissures, and volcanic vent alignments at a structural triple junction, Newbery Volcano, Central Oregon. American Geophysical Union Cordilleran Section Meeting, Queretaro, Mexico.

Heffer, K. 2002. "Geomechanical influences in water injection projects: An overview." *Oil & Gas Science and Technology* 57:415-422.

Hickman, S.H., M.B. Zoback, C.A. Barton, R. Benoit, J. Svitek, J., and R. Summers. 2000. Stress and permeability heterogeneity within the Dixie Valley Geothermal reservoir: recent results from well 82-5, Proceedings: 25th Workshop on Geothermal Reservoir Engineering, Stanford University, Stanford, California, January 24-26, 2000 SGP-TR-165.

Humphreys, E.D., and D.D. Coblentz. 2007. North American dynamics and western US tectonics. *Reviews of Geophysics* 45(3).

Jensen, R.A., J.M. Donnelly-Nolan, and D. McKay. 2009. A field guide to Newberry Volcano, Oregon, *in* O'Connor, J., R.J. Dorsey, and I.P. Madin, (eds.), Volcanoes to vineyards: geologic field trips through the dynamic landscape of the Pacific Northwest, Volume 15. Boulder, Geological Society of America, pp. 53–79.

Jensen, R.A. 2006. Roadside guide to the geology of Newberry Volcano (4th edition). CenOreGeoPub, Bend, Oregon, pp 182.

Jordan, B.T., A. Grunder, R.A. Duncan, and A.L. Deino. 2004. Geochronology of age-progressive volcanism of the Oregon High Lava Plains: Implications for the plume interpretation of Yellowstone. *Journal of Geophysical Research* Vol. 109. doi: :10.1029/2003JB002776.

Kelbert, A., N.M. Meqbel, G.D. Egbert, and K. Tandon. 2014. ModEM: A modular system for inversion of electromagnetic geophysical data. *Computers & Geosciences* 66:40–53.

Kim, J., E. Sonnenthal, and J. Rutqvist. 2012. Formulation and Sequential Numerical Algorithms of Coupled Fluid/Heat Flow and Geomechanics for Multiple Porosity Materials. *International Journal of Numerical Methods in Engineering*, doi: 10.1002/nme.4340.

Kim J., E. Sonnenthal, and J. Rutqvist. 2015. A sequential implicit algorithm of chemo-thermo-poro-mechanics for fractured geothermal reservoirs. *Computers & Geosciences* 76:59–71.

Lawrence, R.D. 1976. Strike-slip faulting terminates the Basin and Range province in Oregon. Geological Society of America Bulletin 87:846–850.

Letvin, A.I. 2011. Analysis of drill cuttings mineralogy and geophysical logs to investigate alteration history at Newberry NWG 55-29 in preparation for EGS stimulation. Confidential M.S. thesis. The School for Renewable Energy Science in affiliation with the Universities of Iceland and Akureyri, pp 68 with appendices.

MacLeod, Norman S. and David R. Sherrod, 1988, Geologic evidence for a magma chamber beneath Newberry Volcano, Oregon. J*ournal of Geophysical Research* Vol. 93, No. B9, pp 10067-10079.

MacLeod, N.S., D.R. Sherrod, L.A. Chitwood, and E.H. McKee. 1981. Newberry Volcano, Oregon, in Guides to Some Volcanic Terranes in Washington, Idaho, Oregon, and Northern California, D.A. Johnston and J. Donnelly-Nolan (eds.), USGS Circular 838, 85–104, U.S. Geological Survey.

MacLeod, N.S., D.R. Sherrod, and L.A. Chitwood. 1982. Geologic map of Newberry Volcano, Deschutes, Klamath, and Lake Counties, Oregon. USGS Open-File Report 82-847, U.S. Geological Survey.

MacLeod, N.S., D.R. Sherrod, L.A. Chitwood, and R.A. Jensen. 1995. Geologic Map of Newberry Volcano, Deschutes, Klamath, and Lake Counties, Oregon. U.S. Geological Survey, 2 sheets, scale 1:62,500, pamphlet, 523 p, scale 1:62,500.

Mark-Moser, M., J. Schultz, A. Schultz, B. Heath, K. Rose, S. Urquhart, E. Bowles-Martinez, and P. Vincent. 2016. A conceptual geologic model for the Newberry Volcano EGS Site in Central Oregon: Constraining heat capacity and permeability through interpretation of multicomponent geosystems data. Proceedings: 41st Workshop on Geothermal Reservoir Engineering Stanford University, Stanford, California, February 22–24, 2016 SGP-TR-209.

Matzel, E., D. Templeton, A. Peterson, and M. Goebel. 2014. Imaging the Newberry EGS Site using Seismic Interferometry. Proceedings: Thirty-Ninth Workshop on Geothermal Reservoir Engineering Stanford University, Stanford, California, February 24–26, 2014.

McCaffery, R., A.I. Qamar, R.W., King, R. Wells, G. Khazaradze, C. Williams, C.W. Stevens, J.J. Vollick, and P.C. Zwick. 2007. Fault locking, block rotation and crustal deformation in the Pacific Northwest. *Geophysical Journal International* 169:1315–1340.

McCaffrey, R., R.W. King, S.J. Payne, and M. Lancaster. 2013. Active tectonics of northwestern US inferred from GPS-derived surface velocities. *Journal of Geophysical Research: Solid Earth* 118(2):709–723.

McClaughry, J.D., and M.L. Ferns. 2006, Field trip guide to the geology of the Lower Crooked River Basin, Redmond and Prineville Areas, Oregon. *Oregon Geology* 67(1):15–23.

McKay, D., J.M. Donnelly-Nolan, R.A. Jensen, and D.E.Champion. 2009. The post-Mazama northwest rift zone eruption at Newberry Volcano, Oregon. *Geological Society of American Field Guide 15*, pp. 91-110, doi 10.1130/2009.fl d015(05).

Meigs, A., K. Scarberry, R.Carlson, M.T. Ford, M. Fouch, T. Grove, W.K. Hart, M. Iademarco, B. Jordan, J. Milliard, M.J. Streck, D. Trench, and R. Weldon. 2009. Geological and geophysical perspectives on the magmatic and tectonic development, High Lava Plains and northwest Basin and Range. *Geological Society of America Field Guide 15*, pp. 435-470, doi 10.1130/2009.fl d015(21).

Meqbel, N.M., G.D. Egbert, P.E. Wannamaker, A. Kelbert, and A. Schultz. 2014. Deep electrical resistivity structure of the northwestern U.S. derived from 3-D inversion of USArray magnetotelluric data. *Earth and Planetary Science Letters*. Available online, ISSN 0012-821X, http://dx.doi.org/10.1016/j.epsl.2013.12.026.

Morgan, D.S., S.R. Hinkle, and R.J. Weick. 2007. Evaluation of approaches for managing nitrate loading from on-site wastewater systems near La Pine, Oregon. USGS Scientific Investigations Report 2007–5237, U.S. Geological Survey, 76 pp.

Morgan, D.S., D.Q. Tanner, and M.D. Crumrine. 1997. Hydrologic, water-quality, and meteorologic data for Newberry Volcano and vicinity, Deschutes county, Oregon, 1991-1995. USGS Open-File Report 97-4088, U.S. Geological Survey, 72 p.

Norbeck, J.H., McClure, M.W., Horne, R.N. 2016. Revisiting stimulation mechanisms at Fenton Hill abd an investigation of the influence of fault heterogeneity on the Gutenberg-Richter b-value for rate-and-state earthquake stimulations. Proceedings: 41st Workshop on Geothermal Reservoir Engineering Stanford University, Stanford, California, February 22–24, 2016 SGP-TR-209.

Neumann, F. 1938. United States earthquakes 1936–1940. U.S. Coast and Geodetic Survey Serial No. 6510, pp. 45.

Olhoeft, G.R. 1981. Electrical properties of granite with implications for the lower crust. *Journal of Geophysical Research* 86(B2):931–936.

Osborn, W.L., S. Petty, T.T. Cladouhos, J. Iovenitti, L.Nofziger, O. Callahan, D.S. Perry, and P.L. Stern. 2011. Newberry Volcano EGS Demonstration, Phase I results. *GRC Transactions* 35:499–505.

Parkhomenko, E I. 1967. Electrical Properties of Rocks. Plenum, New York.

Personius, S.F. (compiler). 2002a. Fault number 838, La Pine graben faults. In Quaternary fault and fold database of the United States, USGS Website. http://earthquakes.usgs.gov/regional/qfaults, last accessed 01/13/2011.

Personius, S.F. (compiler). 2002b. Fault number 1806, Newberry volcano ring faults. In Quaternary fault and old database of the United States, USGS Website. http://earthquakes.usgs.gov/regional/qfaults, last accessed 01/14/2011.

Pezzopane, S.K., and R.J.I. Weldon. 1993. Tectonic role of active faulting in central Oregon. *Tectonics* 12(5):1140–1169.

PNSN (Pacific Northwest Seismic Network). 2015. Volcano Seismicity – Newberry. Pacific Northwest Seismic Network (PNSN). Available at: http://www.pnsn.org/volcanoes/newberry

Priest, G.R. 1990. Volcanic and Tectonic Evolution of the Cascade Volcanic Arc, Central Oregon. *Journal of Geophysical Research* 95(B12):19.583–19.599.

Roberts, C.W., R.P. Kucks, and P.L. Hill. 2008. Oregon magnetic and gravity maps and data–A website for distribution of data. U.S. Geological Survey Data Series 355.

Robinson, P.T., G.F. Brem, and E.H. McKee. 1984. John Day Formation of Oregon: A Distal Record of Early Cascade Volcanism. *Geology* 12(4):229–232.

Sammel, E.A., S.E. Ingebritsen, and R.H. Mariner. 1988. The hydrothermal system at Newberry Volcano, Oregon. *Journal of Geophysical Research* 93(B9):10149–10162.

Sammel, E.A. and R.W. Craig. 1983. Hydrology of the Newberry Volcano Caldera, Oregon. USGS Water Resources Investigation Report 83-4091, U.S. Geological Survey.

Scarberry, K.C., A.J. Meigs, and A.L. Grunder. 2010. Faulting in a Propagating Continental Rift: Insight from the late Miocene Structural Development of the Abert Rim Fault, Southern Oregon, USA. *Tectonophysics* 488:71–86, doi: 10.1016/j.tecto.2009.09.025.

Schmidt M.E., A.L. Grunder, and M.C. Rowe. 2008. Segmentation of the Cascade Arc as indicated by Sr and Nd isotopic variation among diverse primitive basalts. *Earth and Planetary Science Letters* 266(1 2):166–181.

Schultz, A. 2013a. Magnetic observatories and transportable magnetotelluric observatory arrays: imaging the Earth's interior on planetary, continental and local scales. Seminars presented to University of Tokyo

Earthquake Research Institute, and to the Kakioka Magnetic Observatory 100th Anniversary Commemoration Event, Tokyo and Kakioka, Japan, January 2013.

Schultz, A. 2013b. Reservoir characterization – geophysics. Briefing to the JASON Group, La Jolla, California, Thursday, June 20, 2013.

Schultz, A., P. Vincent, K. Rose, A. Hakala, C. Lopano, K. Schroeder, S. Urquhart, J. Hare, and L. Beard. 2012. 4D monitoring techniques to improve reservoir longevity and productivity in Enhanced Geothermal Systems. Intrnational Workshop on Deep Geothermal Systems, Wuhan, China, June 29–30, 2012.

Schultz, A., P. Vincent, K. Rose, A. Hakala, C. Lopano, K. Schroeder, S. Urquhart, J. Hare, and L. Beard. 2013. Integrating geophysical and geochemical methods for 4D monitoring of fluid infiltration, permeability and mineralization reactions in Enhanced Geothermal Systems. International Workshop on the Exploration and Development of Geothermal Resources in Guangdong and Hong Kong, Guangzhou, China, June 29–30, 2013.

Schultz, A., P. Vincent, S. Urquhart, L. Beard, J. Hare, and K. Rose. 2014. Novel use of 4D monitoring techniques at Newberry Volcano Enhanced Geothermal System Demonstrator Site designed to improve reservoir longevity and productivity. 22nd International Workshop on Electromagnetic Induction in the Earth, Weimar, Germany August 24–30, 2014.

Sherrod, D.R., and W.E. Scott. 1995. Preliminary geologic map of the Mount Hood 30- by 60-minute quadrangle, northern Cascade Range, Oregon. U.S. Geological Survey Open-File Report 95-219.

Sherrod, D.R., and J.G. Smith. 2000. Geologic map of upper Eocene to Holocene volcanic and related rocks of the Cascade Range, Oregon. United States Geological Survey.

Sherrod, D.R., M.W. Gannett, and K.E. Lite. 2002. Hydrogeology of the Upper Deschutes Basin, Central Oregon: A Young Basin Adjacent to the Cascade Volcanic Arc. Field Guide to Geologic Processes in Cascadia, Oregon Department of Geology and Mineral Industries Special Paper 36.

Sherrod, D.R., E.M. Taylor, M.L. Ferns, W.E. Scott, R.M. Conrey, and G.A. Smith. 2004. Geologic map of the Bend 30×60-minute quadrangle, central Oregon. USGS Geologic Investigations Series 1-2683.

Smith, G.A. 1986. Stratigraphy, sedimentology, and petrology of Neogene rocks in the Deschutes basin, central Oregon: a record of continental-margin volcanism and its influence on fluvial sedimentation in an arc-adjacent basin. PhD dissertation, Oregon State University, Corvallis, Oregon, 467 pp.

Sonnenthal, E.L., N. Spycher, O. Callahan, T. Cladouhos, and S. Petty. 2012. A thermal-hydrological-chemical model for the enhanced geothermal system demonstration project at Newberry Volcano, Oregon. Proceedings: Thirty-Seventh Workshop on Geothermal Reservoir Engineering, Stanford University, Stanford, California, January 30–February 1, SGP-TR-194.

Sonnenthal, E.L., N. Spycher, O. Callahan, T. Cladouhos, and S. Petty. 2012. A thermal-hydrological-chemical model for the enhanced geothermal system demonstration project at Newberry Volcano, Oregon. Proceedings: Thirty-Seventh Workshop on Geothermal Reservoir Engineering, Stanford University, Stanford, California, January 30–February 1, SGP-TR-194.

Spielman, P. and J. Finger. 1998. Well Test Results of Exploration Drilling at Newberry Crater, Oregon in 1995. Proceedings: Twenty-Third Workshop on Geothermal Reservoir Engineering, Stanford University, Stanford, California, January 26–28, 1998, SGP-TR-158.

Stanley, W.D. 1982. A regional magnetotellurlc survey of the Cascades Mountains region. USGS Open-File Report 82-126. U.S. Geological Survey, Denver, Colorado, 20 pp.

Taylor, E.M. 1990. Volcanic history and tectonic development of the Central High Cascade Range, Oregon. *Journal of Geophysical Research: Solid Earth* 95(B12), doi 10.1029/JB095iB12p19611.

Trench, D., A. Meigs, and A. Grunder. 2012. Termination of northwestern Basin and Range province into a clockwise rotation region of transtension and volcanism, southeast Oregon. *Journal of Structural Geology* 39:52–65.

Vosteen H.D., and R. Schellschmidt. 2003. Influence of Temperature on Thermal Conductivity, Thermal Capacity and Thermal Diffusivity for Different Types of Rock. *Physics and Chemistry of the Earth* 28:499–509.

Waibel, A.F., Z.S. Frone, and D.D. Blackwell. 2015. Geothermal exploration of Newberry Volcano, Oregon, Final Report for the DOE Innovative Exploration Technology (IET) Grant 109 program supporting geothermal exploration of Newberry Volcano, Oregon. Final report for DOE Award: DE-EE0002833. http://gdr.openei.org/files/485/NewberryDavenportAltaRockFinalReportAllAppendices.pdf

Wang, J., W. Jung, Y. Li, and A. Ghassemi. 2016, Geomechanical characterization of Newberry Tuff. *Geothermics*, doi:10.1016/j.geothermics.2016.01.016.

Wells, R.E., D. Burky, R. Friedman, D. Pyle, R. Duncan, P. Haeussler, and J. Wooden. 2014. Siletzia, a large igneous prvince in the Oregon and Washington Coast Range: Correlation with the Geomagnetic Polarity Timescale and Implications for a long-lived Yellowstone Hot Spot. *Geosphere* 10(4):1–28.

Wells, R.E., and R. McCaffrey. 2013. Steady rotation of the Cascade Arc. *Geology,* Geological Society of America 41(9):1027–1030, doi 10.1130/G34514.1.

Wells, R.E., C.S. Weaver, and R.J. Blakely. 1998. Fore arc migration in Cascadia and its neotectonic ignificance. *Geology* 26:759–762.

Werner, K.S., E.P. Graven, T.A. Berkman, and M.J. Parker. 1991, Direction of maximum horizontal compression in western Oregon determined by borehole breakouts. *Tectonics* 10:948–958.

Wernicke, B., and J. Snow. 1992. Cenozoic Tectonism in the Central Basin and Range: Motion of the Sierran-Great Valley Block. *International Geology Review* 40(5).

Williams, H. 1935. Newberry volcano of central Oregon. *Geological Society of America Bulletin* 46(2):253–304.

Wilson, D.S. 1993. Confidence intervals for motion and deformation of the Juan de Fuca plate. *Journal of Geophysical Research* 98:16053–16071.

Wong, I.G., and J.D.J. Bott. 1995. A look back at Oregon's earthquake history, 1841–1994. *Oregon Geology* 57:125–139.

Wong, I., W. Silva, J. Bott, D.Wright, P. Thomas, N. Gregor, S. Li, M. Mabey, A. Sojourner, and Y. Wang. 2000. Earthquake scenario and probabilistic ground shaking maps for the Portland, Oregon, metropolitan area, Oregon Department of Geology and Mineral Industries Interpretive Map Series IMS-16, scale 1:62,500, 11 sheets with 16 p. text.

Zonge (Zonge Geosciences, Inc.). 2007. Gravity survey on the Newberry project, Deschutes County, Oregon, for Davenport Resources LLC, Data Acquisition Report, 38 pp.

Zonge (Zonge Geosciences, Inc.). 2010. Gravity survey on the Newberry project, Deschutes County, Oregon, for Davenport Resources LLC, Data Acquisition Report, 41 pp.

Zonge (Zonge Geosciences, Inc.). 2012. Gravity survey on the Newberry project, Deschutes County, Oregon, for Davenport Resources LLC, Data Acquisition Report, 40 pp.